Novel Designs and Applications of Photonic Crystal Fibers

D i s s e r t a t i o n

zur Erlangung des akademischen Grades

d o c t o r r e r u m n a t u r a l i u m
(Dr. rer. nat.)
im Fach Physik

eingereicht an der
Mathematisch-Naturwissenschaftlichen Fakultät I
Humboldt-Universität zu Berlin

von
Dipl.-Phys. Jens Lutz Bethge

Präsident der Humboldt-Universität zu Berlin:
Prof. Dr. Jan-Hendrik Olbertz

Dekan der Mathematisch-Naturwissenschaftlichen Fakultät I:
Prof. Dr. Andreas Herrmann

Gutachter/innen:

1. Prof. Dr. Thomas Elsässer
2. Prof. Dr. Fedor Mitschke
3. Prof. Dr. Oliver Benson

eingereicht am: 28. Juli 2011
Tag der mündlichen Prüfung: 4. November 2011

Renate Bethge
14.3.1953 - 20.7.2006

Abstract

Photonic crystal fibers based on microstructured air-glass designs have significantly increased the capabilities of fiber optics. On the one hand, such fibers allow for extremely tight confinement of light in a small modal volume, giving rise to strongly enhanced nonlinear interaction between light and dielectric media. On the other hand, photonic crystal fibers also enable guiding of light in air cores rather than in glass. The latter type of fiber therefore reduces optical nonlinearities to an extent impossible in traditional fiber designs. This thesis explores new physical possibilities at both frontiers of photonic crystal fiber design, going significantly beyond existing technology in terms of dispersion management and in terms of enhancing or suppressing optical nonlinearities.

First, the concept of a novel chirped photonic crystal fiber is introduced. The qualitative dispersion and loss properties of this new fiber are theoretically derived from a model based on a chirped Bragg fiber. All essential design parameters are identified in this simple model. Furthermore, a finite element method is employed to calculate quantitative properties of the fiber and to optimize the design. The calculated results agree excellently with experimental data obtained from fabricated fiber samples. The superior guiding properties of this new photonic fiber are demonstrated in two experiments. The delivery of 25 fs pulses over a 1 meter distance is realized without any dispersion compensation. Moreover, using dispersion compensation, the delivery of even sub-20-fs pulses becomes possible. This demonstration sets a new record for the fiber-based delivery of ultrashort pulses.

Subsequently, a photonic crystal fiber with a liquid core is investigated. The fabrication of such a fiber is challenging. This work presents effective methods for the preparation and explains a scheme for successfully reducing the insertion loss. The fiber is optimized to support the highly efficient soliton-fission mechanism at unprecedented pulse energies in white-light supercontinuum generation. Because of the liquid core, the supercontinuum generation scheme can be scaled beyond the peak-power limitations of solid-core fibers. The generation of a two-octave spanning supercontinuum with 390 nJ pulse energy is demonstrated. The experimental results are compared to a numerical simulation and the underlying mechanism is identified.

Finally, an experiment is presented that exploits strong nonlinear interaction of two pulses inside a photonic crystal fiber for all-optical switching. This experiment requires extremely careful management of dispersion and nonlinearity. A novel effect is observed during the co-propagation of two ultrashort pulses with different wavelengths. Because of the dispersion properties in the chosen fiber, these pulses are propagating at nearly identical group velocities, which dramatically increases the nonlinear interaction via cross-phase modulation between the two pulses. Based on this interaction, a fully functional optical transistor is experimentally demonstrated with good switching contrast. In particular, the demonstrated optical transistor enables switching of a strong pulse by a much weaker pulse.

Zusammenfassung

Die Möglichkeiten der Faseroptik wurden durch die Entwicklung von photonischen Kristallfasern erheblich erweitert. Einerseits führen diese Fasern Licht in einem sehr kleinen Volumen, und ermöglichen hohe Spitzenleistungen sowie eine stark nichtlineare Wechselwirkung zwischen Licht und Dielektrikum im Faserkern. Andererseits ist aber auch die Lichtführung in einem luftgefüllten Kern möglich. In letzterem Fall ist die Nichtlinearität auf ein Maß reduziert, das mit herkömmlichen Fasern nicht möglich ist. Diese Dissertation untersucht neue physikalische Möglichkeiten an beiden Grenzen des Designs von photonischen Kristallfasern. Zum einen wird eine Kontrolle der Dispersion gezeigt, die weit über vorher existierende Technologie hinausgeht; zum anderen wird die optische Nichtlinearität in bisher nicht demonstriertem Maße angehoben oder unterdrückt.

Zuerst wird die Idee einer gechirpten photonischen Kristallfaser vorgestellt. Aus einem stark vereinfachten Modell, basierend auf einer gechirpten Braggfaser, werden die qualitativen Eigenschaften dieses neuen Fasertyps abgeleitet. Hier gelingt es, alle wichtigen Designparameter zu bestimmen. Im Weiteren wird eine finite-Elemente-Methode benutzt, um auch quantitative Eigenschaften dieser Fasern berechnen zu können, und die Struktureigenschaften zu optimieren. Die hervorragenden Leitungseigenschaften dieser Fasern werden dann in Experimenten demonstriert. Ohne jegliche Dispersionskompensation wird die Übertragung eines 25 fs Impulses in einer 1 Meter langen Faser gezeigt. Wird zusätzlich eine Dispersionskompensation verwendet, lassen sich sogar Impulse mit weniger als 20 fs Dauer übertragen.

Im Anschluss daran wird eine photonische Kristallfaser untersucht, die mit einer Flüssigkeit gefüllt ist. Allein die Herstellung einer solchen Faser ist eine Herausforderung. Diese Dissertation beschreibt eine Methode zum Befüllen einer Kristallfaser und zur Reduzierung der Kopplungsverluste. Die hergestellte Faser ist dahingehend optimiert, einen hoch effizienten Soliton-Fission Mechanismus zu ermöglichen, der zur Erzeugung von Weißlicht genutzt wird. Diese Weißlicht-Impulse haben eine mit Soliton-Fission bisher noch nie erreichte Energie von 390 nJ. Auf Grundlage einer guten Übereinstimmung mit den experimentellen Resultaten lässt sich aus numerischen Simulationen der zugrunde liegende Effekt bestimmen.

Abschließend wird über ein Experiment berichtet, das die nichtlineare Wechselwirkung zwischen zwei Impulsen verschiedener Wellenlänge ausnutzt, um einen optischen Schalter zu verwirklichen. Dieses Experiment erfordert genaueste Kontrolle der Dispersion und der Nichtlinearität in der Faser. Bei der gleichzeitigen Propagation von zwei Impulsen wird ein neuartiger Schalteffekt beobachtet. Beide Impulse haben nahezu die gleiche Gruppengeschwindigkeit, und ihre nichtlineare Wechselwirkung basierend auf Kreuz-Phasen-Modulation wird dadurch deutlich verstärkt. Hiermit wird ein voll funktionsfähiger optischer Transistor mit gutem Schaltkontrast experimentell demonstriert, der insbesondere einen schwachen Impuls einen stärkeren Impuls schalten lässt.

Contents

1 Introduction

Optical fibers constitute the back bone for all international voice and data traffic as well as for the internet. The very idea of transmitting information by modulating signals on a light beam and of detecting its information in a receiver dates back at least 130 years to Alexander Graham Bell's famous Photophone [1]. The other important building block is the optical fiber for light delivery. While total internal reflection was already discovered in 1842 [2] the first optical fiber featuring two glass components was not fabricated until 1958 [3]. Within the next ten years the technology of fiber fabrication and light detection was mastered, and the Nobel prize of 2009 [4–7] honored the pioneers of this time. Since late 60's the improved fabrication has led to lower losses and increasing data rates in optical fibers, recently passing the 100 Tbit/s mark [8].

The physical basis for this amazing engineering development is the management of two optical effects: chromatic dispersion and the nonlinear optical Kerr effect, in particular, self-phase modulation. Modern fiber design methods for solid core fibers enable considerable control of these two parameters, eliminating dispersion to leading order and suppressing or enhancing nonlinearities by orders of magnitude. This work will explore these limitations in context of ultrashort pulses, i.e., at sub-50-fs duration.

For such extremely short pulses and extremely high peak intensities, standard telecom fibers cannot be used. However, photonic crystal fibers (PCF) [9] have been found to be most suitable for ultrashort pulses. Despite the recent progress, there are physical constraints limiting the technological capabilities of PCFs. For example, dispersive broadening can never be completely eliminated as higher dispersion orders take over when second-order dispersion is removed for one wavelength. This limitation rendered transmission of sub-50 fs pulses over sizable distances impossible prior to the work described in this thesis. While the nonlinearity needs to be minimized for the pulse transmission, there are other applications that greatly benefit from an enhanced optical nonlinearity. This work introduces a method to control the nonlinearity of a PCF by filling the core with liquid. The generation of a two-octave spanning white-light supercontinuua with unprecedented power in such a liquid core fiber is described.

Finally, an implementation of an all-optical transistor is demonstrated in a standard PCF. While electrons in an electronic transistor exhibit a strong interaction, the photons in a photonic transistor will not interact with each other since they are bosons. To observe an interaction between photons, both a nonlinear optical medium and high intensities are required. The extreme confinement in a PCF is therefore beneficial yet still not sufficient for the nonlinear interaction required to switch a strong pulse with a weak one. This work will experimentally show that there are ways to significantly enhance the nonlinear interaction, overcoming previous limitations for implementing an all-optical transistor with good switching contrast. This concept only requires a careful

engineering of the dispersion profile. Optical devices based on the demonstrated effect promise to be the next step towards future applications of optical computing, data processing and telecommunications.

All the experiments together will demonstrate a control of linear and nonlinear effects inside a fiber previously considered widely impossible.

2 Ultrashort pulses and their propagation

This introduction will give a brief overview about the mathematical model for ultrashort laser pulses and their propagation. It will provide the mathematical tools to understand the physics discussed in this work. The focus is on a coherent description of different phenomena observed inside optical fibers. First the linear and nonlinear propagation in a transparent medium are discussed and then some fiber specific propagation phenomena are explained, as far as they are relevant for this work.

2.1 Mathematical description of ultrashort laser pulses

The connection between the electric field $\vec{E}$ and the magnetic induction $\vec{B}$ of an ultrashort laser pulse is determined by Maxwell's equations [10], dating back to 1861. In a more recent formulation using SI units these equations read as [11]:

$$\nabla \vec{D} = \rho \tag{2.1}$$

$$\nabla \vec{B} = 0 \tag{2.2}$$

$$\nabla \times \vec{E} = -\frac{\partial \vec{B}}{\partial t} \tag{2.3}$$

$$\nabla \times \vec{H} = \vec{J} + \frac{\partial \vec{D}}{\partial t}, \tag{2.4}$$

with ρ being the charge density, $\vec{J}$ the current density, $\vec{D} = \epsilon_0 \vec{E} + \vec{P}$ the electric displacement field in a medium with the polarization $\vec{P}$, $\vec{H} = \vec{B}/\mu_0 - \vec{M}$ the magnetic field in a medium with the magnetization $\vec{M}$. In the case of a isotropic medium, the equation spells out as $\vec{D} = \epsilon \vec{E}$ and $\vec{B} = \mu \vec{H}$, with ϵ denoting the scalar electric permittivity and μ the magnetic permeability. Further, if the medium has no free currents and free charges ($\vec{J} = 0$ and $\rho = 0$), Eq. 2.4 can be transformed into a wave equation for the electric and magnetic field:

$$\nabla^2 \vec{E} - \epsilon\mu \ddot{\vec{E}} = 0 \tag{2.5}$$

$$\nabla^2 \vec{H} - \epsilon\mu \ddot{\vec{H}} = 0. \tag{2.6}$$

The laser pulses as discussed in this work are one solution of this equation set and are completely described by the electric field $\vec{E}(t, \vec{x})$ as a function of time and spatial coordinates. For linearly polarized light, the full three-dimensional ansatz is reduced to a scalar field. Even if the light is not linearly polarized, the field components can be separated and treated independently. Only nonlinear effects can cause an interaction

between the different polarization components.

In a mode-locked ultrashort laser pulse the electric field is understood as a superposition of plane waves of different frequency but with a fixed phase [12]:

$$E(t,z) = \frac{1}{\sqrt{2\pi}} \int_{-\infty}^{\infty} \tilde{\mathcal{E}}(\omega,z) e^{i\omega t} \mathrm{d}\omega = \mathfrak{F}\left\{E(\omega,z)\right\}. \tag{2.7}$$

Here $\tilde{\mathcal{E}}(\omega,z) = \left|\tilde{\mathcal{E}}(\omega,z)\right| e^{i\phi(\omega,z)} = \tilde{E}(\omega) e^{i\phi(\omega,z)}$ is a complex spectral amplitude of one plane wave. Since the field $E(t,z)$ is a real quantity, $\tilde{\mathcal{E}}(\omega,z)$ must be self-adjoint, i.e., $\tilde{\mathcal{E}}(\omega,z) = \tilde{\mathcal{E}}^*(-\omega,z)$. Applying a Fourier transform gives the description in the temporal domain. Here the complex field amplitude $\mathcal{E}^+(t,z)$ is given by the integral over positive frequencies only:

$$\mathcal{E}^+(t,z) = \frac{1}{\sqrt{2\pi}} \int_{0}^{\infty} \tilde{\mathcal{E}}(\omega,z) e^{i\omega t} \mathrm{d}\omega. \tag{2.8}$$

The real field of the pulse is determined by $E(t,z) = 2Re\left[\mathcal{E}^+(t,z)\right]$. According to this time domain picture, the positive spectrum in the frequency domain is defined by:

$$\begin{aligned} \tilde{\mathcal{E}}^+(\omega,z) &= \tilde{\mathcal{E}}\,, & \omega \geq 0 \\ \tilde{\mathcal{E}}^+(\omega,z) &= 0\,, & \omega < 0. \end{aligned} \tag{2.9}$$

The fields in the time and frequency domain are connected via the Fourier transform:

$$\mathcal{E}^+(t,z) = \mathfrak{F}\left\{\tilde{\mathcal{E}}^+(\omega,z)\right\}. \tag{2.10}$$

For the pulses discussed here, only a small range of frequencies $\Delta\omega$ around the carrier frequency ω_c contribute to the spectral amplitude. If $\Delta\omega$ is small compared to ω_c, the carrier frequency can be also separated in the time domain. By substituting $\omega \rightarrow \omega_\mathrm{c} + \Delta\omega$:

$$\tilde{\mathcal{E}}^+(t,z) = e^{i\omega_\mathrm{c} t} \frac{1}{\sqrt{2\pi}} \int_{\infty}^{\infty} \tilde{\mathcal{A}}(\Delta\omega,z) e^{i\Delta\omega t} \mathrm{d}\Delta\omega \tag{2.11}$$

$$= A(t,z) e^{i\phi(t,z)} e^{-i\omega_\mathrm{c} t}. \tag{2.12}$$

$\mathcal{A}(t,z)$ is the Fourier transform of the spectral amplitude shifted by ω_c. Here the electric field is described only by the temporal amplitude ($A(t,z)$) and phase ($\phi(t,z)$). This approximation is usually referred to as slowly-varying envelope approximation (SVEA) [13]. Applying the SVEA the propagation equation is simplified into a much simpler differential equation [13]. This differential equation is derived directly from the wave equation Eq. 2.6:

$$\frac{\partial}{\partial z} \tilde{\mathcal{A}}(\Delta\omega,z) + i\Delta k \tilde{\mathcal{A}}(\Delta\omega,z) = 0. \tag{2.13}$$

Note that the SVEA is only valid as long as the variation of the envelope is either slow

compared to one cycle of the carrier oscillation, and long compared to the wavelength:

$$\left|\frac{\partial \mathcal{A}}{\partial z}\right| << |k(\omega_c)\mathcal{A}| \text{ , or } \left|\frac{\partial \mathcal{A}}{\partial t}\right| << |\omega_c \mathcal{A}| . \tag{2.14}$$

Modern laser sources with a pulse duration no longer than a few optical cycles often generate a field which violates the criteria of this approximation. Whether or not the approximation can be used, depends on the pulse shape and the carrier wavelength [14], i.e., given a sech^2 temporal envelope with a FWHM of 10 fs and a carrier wavelength $\lambda_0 = 800\,\text{nm}$, the right side of Eq. 2.14 is only 10 times the left side and the ceiling of the approximation is already reached. For any shorter pulses at this specific wavelength, the SVEA would violate the phase-independent energy conservation. The need for a complete description of shorter pulses and even single cycle pulses has lead to the development of more advanced theoretical descriptions of the electric field [14–16], without the restrictions of Eq. 2.14.

2.2 Linear propagation in transparent media

A part of this work will focus on the linear propagation of light in a specially designed optical fiber. The propagation of light is called linear when the polarization in the medium ($\vec{P}$) depends linearly on the electric field $\vec{E}$. The polarization has its origin in the displacement of the electric charges in the medium, as a consequence the polarization is actually never strictly linear, since it always depends on the electric potential of the medium's charges. However, for small electric fields the linear approximation is justified and delivers excellent results. For the linear propagation, Eq. 2.13 can be solved by the following ansatz:

$$\tilde{\mathcal{A}}(\omega, z) = \tilde{\mathcal{A}}(\omega, 0) e^{i\Delta k z} e^{-\alpha z} \tag{2.15}$$

Each frequency component of the field receives a linear phase shift $\phi(\omega, L)$ during the propagation of the distance L in the media. The absolute value of the phase shift depends on the dispersion properties of the medium:

$$\phi(\omega, L) = L\Delta k(\omega) = L\frac{\omega}{c_0} n(\omega). \tag{2.16}$$

The spectral phase ϕ is here developed into a Taylor series at the carrier frequency ω_c

$$\phi(\omega, z) = \sum_{m=0}^{\infty} b_m(\omega, z)(\omega - \omega_c)^m, \tag{2.17}$$

with the Taylor coefficients being:

$$b_m(\omega, z) = \frac{1}{n!}\frac{\partial^n \phi(\omega, z)}{\partial \omega^n}|_{\omega=\omega_c}. \tag{2.18}$$

The dispersion properties in transparent media as well as in waveguides are given by

a set of propagation parameters $\beta_m(\omega)$. The parameters can be derived directly from Eq. 2.18 according to $\beta_m(\omega) = m! \frac{b_m}{z}$. In most cases the first three parameters already cover all relevant physical effects of the propagation:

$$\beta_1 = \frac{1}{c}\left(n + \omega\frac{dn}{d\omega}\right) = \frac{1}{v_\mathrm{g}}, \tag{2.19}$$

$$\beta_2 = \frac{1}{c}\left(2\frac{dn}{d\omega} + \omega\frac{d^2n}{d\omega^2}\right), \tag{2.20}$$

$$\beta_3 = \frac{1}{c}\left(3\frac{d^2n}{\omega^2} + \frac{\omega d^3n}{d\omega^3}\right). \tag{2.21}$$

Some of the introduced parameters are individually named, as are some related and derived parameters:

- β_2 is known as *group velocity dispersion* (GVD),
- $2 \cdot b_2$ is known as *group delay dispersion* (GDD),
- $3! \cdot b_3$ is known as *third order dispersion* (TOD),
- $T_\mathrm{p} = z/c_0 n(\omega_\mathrm{c}) = z/v_\mathrm{p}$ is known as phase delay,
- $T_\mathrm{g} = z/v_\mathrm{g}$ is known as *group delay* (GD).

The difference between T_p and T_g describes the group phase offset, which causes a slip of the field oscillation under the envelope. The change of the pulse envelope function during the propagation in z-direction is estimated analytically for different pulse shapes in [17]. In the case of a Gaussian pulse with only applying GVD, when all higher orders of dispersion are zero, this will conserve the pulse shape and only cause a broadening of the pulse. Including the higher order dispersion terms, the pulse could also broaden asymmetrically. An analytical approximation for the RMS (root mean square) width of the pulse is found:

$$\sigma(L) = \sigma_0\sqrt{\left(1 + \frac{C\beta_2 L}{2\sigma_0^2}\right)^2 + \left(\frac{\beta_2 L}{2\sigma_0^2}\right)^2 + (1+C^2)^2\frac{1}{2}\left(\frac{\beta_3 L}{4\sigma_0^3}\right)^2}, \tag{2.22}$$

with C being the chirp parameter of the input pulse [17].

Connection between loss and dispersion

The last term in Eq. 2.15 introduced the wavelength dependent loss for linear propagation in transparent media. The loss describes the continuous exponential attenuation of light propagating in a medium and is closely connected to the dispersion of the medium. Both are derived from the frequency dependent dielectric constant which is defined as:

$$\epsilon(\omega) = \left(n(\omega) + i\frac{c}{2\omega}\alpha(\omega)\right), \tag{2.23}$$

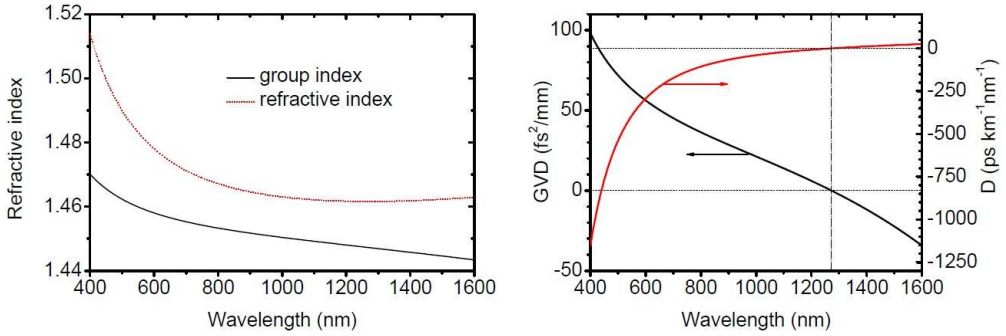

Figure 2.1: *Left:* The refractive index n (red line) and the group index n_g (black line) of fused silica, calculated with the Sellmeier equation Ref. [20] *Right:* The GVD β_2 (black line) and D (red line) calculated for fused silica. The dispersion changes from normal to anomalous dispersion at the zero dispersion wavelength of $\lambda = 1.27\,\mu$m.

together with Eq. 2.18 this results in

$$\beta(\omega) = n(\omega)\frac{\omega}{c} \propto \Re\left(\epsilon(\omega)\right) \tag{2.24}$$

$$\alpha(\omega) \propto \Im\left(\epsilon(\omega)\right). \tag{2.25}$$

Since the real and imaginary part are mathematically separated in the equations for a linear propagation, the complex effective refractive index is used to simultaneously handle both the dispersion and loss of the propagation:

$$n_{\text{eff}} = n(\omega) + i\alpha(\omega). \tag{2.26}$$

In a microscopic picture the loss and the dispersion are fundamentally connected via an integral transformation, the so called Kramers Kronig relation in optics [18, 19].

2.2.1 Example: Dispersion of fused silica

In this example a frequently used optical material and its material parameters are introduced. Fused silica is an important material since it is used as a host material for the dopant in most optical fibers. The dispersion parameters β_m and b_m are derived directly from the refractive index $n(\omega)$ of the material, e.g., [21]. The refractive index has been measured for a wavelength range covering all common laser wavelengths. The experimental data for most of the common material is listed. Since the refractive index describes the medium's response to the electromagnetic wave interacting with the bound electrons, it depends on the specific position of the medium resonance frequencies. For wavelength far from the mediums resonances the refractive index is well approximated

by the Sellmeier equation [22]:

$$n^2(\omega) = 1 + \sum_{j=1}^{m} \frac{B_j \omega_j^2}{\omega_j^2 - \omega^2}, \tag{2.27}$$

with B_j the strength of the resonance located at ω_j. The sum needs to extend over all resonances contributing to the wavelength range of interest. In case of the visible and infrared spectral range usually three resonances and six coefficients are sufficient to fit the experimental data. The Sellmeier coefficients for fused silica are found in Ref. [20]. Figure 2.1 (right) plots the refractive index of fused silica as well as the group index, the slope of this curve and the average value of $n \approx 1.45$ is low compared to most other glasses. The dispersion parameter $\beta_2(\omega)$ as shown in Fig. 2.1 (left) is calculated according to Eq. 2.21. The point $\beta_2 = 0$ is referred to as zero dispersion wavelength (ZDW). In fused silica the ZDW is near $1.27\,\mu$m. The wavelengths with positive β_2 are called wavelengths with normal dispersion and wavelengths with negative β_2 are called wavelengths with anomalous dispersion. While a positive GVD always increases the pulse duration (see Eq. 2.22), negative GVD can, given a negative pre-chirp, lead to a decrease in duration for a certain propagation length, before the pulse eventually broadens.

2.3 Nonlinear propagation of ultrashort pulses

Chapters 5 and 6 will deal with various nonlinear effects during the propagation in an optical fiber. In this section the concept of a nonlinear polarization is developed; first for a general transparent medium, and then two fiber specific nonlinear effects (the self and the cross-phase modulation) are introduced, still for a general medium. Second, a nonlinear propagation equation is developed. Finally the soliton fission process is introduced as an example of a combination of different nonlinear effects in a fiber.

The propagation is called nonlinear if the extreme field amplitude leads to an extreme field gradient and a nonlinear polarization response of the medium. In this case $\vec{P}$ no longer depends linearly on $\vec{E}$ and the light changes the optical properties of the medium it propagates in. Still, this nonlinear change is small and the nonlinear polarization P_{NL} is small compared to the linear polarization P_{L}. The total polarization is developed in a power series for the electric field strength:

$$P(t) = P_{\mathrm{L}}(t) + P_{\mathrm{NL}}(t) = \chi^{(1)}E(t) + \chi^{(2)}E^2(t) + \chi^{(3)}E^3(t)..., \tag{2.28}$$

with $\chi^{(1)}$ the linear and $\chi^{(i)}$ $(i > 1)$ the nonlinear susceptibilities of the medium. Mathematically these susceptibilities are tensors of the rank $i + 1$ and in general become unhandy because of the high number of entries. A contracted notation is common [23] and symmetry arguments further reduce the number of independent tensor elements [24]: The materials appearing in this work are liquids, gases, and amorphous solids (glasses). All of these materials are centro-symmetric, i.e., their electric potential is symmetric. For this reason their $\chi^{(2)}$ vanishes identically [23]. Second-order nonlinear effects, such

as second harmonic generation or sum-/difference frequency generation, will not be observed in these materials. The dominant nonlinear effects are third-order linear effects. The corresponding third order nonlinear polarization is generated, in the time domain oscillating with the frequency ω, and its component i is given by:

$$P^{(\omega)}_{\mathrm{NL},i} = \epsilon_0 \chi^{(3)}_{ijkl}(\omega;\omega_1,\omega_2,\omega_3,) E^{(\omega_1)}_j(t) E^{(\omega_2)}_k(t) E^{(\omega_3)}_l(t). \tag{2.29}$$

Here, four electric fields are involved, and these effects are referred to as four-wave mixing (FWM). A large variety of effects are possible but most of them are restricted because of a phase matching condition. Since the direction of the wave-vector is parallel to the propagation direction and fixed for any propagating mode in the fiber, phase matching can only be observed if the absolute value of the vectors are also equal. This is usually not the case for the fundamental and any of its harmonics. In fact in most fibers the phase matched frequencies are in far spectral distance to each other. This way the number of important nonlinear effects in a fiber is drastically reduced. Degenerate four-wave mixing (DFWM) processes are the dominant nonlinear effects observed in fibers, since these are always perfectly phase matched. The nonlinear contribution of DFWM to the polarization is described by:

$$P_{\mathrm{NL}}(t,z) = \epsilon_0 \chi^{(3)}_{\mathrm{eff}}(\omega_\mathrm{c};\omega_\mathrm{c},\omega_\mathrm{c},-\omega_\mathrm{c}) \left|E(t,z)\right|^2 E(t,z). \tag{2.30}$$

With $\chi^{(3)}_{\mathrm{eff}}$ the effective susceptibility for the DFWM process. Using Eq. 2.29 the total polarization reads as:

$$P(t) = \epsilon_o \left[\chi^{(1)} + \chi^{(3)}_{\mathrm{eff}} \left|E(t,z)\right|^2\right] E(t,z). \tag{2.31}$$

Here again is $P = \epsilon E$, however, with ϵ depending on the Intensity $I(z,t) = |E(t,z)|^2$. The new intensity dependent refractive index of the medium is given by $n = \sqrt{\epsilon}$ and found to be:

$$n(I) = n_\mathrm{L} + n_\mathrm{NL} = n_\mathrm{L} + n_2 I(z,t). \tag{2.32}$$

The nonlinear third order response of the medium is described by a new material parameter, the nonlinear refractive index

$$n_2 = \frac{3\chi^{(3)}\left(\omega_\mathrm{c};\omega_\mathrm{c},\omega_\mathrm{c},-\omega_\mathrm{c}\right)}{8 n_\mathrm{L}}. \tag{2.33}$$

Its unit is $[n_2] = \mathrm{m}^2/\mathrm{W}$, e.g., the value for fused silica is measured to be $2.7 \times 10^{-16}\mathrm{cm}^2/\mathrm{W}$. A significant change of n is observed for peak powers of several GW or more, which are easy to obtain with ultrashort laser pulses. A medium showing this intensity-dependent refractive index is called a Kerr-medium and the effect is called the Kerr-effect.

2.3.1 Self-phase modulation

One of the most prominent effects caused by the nonlinear refractive index is the Self-phase modulation (SPM). The temporal change of the pulse intensity causes a temporal change of the refractive index, which in return changes the temporal phase of the pulse. As mentioned above, the electric field after a propagation over a distance L is $E(t,L) = A(t,L)e^{-i\omega_c t}e^{i\phi(t,L)}e^{i\phi_{\mathrm{NL}}(t,L)}$ (c.f. Eq. 2.12). The nonlinear contribution to the phase after a propagation is:

$$\phi_{\mathrm{NL}}(t,L) = -\frac{\pi L}{\lambda}\delta n(t), \tag{2.34}$$

With the nonlinear refractive index change given by [25]:

$$\delta n(t) = \frac{n_2}{t}\int_{-\infty}^{t} \mathrm{d}t' A^2(t) e^{\frac{t-t'}{\tau}}. \tag{2.35}$$

The relaxation time τ is the key parameter to determine the character of the SPM effect. If the Kerr-effect is instantaneous ($\tau = 0$), the change of the instantaneous frequency $\delta\omega = \mathrm{d}\phi/\mathrm{d}t$ is proportional to the gradient of the intensity $-\mathrm{d}I/\mathrm{d}t$ and the frequency broadening occurs on both sides of the spectrum [26]. In case $\tau \neq 0$ and τ is sufficiently large, the change follows the intensity linearly and the spectrum broadens only on the low frequency (red) side. For an asymmetric pulse shape, an asymmetric broadening will be observed. The broadening of the pulse is for example used to generate a pulse significantly shorter than the initial pulse. This, of course, requires compensation of the the nonlinear phase and realignment of the new spectral components in time, after the SPM process. If the nonlinear phase vastly exceeds values of the original phase $\phi(t)$, the temporal structure of the pulse is severely distorted and the re-compression is practically impossible.

2.3.2 Cross-phase modulation between two pulses

Chapter 6 will deal with two pulses co-propagating in a fiber. In this case both electrical fields contribute to the nonlinear polarization and additional nonlinear effects are observed. The dominant effect for co-propagating pulses is cross-phase modulation (XPM). The literature reports on two kinds of XPM, first on the interaction between two states of polarization at the same wavelength and second the interaction of two different wavelengths. In this work XPM is restricted to only the nonlinear interaction between two linearly polarized pulses of different carrier frequencies ω_i and ω_j with the same polarization direction. The pulses are separated in the frequency domain in such a way that their spectra do not overlap, i.e., no linear interaction can be observed. Two electric fields give arise to a nonlinear polarization oscillating at ω_j, ω_i, $2\omega_j - \omega_i$, and $2\omega_i - \omega_j$. The new frequencies $2\omega_j - \omega_i$ and $2\omega_i - \omega_j$ created in a FWM process are considered not to be phase-matched and are neglected. The remaining two contributions at ω_j and ω_i are $P_{\mathrm{NL}}^{i,j} = \frac{3\epsilon_0}{4}\chi^{(3)}(|E_{i,j}|^2 + 2\,|E_{j,i}|^2)E_{i,j}$ and the total induced polarization reads as

$$P_j = \epsilon_0 \epsilon_j E_j, \tag{2.36}$$

with $\epsilon_j = \epsilon_j^L + \epsilon_j^{\mathrm{NL}} = (n_j^L + n_j^{\mathrm{NL}})^2$. Using the same approximation as used in Eq. 2.32 ($n_{i,j}^{\mathrm{NL}} << n_{i,j}^L$) and $n_i^L \approx n_j^L$ the nonlinear refractive index is given by:

$$n_{i,j}^{\mathrm{NL}} \approx n_2(|E_{i,j}|^2 + 2\,|E_{j,i}|^2)E_{i,j}, \tag{2.37}$$

with the same n_2 as introduced in the Eq. 2.32. The first term of Eq. 2.37 shows the nonlinear index change induced by the field to itself (SPM) and the second term changes the refractive index proportional to the intensity of the co-propagating electric field (XPM). The nonlinear change in the refractive index causes a change in the phase of the field exactly as in Eq. 2.34, however, this time the δn depends on the intensity of both co-propagating fields. For an instantaneous Kerr-effect, Eq. 2.37 results in $\delta n_j = n_2(I_j + 2I_i)$ and the XPM is always twice as effective as the SPM. It is noteworthy that SPM and XPM always occur together.

2.3.3 Nonlinear propagation equation

In order to mathematically describe the nonlinear propagation of ultrashort laser pulses in transparent media, the slow Raman effect needs to be included in the mathematical model, not just the virtually instantaneous Kerr-effects. The source of the Raman effect is the inelastic scattering of photons on phonons in the glass or crystal lattice. Depending on the type of phonon, the effect is either called Raman (optical phonon) or Brillouin scattering (acoustic phonon). Typically, response times in fibers range from a few femtoseconds to some hundred femtoseconds [27]. A nonlinear propagation equation is derived by solving the wave equation of nonlinear propagation:

$$\nabla^2 E - \frac{1}{c}\frac{\partial^2 E}{\partial t^2} = \mu_0 \frac{\partial^2 P_L}{\partial t^2} + \mu_0 \frac{\partial^2 P_{\mathrm{NL}}}{\partial t^2}. \tag{2.38}$$

Here the SVEA and some algebra is used to transform the above equation into the so called nonlinear Schroedinger equation (NLS) [28, 29] for an optical single mode fiber:

$$\begin{aligned} &\frac{\partial A}{\partial z} + \frac{1}{2}\left(\alpha(\omega_0) + i\alpha_1 \frac{\partial}{\partial t}\right) A + \beta_1 \frac{\partial A}{\partial t} + i\frac{\beta_2}{2}\frac{\partial^2 A}{\partial t^2} - \frac{\beta_3}{6}\frac{\partial^3 A}{\partial t^3} \\ &= i\left(\gamma(\omega_0) + i\gamma_1 \frac{\partial}{\partial t}\right)\left(A(z,t)\int_0^\infty R(t')\,|A(z,t-t')|^2\,\mathrm{d}t'\right), \end{aligned} \tag{2.39}$$

with α_1 and γ_1 being the first coefficients from a Taylor expansion of the absorption and the nonlinear parameter. The use of this Taylor expansion implies that both α and γ are frequency dependent quantities and also n_s is frequency dependent. The parameter γ_1 in Eq. 2.39 is causing the self steepening of the pulse. Equation 2.39 is usually referred to as extended NLS [17] and describes the propagation accurately as long as the SVEA is valid.

The nonlinear response function in the integral part of the NLS describes the electronic and the nuclear nonlinear response of the medium. A common form for this response

function is [27]:

$$R(t) = (1 - f_\mathrm{R})\delta(t - t_e) + f_\mathrm{R} h_\mathrm{R}(t), \tag{2.40}$$

with $h_\mathrm{R}(t)$ the Raman response function, t_e the delay of the electronic response and f_R the Raman fraction. The Raman response function cannot be analytically derived for an amorphous material such as glass. Different experimental methods have been developed to measure typical delay times and amplitudes and to create realistic models for $h_\mathrm{R}(t)$, e.g., [27, 30]. With a proper description of h_R the extended NLS can be used to describe the nonlinear propagation of pulses as short as a few optical cycles, if enough higher dispersion orders are included [14, 31–33]. However, as soon as the SVEA is violated, the NLS can not be used to describe the nonlinear propagation. Important consequences of the Raman effect on ultrashort pulses in an optical fiber are the intrapulse Raman scattering resulting in a red shift of the pulse spectrum and the formation of Raman solitons.

2.3.4 Soliton fission and supercontinuum generation

So far, a number of nonlinear effects have been discussed separately, however, as Eq. 2.39 indicates, all effects contribute to the nonlinear propagation at all times. In bulk media, sometimes one effect dominates the others and can be studied in isolation. However, in fibers as discussed in this work all effects are contributing almost equally. Interesting new phenomena are observed as a result of a balance and cascadation of different nonlinear effects. The supercontinuum (SC) generation in a PCF first demonstrated by Ranka [34] is a typical example for such a cascaded effect. The effect can not be explained by a single nonlinear effect, especially not by SPM alone. The octave spanning white-light generation was first explained as soliton fission by Husakou et al. [35], and also experimentally verified [36].

Figure 2.2 illustrates the supercontinuum generation during the propagation in a typical photonic crystal fiber. The main requirement for an efficient SC generation is that the initial pulse is propagating close to the zero dispersion wavelength (ω_ZDW) of the fiber in the negative dispersion regime. The dispersion is depicted as a gray line. Under this condition the pulse forms a higher-order soliton with the soliton number given by $N = \tau_0 / |\beta_2(\omega_0)|$. This soliton exists as a result of a balance between SPM and GVD and periodically broadens in both the time and frequency domain. Because of the high TOD (green dashed line) at the ZDW the high order soliton fissions subsequently into a number of fundamental soliton (N=1) whenever it has reached its maximum width in the spectral domain. The earlier the fundamental soliton splits off from the high order soliton, the higher its amplitude and group velocity and the shorter its duration. These solitons are then red shifted by the Raman effect during their propagation. Each fission process gives rise to the emission of phase matched non-solitonic radiation (NSR [37], blue) at blue frequencies. This NSR is understood as phase-matched FWM process, which also explains the blue shift according to the red shift of the associated soliton [38–40]. Since the NSR is located in the normal dispersion part of the spectrum it propagates not as a soliton but as a dispersive wave. This soliton fission process explains the octave

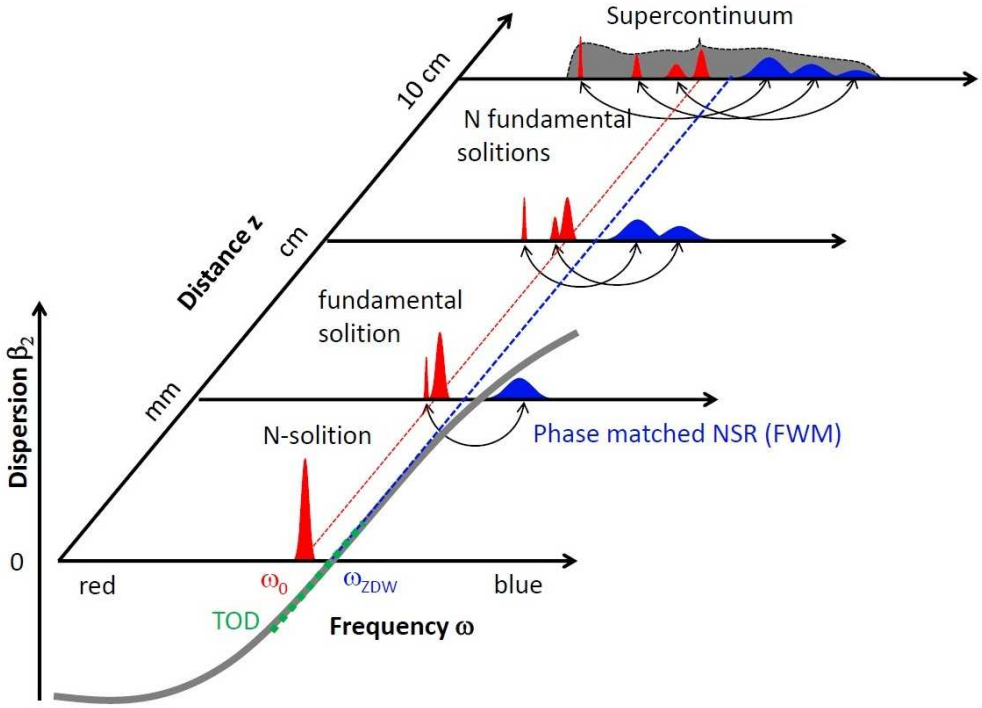

Figure 2.2: Schematic of supercontinuum generation based on soliton fission. The pulse starts its propagation as a high order soliton at negative dispersion close to the zero dispersion wavelength. Because of the high third order dispersion, the input soliton fissions into N fundamental solitons, which are subsequently Raman shifted towards the red. Each fission process gives rise to the emission of non-solitonic radiation at blue frequencies and the non-solitonic radiation propagates as a dispersive wave. In a cascadation of this process the supercontinuum is created. The distances given on the z-axis may vary with the energy and wavelength of the input pulse.

spanning supercontinuum generation in fibers.

2.4 Optical fibers

Optical fibers are an important development of the 20th century [4, 5]. They have revolutionized communication networks and have also found many different applications in all fields of science and technology. The majority of fibers are made from ultra-pure amorphous silicon dioxide (silica) with or without a dopant. The typical optical fiber has a core region of about $2-30\,\mu$m diameter surrounded by a cladding layer of $100-250\,\mu$m width and is jacketed with a polymer protection coating. Most fibers are all solid and the core has a higher refractive index than the cladding due to a special doping of the core and/or the cladding. A fiber can support many electromagnetic field modes propagating in the core, the cladding, and even on the surface between core and cladding. A fiber which only supports a single electromagnetic mode in the core is called a single-mode fiber, whereas a multimode fiber allows for many modes to propagate at the same time in the core. Today a zoo of fibers for different purposes is available, the following section will only describe a small part of them and will focus on the photonic crystal fibers.

2.4.1 Index guiding fibers

Most of the fibers used today have high index core and at least one low index cladding layer. The guiding mechanism in these fibers is named index guiding and can be understood by total internal reflection on the interface between core and cladding. This explanation uses the ray-picture of light propagation but the index guiding equally be explained in the wave picture. The important parameters for such a fiber are the core diameter (d_{core}) and the numerical aperture $\mathrm{NA} = 1/n_0\sqrt{n_{\mathrm{core}}^2 - n_{\mathrm{cladding}}^2}$. The latter is determined by the refractive indices of the core (n_{core}) and cladding (n_{cladding}). The number of modes supported in such a fiber scales with the square of the so called V number ($V = 2\pi/\lambda d_{\mathrm{core}}\mathrm{NA}$) and a fiber is a single-mode fiber when V is smaller than ≈ 2.405. The NA also determines the maximum acceptance angle ($\sin\theta_{\mathrm{max}} = \mathrm{NA}/n_0$) of the fiber. If the fiber parameters and the wavelength are well chosen, light can propagate over many kilometers in a single-mode fiber, the internal loss is typically in the range of 0.2 dB/km for a silica fiber.

2.4.2 Photonic crystal fibers

Compared to the index guiding fibers, photonic crystal fibers are rather new and complicated to fabricate. They are named because of their microstuctured cladding, which acts as an artificial crystal for light. The first attempts to realize such fibers were made in the 1970s by Kaiser et al. [41]. Since major improvements in the early 1990s [42], the stack and draw technique today allows for reliable fabrication of such fibers. Many research groups are able to draw microstructured fibers and even a small number of commercial fibers are available. Within only a few years PCFs have achieved major significance in many research applications. However, only a small number of commercial applications

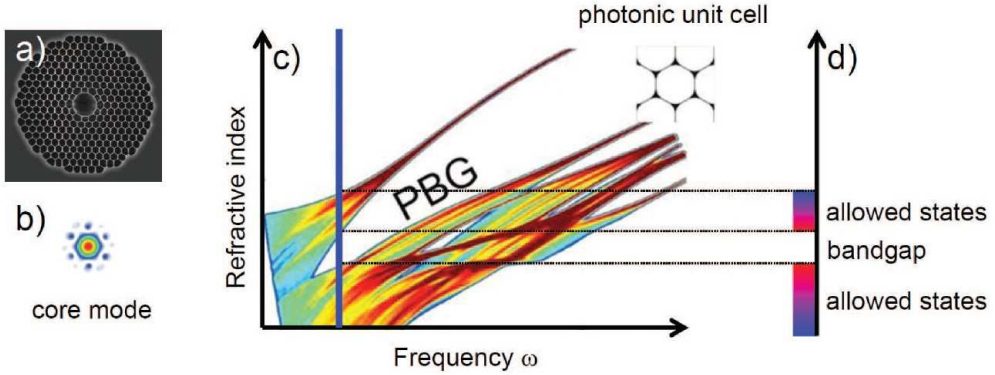

Figure 2.3: Illustration of bandgap guiding: (a) A micrograph of a typical bandgap guiding PCF. (b) The core mode calculated for this type of PCF. (c) The density of optical states in a bandgap fiber features bandgaps with no optical states. (d) A cross-section of the density of optical states at a single frequency [indicated as a blue line in (c)], illustrating the photonic bandgap. The density of optical states data is taken from [44].

have been developed thus far. Most fibers are made from a uniform glass with easy-to-handle thermo-mechanical properties [9, 43]. The appearance of PCFs may vary a lot: solid core and hollow core fibers are very common. It is useful to categorize the PCFs by their guiding mechanism, instead of their appearance. This categorization does not depend on the properties of the core, but on the photonic properties of the cladding. The first reported PCFs were basically index guiding fibers. If the size of the holes is in the range of the wavelength and their distance is somewhat smaller than the mode diameter in the core, the mode basically averages the refractive index over the entire microstructure. Since the average refractive index of that microstructure is smaller than the one of the core, index guiding as described above is observed.

With the increasing quality and dimension of the microstructure two new guiding mechanisms were discovered: the photonic bandgap guiding and the quasi guiding. Both mechanism confine a light mode in the the core and allow for low loss guiding over long distances. The understanding of these effects allows engineering of the fiber properties with a great degree of freedom.

2.4.3 Photonic bandgap guiding fibers

The microstructured cladding in a bandgap fiber represents a two-dimensional photonic crystal [45]. Because of the boundary conditions only a limited number of optical frequencies are able to propagate in the photonic crystal structure. In case of an one-dimensional photonic crystal, a band structure of such a photonic crystal can be derived using the same mathematical methods as in solid state physics. The two-dimensional case is usually too complex to be solved analytically. A numerical method needs to be employed to calculate the band structure of such a two-dimensional photonic crystal.

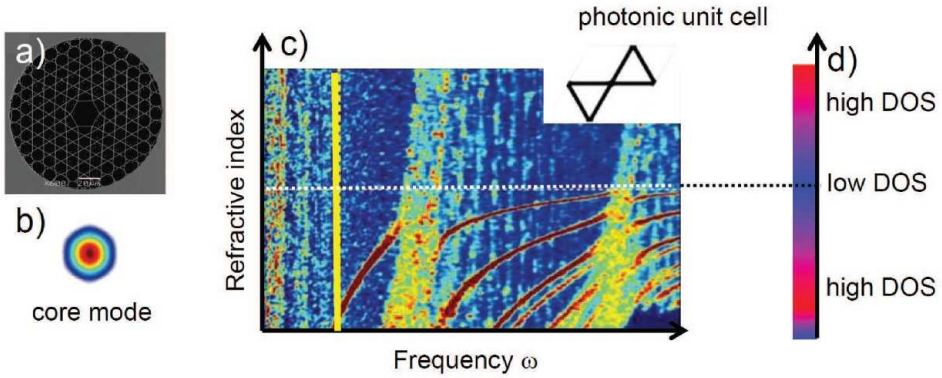

Figure 2.4: Illustration of the quasi guiding: (a) A micrograph of a typical quasi-guiding PCF. (b) The core mode calculated for such a PCF. (c) The density of optical states for a quasiguiding fiber has no bandgaps and is completely populated. (d) The density of optical states at a single frequency [indicates as yellow line in (c)] shows only regions with higher and lower density. The density of optical states data is taken from [44].

The photonic analog to the electronic band structure of a crystal is shown in Fig. 2.3 (c) as the density of optical states (DOS) diagram for a typical bandgap fiber [Fig. 2.3 (a)]. The number of optical states is color coded and displayed over the optical frequency. The plot indicates several white areas of absolutely no optical states; these areas are called photonic bandgap. In Fig. 2.3 (d) the DOS is shown for a specific frequency. This illustrates the concept of bandgap guiding: Any optical mode with an effective refractive index within this bandgap will be confined in the core because their light simply cannot leak trough the cladding. Depending on the manufacturing quality of the microstructure, this guiding mechanism allows for losses well below 1 dB/m [46, 47].This mechanism is also not depending on the refractive index of the core, which is just representing a defect in the crystal structure, i.e., the guiding works even for a hollow core fiber. Such hollow core fiber are of special interest for applications such as spectroscopy and biomedical sensing. Because of the very strict confinement, solid core bandgap fibers are used in supercontinuum generation [34] but also for the realization of single mode large mode area (LMA) fibers.

2.4.4 Quasi guiding fibers

The second important guiding mechanism in PCFs is quasi guiding [48]. Figure 2.4 illustrates this guiding mechanism. Apart from that for the bandgap fiber, the DOS diagram [Fig. 2.4 (c)] for a quasi guiding fiber is completely populated. Given the missing bandgap, virtually loss-less guiding of the core mode is impossible. The core mode can leak into the cladding whenever the core mode is resonant to one of the cladding modes. In such a quasi guiding fiber the cladding is always resonant to at least one cladding mode. However, light can still be guided with low losses in the range of

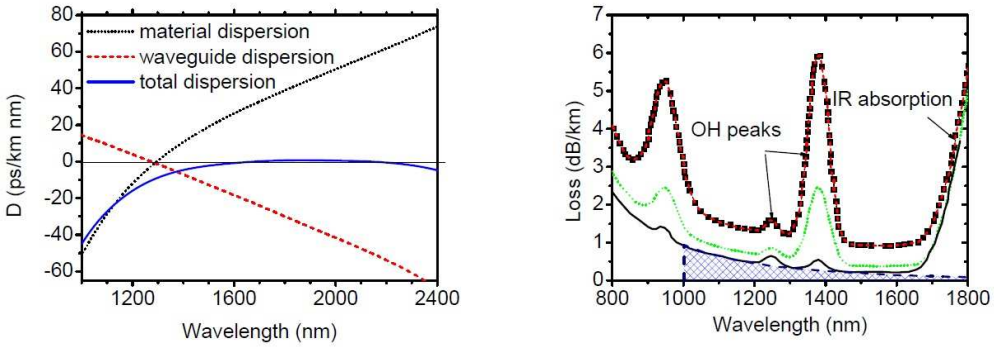

Figure 2.5: *Left:* material (black), waveguide (red) and total dispersion (blue) for an all-solid highly nonlinear fiber. *Right:* Comparison of the loss for single-mode fibers from the early 1980s (red), the late 1980s [51] (green), and recent fiber (black). The theoretical limit of the loss is given by pure Rayleigh scattering and displayed as a blue-shaded area.

a few dB/m if the leaking is small enough. The core mode as shown in Fig. 2.4 (b) is guided as a defect mode in a low DOS region indicatedby blue colors, c.f. Fig. 2.4 (d). These regions are neighbored by regions with high DOS (red colors). In these regions the cladding resonances accumulate, and the loss is dramatically increased.

The main advantage of the quasi-guiding is that very broad connected regions of low DOS are observed, e.g., in Kagome type fibers as shown in Fig 2.4 (a). This makes this guiding mechanism particularly suitable for the guiding of ultrashort laser pulses with an extremely broad spectrum [48]. These spectra exceed the bandwidth of any known photonic bandgap in the same wavelength region. Even several single but isolated strong resonances within the spectrum of such an ultrashort laser pulse do not cause severe distortions in its temporal structure [49]. Furthermore, the quasi-guiding does not rely on a strictly periodic cladding, and the loss [49] as well as the dispersion [50] can be optimized.

2.4.5 Dispersion and loss in a fiber

Dispersion

The dispersion in a fiber constitutes from the material dispersion of the core material (c.f. Sec. 2.2.1) and the waveguide dispersion of the fiber. The latter is a result of geometrical confinement of the light in the core. Especially, when the waveguide dimensions are of the same scale as the center wavelength, the waveguide contribution is changing the global and local dispersion properties significantly.

Figure 2.5 shows the two contributing components and the total dispersion calculated for a simple index guiding highly nonlinear fiber made from fluoride doped glass. It is observed that for wavelength smaller than the core diameter ($d_{\text{core}} = 1.74\,\mu\text{m}$) the waveguide contribution is linear. A linear waveguide dispersion shifts the zero dispersion

wavelength and changes the slope of the total dispersion. For wavelengths longer than the doped core diameter, the waveguide dispersion roles off and causes a second zero dispersion wavelength. Such a behavior is observed for many solid core fiber, regardless of their material and specific guiding mechanism. This includes also the nonlinear photonic crystal fiber used in Ch. 6.

In a hollow core photonic crystal fiber, as discussed in Ch. 4 the material dispersion of air is very small [52], and the waveguide dispersion is dominating the total dispersion. For these fibers usually a resonance-shaped dispersion is observed with linear middle part and roll offs close to the resonances (quasi-guiding fibers) or at the bandgap borders (bandgap guiding). Since there are almost no analytical solutions for the waveguide dispersion in hollow core fiber, numerical mode-solving (c.f. Sec. 3.2.2) is required to calculate the effective refractive index and the dispersion of such fibers. However, in some cases a much simpler approximation is useful [53].

Loss

Similar to the dispersion, also the loss of a fiber has a material and a waveguide contribution. Figure 2.5 (left) illustrates how the total loss in the fiber has been improved in the last decades. The theoretical loss limit in a fiber is given by the Rayleigh scattering (blue shaded area) and decreasing with λ^{-4}. While earlier fibers still had absorption peaks at $1.24\,\mu$m and $1.39\,\mu$m modern fibers made from ultra-pure silica have losses as low as the intrinsic limit. Most glasses however have a high absorption in the infrared spectral region above 3μm wavelength, this absorption is due to vibrational excitation of the glass and cannot be avoided. The waveguide loss is given by the imaginary part of the effective refractive index for the guided mode and therefore directly coupled to the waveguide dispersion via the Kramers-Kronig relation [18, 19]. Especially, in hollow core photonic crystal fibers this waveguide loss contribution is important.

Furthermore, an externally caused loss can be observed, if a fiber is bent too tightly. This so called bending loss is observed for all guiding mechanisms. Physical bending deforms the fiber cross-section in a way that breaks the confinement of the core-mode and leads to a leaking into the cladding. The bending loss can easily exceed all other loss contributions and the leaking of optical power can cause severe damage in the fiber. The critical bending radius depends on the wavelength and the waveguide and can range from a few to a few tens of centimeters.

3 Methods

This chapter covers the important experimental and numerical methods used in this work. The first part will explain the dispersion measurement technique, loss measurements, and the interferometric autocorrelation including an iterative phase retrieval algorithm. The second part will describe the numerical method which is used to calculate the guiding properties of complex photonic structures. Chapters 5 and 6 will also use simulations of nonlinear propagation of ultrashort pulses in media. These simulation are performed in collaboration with Anton Husakou (Max Born Institute) and Ayhan Demircan (Weierstrass Institute). The simulations are based on advanced numerical models and have been performed, based on the data obtained in this thesis. The underlying principles and methods are briefly reviewed when the method is first used.

3.1 Experimental methods

3.1.1 Dispersion measurement techniques

The dispersion of a medium is a key parameter for many experiments in optics. As can already be deduced from the further turn of this thesis: for the propagation of ultrashort pulses the dispersion is one of two critical parameters. In Ch. 4, an extraordinary low dispersion over a broad bandwidth preserves an ultrashort pulse from temporal broadening. In Ch. 5, the zero dispersion wavelength and the dispersion parameters enable soliton formation, which induces the observed nonlinear supercontinuum generation. In Ch. 6, the dispersion, more specifically the group delay, allows for two pulses propagating with similar group velocity.

Usually the dispersion of a fiber is given just as a single parameter β_2 or D at one specific wavelength, and it is sufficient to describe the higher order dispersion by a series of scalar values β_i, as defined in Eq. 2.18. For the propagation of ultrashort pulses with bandwidth easily exceeding 50 nm, the wavelength dependence of the GVD is important. In this work the dispersion is calculated and measured as a function of frequency $\beta_2(\omega)$. This implies that the high order dispersion terms are also frequency dependent and are given by the derivatives of $\beta_2(\omega)$. A precise measurement of $\beta_2(\omega)$ is required for all experiments in this work and many others, e.g., Refs. [54–58]. $\beta_2(\omega)$ describes the change of the group delay, i.e., the change of the relative phase between frequency components. This change can be directly measured in the temporal domain as well as in the spectral domain. Both measurements are absolutely equivalent and, ultimately, the precision of the measurements in both domains are limited by noise [59–61]. In this work the measurements are performed in the spectral domain.

Interferometric dispersion measurement

The measurements use spectral interferometry [62] to measure the phase difference between frequency components. The setup consists of a dispersion balanced Mach-Zehnder type interferometer [63]. At the output port of the interferometer, the spectral interference between the sample and reference arm is measured, and the interference signal is given by:

$$|E_{\mathrm{sig}}|^2(\omega) = |E_{\mathrm{probe}}(\omega) + E_{\mathrm{ref}}(\omega)|^2 \propto \cos\left(2\pi \frac{1}{\tau(\omega)}\right). \tag{3.1}$$

With $\tau(\omega)$ being the temporal delay of the different frequency components. The signal is a spectral fringe pattern. For analysis of this fringe pattern, first the phase of the interferogram φ needs to be retrieved:

$$\varphi(\omega) = \omega\tau_0 + \phi_{\mathrm{ref}}(\omega) - \phi_{\mathrm{sig}}(\omega) = \omega\tau_0 + \Delta\phi(\omega) \tag{3.2}$$

This phase can be extracted with either the Takeda algorithm [64] or a wavelet based algorithm [65]. The first derivative of the extracted phase gives the group delay (GD) of the sample:

$$\frac{\mathrm{d}\varphi(\omega)}{\mathrm{d}\omega} = \tau_0 + \frac{\mathrm{d}\phi_{\mathrm{ref}}(\omega)}{\mathrm{d}\omega} - \frac{\mathrm{d}\phi_{\mathrm{sig}}(\omega)}{\mathrm{d}\omega} = \tau_0 + \mathrm{GD}_{\mathrm{ref}} + \mathrm{GD}_{\mathrm{sig}}. \tag{3.3}$$

From this precise measurement of the group delay $\mathrm{GD}(\omega)$, the dispersion $\beta_2(\omega)$ and the higher order dispersion terms are calculated by successive derivatives of the signal, c.f. Eq. 2.18.

Light source and precision

For the experiments presented in this work, the group delay needs to be precisely measured over a bandwidth covering some 100 nm. In Chapter 4 the latter is achieved with a tunable laser source (Spectra-Physics, Tsunami), which is tuned 5 nm steps from 730 nm to 830 nm. For the spectral range covered in Ch.6 the tunable laser cannot be used and a white-light supercontinuum (NKT Photonics, SuperK) is used instead. In both measurements the precision is limited by the shot-noise [59], and shot noise is proportional to the square root of the number of photons. The light source is the better, the more photons are emitted at the specific wavelength, and the detector is the better, the more photons are detected per time unit. For the measurements presented in this work extensive averaging is used to increase the precision. Unfortunately, even in a perfect setup, the standard deviation of $\beta_2(\omega)$ is proportional to the third power of the inverse spectral resolution [59]. As a consequence, the noise level rises rapidly with increasing resolution and the maximum achieved spectral resolution and precision need to be traded off by an increased measurement time.

3.1.2 Loss measurements

The loss coefficient α describes the attenuation during a propagation in a sample with length l:

$$P_{\text{out}} = P_{\text{in}} e^{-\alpha l}. \tag{3.4}$$

The most straightforward way to measure the loss is to measure the input and output power as well as the length of the sample. However the precision of these measurements is crucial and in general a precise loss measurement averages over a large number of measurements. Typically such a measurements is performed as a cut-back measurement. A series of power $I_0, I_1, \ldots, I_n$ is recorded, while the sample is cut back to length $l_0, l_1, \ldots, l_n$. Saving and measuring the cut parts allows for very precise relative length measurements. The loss is then given by the average over:

$$\alpha_n = \frac{-\ln\left(P_n / P_{n-1}\right)}{l_n - l_{n-1}}. \tag{3.5}$$

In some literature dealing with fiber optics, as an engineering problem, the loss of a fiber is given in the unit dB/m. The conversion formula from α, given in 1/m, into loss α_{dB} in dB/m is:

$$\alpha_{\text{dB}} = \frac{1}{l} 10 \log_{10} \frac{1}{e^{-l\alpha}}. \tag{3.6}$$

3.1.3 Pulse characterization

The characterization of ultrashort laser pulses is a challenging task. In most cases a direct measurement of $E(t)$ or $\mathcal{A}(t)$is not possible for pulse durations smaller than a few picoseconds. Several methods have been developed to gather information about the temporal pulse structure [66]. The spectral phase interferometry for direct electric field reconstruction and frequency resolved optical gating are the most sophisticated approaches and both methods allow for complete characterization of the electric field.

Unfortunately, both methods require measurements in the spectral domain, which requires a certain pulse energy for a detectable signal. Depending on the used setup, wavelength, and the detector type, this critical power level may vary. However, the few nJ pulse energy at a repetition rate only 1 kHz as used in Ch. 4-6 of this work neither allow for none of the complete characterization techniques. The only reliable characterization techniques available are the autocorrelations, which spectrally integrate the signal. Very sensitive detectors can be used and easy-to-use commercial devices are available.

Interferometric autocorrelation

The technique used for the measurements in Ch. 4 and Ch. 6 is the interferometric autocorrelation (IAC) in combination with an iterative pulse reconstruction developed for this work [67, 68]. Figure 3.1 (left) illustrates the setup for an interferometric autocorrelation and Fig. 3.1 (right) shows a calculated example for a IAC signal (black)

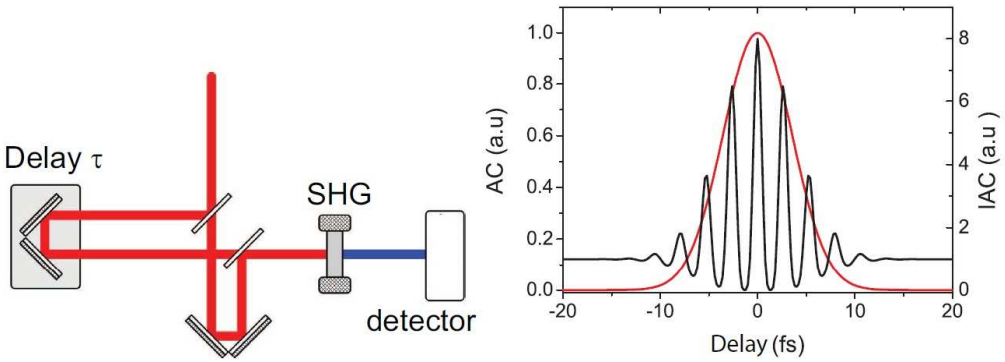

Figure 3.1: Typical setup for the interferometric autocorrelation (IAC). Calculated traces autocorrelation traces of a transform limited Gaussian pulse. The trace for an intensity autocorrelation in red and the interferometric autocorrelation in black.

compared to the signal of an intensity autocorrelation (AC) for the same pulse. The signal interferometric autocorrelation is a convolution of the electric field and shows typical interference fringes. The signal is then given by:

$$\mathrm{IAC}(\tau) = \int_{-\infty}^{\infty} \left| (E(t)E(t+\tau))^2 \right|^2 \mathrm{d}t. \tag{3.7}$$

This measured signal is not background free and the background-to-signal ratio calculated from Eq. 3.7 is 1 : 8. The IAC signal is analyzed by counting the fringes within the FWHM of the signal (N_{fringe}) and no calibrated delay axis is required, since the fringe spacing $\Delta\tau = 1/\nu_0$ is given by the center frequency of the laser pulse. The pulse duration is then estimated with:

$$T_{\mathrm{FWHM}} = \frac{N_{\mathrm{fringe}}\Delta\tau}{B}, \tag{3.8}$$

with B the deconvolution factor for the assumed pulse profile, e.g., 1.897 for a super Gaussian pulse. The the IAC setup is more difficult to adjust than the standard autocorrelation, but the fixed background/signal ratio provides an excellent control mechanism for the adjustment. The collinear setup allows for characterization of ultrashort pulses even as short as just a few optical cycles [69].

Iterative phase reconstruction

It has also been shown that the direct calculation of the temporal pulse structure is impossible. However, a number of different iterative approaches has been reported , e.g., Ref. [70], which allows for iterative retrieval of the temporal pulse structure. These algorithms search for a matching spectral phase that would lead to the recorded auto-

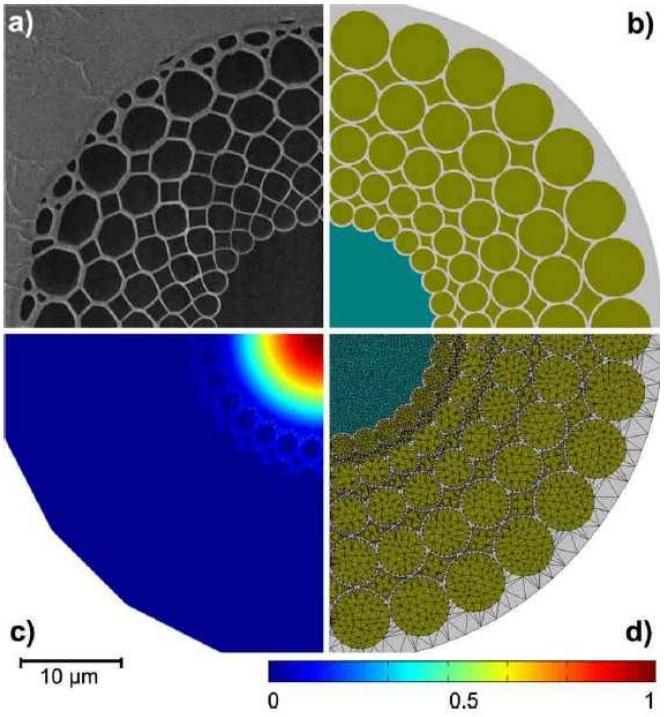

Figure 3.2: Illustration of an FEM calculation. (a) scanning-electron micrograph of a manufactured fiber [50]. (b) Schematics of the geometry of a photonic structure. The hollow core is color-coded in blue-green, gray areas indicate glass cross sections. Hollow regions of the cladding are marked in green. (c) Example of a fundamental mode pattern determined in the numerical simulations computed at 650 nm wavelength. Color coding indicates the modulus of the electric field on a linear scale. (d) Triangular discretization of the geometry as depicted in (b), as used by the FEM solver.

correlation signal for the given spectrum of the pulse. For this work this technique is adapted for the IAC [67]. The adapted algorithm first extracts the AC core and then performs an iterative optimization of the spectral phase, to achieve the best possible agreement with the calculated AC signal. This technique allows for identification of temporal substructures, however, the time-direction itself cannot be determined. The iterative phase reconstruction allows for verification of the pulse shape assumption and for optimization of the spectral phase [67, 68].

3.2 Numerical method: Finite Element Method

This section presents the main numerical method employed to calculate the dispersion and loss in a fiber. For simple structures such as one layer step index fibers and hollow capillaries [71] the propagation parameters can be calculated directly in an analytic

fashion. More complex fiber designs require a numerical method to solve the propagating mode problem and to calculate the real and imaginary part of the effective refractive index. The structures discussed in this work lack strict spatial periodicity in the photonic cladding structure, c.f. Fig. 3.2 (a). Analytical calculations of guiding properties of photonic structures rely on a calculation of a photonic band structure for modes in a unit cell of the photonic crystal, these approaches are not applicable for the fibers discussed in this work. The only way to determine the guiding properties of a complex non-periodic structure is to solve the complete set of Maxwell equations.

The finite element method (FEM) is a mathematical technique developed to numerically solve a set of differential equations in a very effective way. Since most problems in modern physics can be formulated as such a set of differential equations this technique is commonly used. Applications of the FEM are found in heat conduction, fluid dynamics, solid state physics, and particle physics. Simulations in some of these areas play a key-role in industrial engineering and a precise simulation can save a lot of money, which explains the availability of many different software solutions utilizing the FEM method. Some products cover all simulation areas, and combine FEM with other mathematical methods to provide universal simulation tools, other software is specialized on one specific problem.

3.2.1 The mathematical concept

The FEM is used in this work as an effective tool to solve the propagation mode problem in a photonic crystal fiber, i.e., to calculate the field pattern of the propagating mode $\mathbf{E}_{\mathrm{pm}}(x, y)$ and to calculate the effective refractive index n_{eff}. The full propagating mode of the time harmonic Maxwell's equations is written as:

$$\mathbf{E} = \mathbf{E}_{\mathrm{pm}}(x, y)\, e^{\imath k_z z} \tag{3.9}$$

and

$$\mathbf{H} = \mathbf{H}_{\mathrm{pm}}(x, y)\, e^{\imath k_z z}. \tag{3.10}$$

The notation here is different from the one in Ch. 2 to enable a compact formulation as it is used in the theoretical literature on the FEM. In this notation the Maxwell's equations can be read as a generalized eigenvalue problem for the propagation constant k_z and $\mathbf{E}_{\mathrm{pm}}$:

$$A \begin{bmatrix} \mathbf{E}_{\perp} \\ \widetilde{E}_z \end{bmatrix} = k_z^2 B \begin{bmatrix} \mathbf{E}_{\perp} \\ \widetilde{E}_z \end{bmatrix} \tag{3.11}$$

with $\widetilde{E}_z = k_z E_z$ and A and B according to [72]. The matrices A and B contain all of the differential operators. This formulation as an eigenvalue problem suggests a way to solve the problem numerically with the finite element method [73]. A detailed description of the mathematical procedure can be found in [72]. Figure 3.2 illustrates the steps of a FEM calculation. Inspired by the micrograph of the structure (a) a geometrical abstraction is generated (b). During the triangulation, the computational domain Ω is discretized into small triangles as shown in (d). These triangles are called a

finite dimensional subspace of Ω and build the backbone of the calculation. For each of theses triangles a set of ansatz functions are defined. The approximate solution $\mathbf{E}_{\text{approx}}$ for the eigenvalue problem in Eq. 3.11 is given as a superposition of all these ansatz functions from all elements (triangles) of the subspace. The amplitude coefficients for each ansatz function on every element are unknown. To calculate these coefficients, only the boundary conditions of the computational domain Ω and between all of the elements are needed to be known. Despite the amount of data, this is a rather simple computational problem. To solve this computational problem, a large number of integrals needs to be solved numerically. Eventually one receives the amplitude coefficients for each element. This gives the solution $\mathbf{E}_{\text{approx}}$ and its propagation constant k_z as well as the complex effective refractive index n_{eff} (c.f. 2.2). The use of a finite element method to solve the propagating mode problem is beneficial, especially, for complex photonic structures [74, 75]. Virtually arbitrary structures can be calculated without simplifications or approximations. Important physical features of the electric field, such as discontinuities or singularities can be modeled very accurately and do not give rise to numerical problems.

The complicated cladding structure of a photonic fiber usually has many glass/air and air/glass surfaces, and a large number of discontinuities is expected. This is the reason why the FEM method was chosen for this work. As an additional mathematical feature of the FEM method, it converges with a fixed convergence rate towards the exact solution of Maxwell-type problems. An iterative refinement of the triangulation provides an easy check to see if numerical results are trustworthy [73]. For complicated geometrical structures the finite element method is faster and more accurate than the plane wave expansion method, whose ansatz functions (plane waves) are defined over the whole computational domain. In contrast, the FEM method uses localized ansatz functions. Using the plane wave expansion method a very large number of plane waves are necessary, in order to approximate a solution with discontinuities. This will result in a low convergence rate and large computational times [76].

3.2.2 The mode solver and the written code

For this work a commercial software package, namely JCMsuite [77], was used to solve the propagating mode problem. The software is optimize for scientific applications in optics. The software is developed at the Zuse Institute Berlin (ZIB) and is distributed by JCMwave [78]. All calculations presented were performed with a self-produced code written in Matlab.

The mode solver

The main advantage of the FEM implementation in JCMwave is the optimized computational effort compared to other mode solvers. To improve the accuracy and to reduce the computational time the software uses high-order edge elements, a-posteriori error control, and adaptive and goal-oriented mesh refinement [72, 76]. This allows for calculating the properties of a photonic fiber on a single computer. All calculations presented in this

work are computed on a single desktop computer with a Quad-Core processor. It is an intrinsic feature that an FEM calculation uses a rather large amount of random access memory (RAM). Since every finite element needs a certain amount of memory, more available memory results in more elements being evaluated and eventually in a more precise result. For a complex photonic structure as shown in Fig. 3.2 a total number of some 10^6 elements is sufficient, which requires a RAM memory of about 8-10 gigabyte. The actual amount of memory needed, also depends of the order of the elements and on the number of refinement steps. One mode-solving step for one wavelength is usually done in about half an hour.

Written code

The commercial software only provides a mode solver with a Matlab interface. To actually calculate the guiding properties of the fiber, the computational problem needs to be prepared for the solver, the mode solving needs to be repeated for all wavelengths of interest, and the calculated data must be post processed. The written code provides an exact description of the geometrical structure. The material is specified for every point in the computational domain Ω. In the produced code this description is realized by a series of iterative polygons Fig. 3.2 (b) shows a color coded representation of this description. The parameters defining the structure are:

- core diameter
- thickness of the first wall next to the core
- number of cells per cladding ring
- number of cladding rings
- chirp parameter (ratio of the diameter of the n-th and the $n+1$th ring)
- axes ratio, to control the elliptic cladding cells

In a next step, the triangulation sub-package is employed to calculate a proper triangulation of the structure as shown in Fig. 3.2 (d). The received triangulation is passed to the solver-package to solve the propagating mode problem for this structure. As described in Sec. 2.4.4 and Sec. 2.4.3, a photonic fiber usually features not only a single propagating mode, but a number of guided modes at the same wavelength, each with a different effective refractive index, c.f. Fig. 2.3 and Fig. 2.4. Additionally the FEM solver cannot distinguish between degenerated modes and returns them as two separate solutions. Figure 3.3 shows a selection of the calculated modes for a PCF at a single wavelength. The first step of the post-processing is to filter the fundamental mode in the core.

Figure 3.3 shows some modes calcultated at 760 nm. The real and imaginary part of the refractive index as well as the fraction of field intensity guided in the core (core fraction) is listed in Tab. 3.1. The modes guided in the core are identified by the core

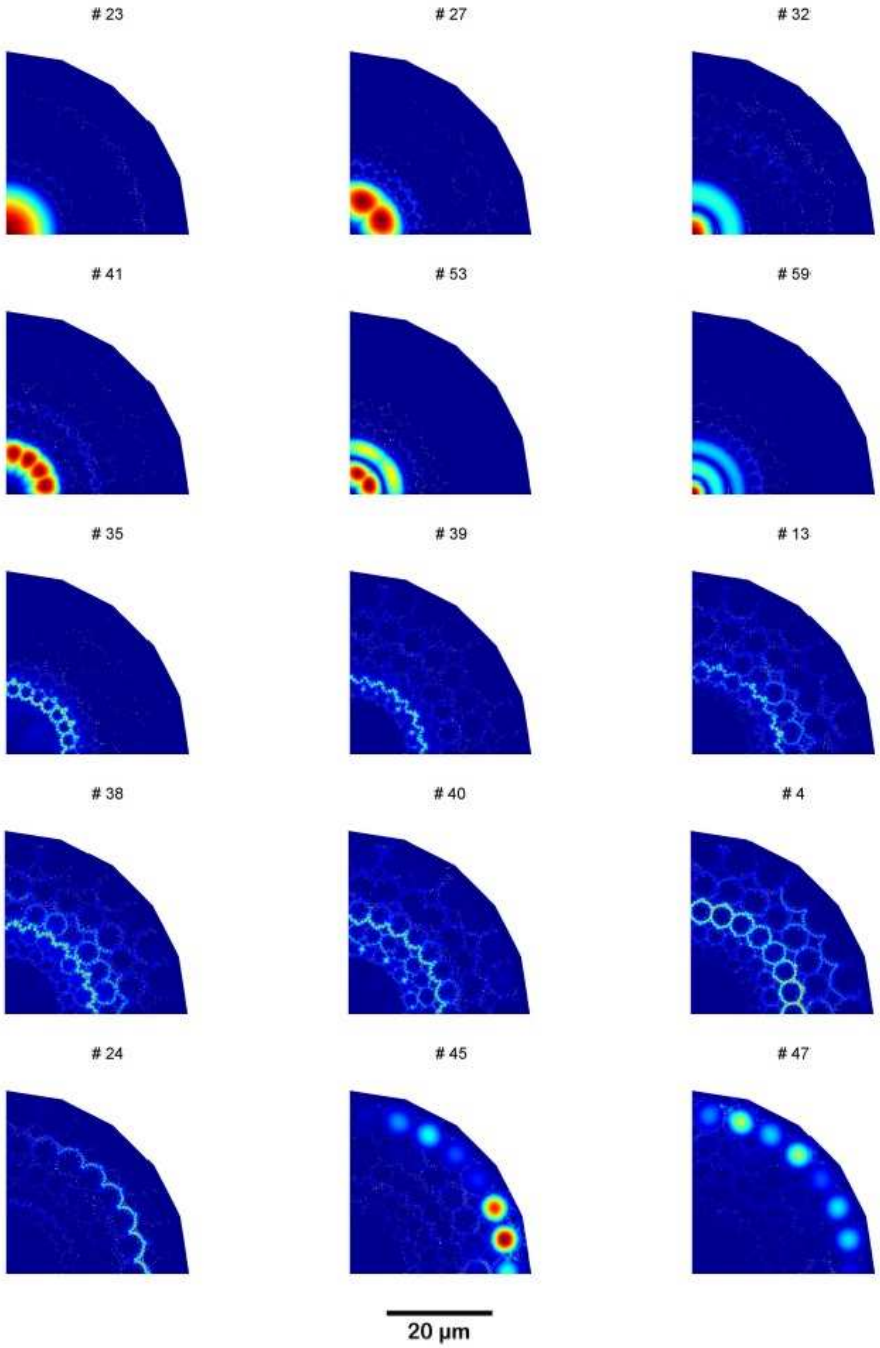

Figure 3.3: Selection of the calculated propagating modes in a PCF at 790 nm. The solutions are taken from a set of 60 solutions for the eigenvalue problem ordered by the absolute real part of the corresponding refractive index.

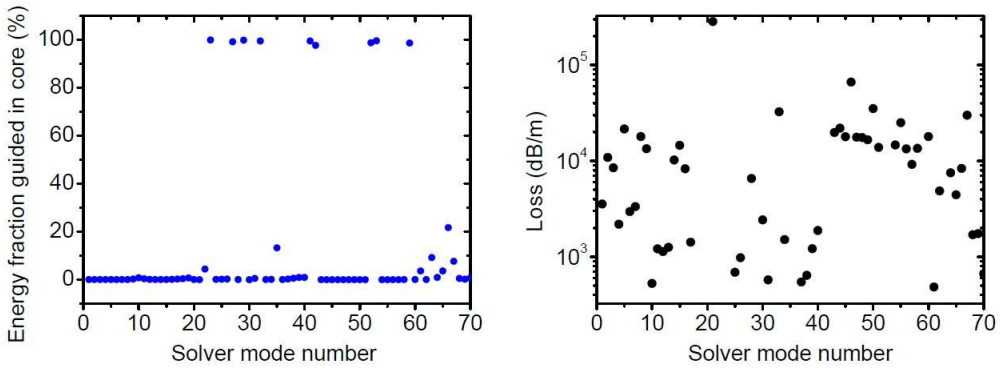

Figure 3.4: *Left:* Fraction of energy guided in the glass structure compared to the core in percent. This quantity allows for the identification of the modes guided in the core of the structure. *Right:* Losses of different propagating modes in dB/m. Because the data was taken after only one refinement step, the results are not accurate and the fundamental mode cannot be distinguished from the others.

fraction, Fig. 3.4 plots the core fraction as a function of the ordering number of the mode; the nine core modes can be identified by their core fraction values above 95 percent.

In a last step, the fundamental mode has to be identified from the selected core modes. Theoretically, the fundamental core mode can be found by comparing the losses (the fundamental mode has the lowest loss) or by a symmetry check. The symmetry check is more robust and can be applied at earlier stages of refinements, which reduces the computational costs. If the FEM method has not fully converged, the imaginary part of the refractive index is not very accurate and cannot be used to distinguish between the modes. Figure 3.4 shows the losses of the calculated modes after one refinement step, one of the core modes shows extraordinary low losses. For the symmetry check, the integrated intensity of different core segments is calculated and compared. The fundamental mode is the only mode where every ring segment at a distance r has less intensity than segment $r + \epsilon$ and simultaneously all $\Delta\phi$ segments have the same integrated intensity. When fundamental mode is found the FEM solver performs more refinement steps, with only this fundamental mode until the algorithm converges to its final accuracy. This way the computational effort is reduced to a minimum. By repeating this calculation for many wavelengths, β is calculated as a function of ω. The calculated $\beta(\omega)$ has to be precise enough and the wavelength steps have to be small enough so that the second derivative with respect to ω can be calculated with a sufficient signal to noise ratio [59]. Usually a step-width of 0.1-0.5 nm is sufficient in the vicinity of cladding resonances, the step-width needs to be reduced. To compensate for geometrical deviations from the ideal structure with the fiber length, the calculated β_2 is convoluted with a Gaussian [49, 50]. The loss of the fiber is calculated from the imaginary part of the effective index calculated for the fundamental mode, c.f. Eq. 2.26.

mode number	$\Re(n_{\text{eff}})$	$\Im(n_{\text{eff}})$	core fraction
4	1.0050	$1.3896\ 10^{-5}$	0.00032
13	1.0030	$7.9723\ 10^{-6}$	0.00059
23	0.9996	$8.3469\ 10^{-10}$	0.99898
24	0.9995	$1.6142\ 10^{-6}$	0.00094
27	0.9983	$1.0714\ 10^{-8}$	0.99165
32	0.9981	$1.9073\ 10^{-8}$	0.99455
35	0.9977	$2.9692\ 10^{-8}$	0.13227
38	0.9969	$4.0860\ 10^{-6}$	0.00589
39	0.9969	$7.7340\ 10^{-6}$	0.00926
40	0.9964	$1.1976\ 10^{-5}$	0.00921
41	0.9963	$6.5961\ 10^{-9}$	0.99507
45	0.9957	$1.1333\ 10^{-4}$	0.00009
47	0.9957	$1.2233\ 10^{-4}$	0.00006
53	0.9955	$3.9793\ 10^{-10}$	0.99575
59	0.9952	$7.2285\ 10^{-9}$	0.98595

Table 3.1: Properties of propagating mode solutions in a CPCF calculated at 790 nm with the FEM solver of JCMwave. The calculation was performed with one adaptive refinement step.

4 Dispersion management in a photonic crystal fiber

This chapter introduces the concept for a new class of photonic crystal fibers. The idea is to slightly change the geometrical dimensions of the microstructured cladding in radial direction to change the dispersion properties. The term chirped photonic crystal fiber (CPCF) is used to describe such a hollow core photonic fiber with a microstructured cladding where the geometrical cladding parameters are changing in radial direction. In the first part of this chapter, the guiding properties are investigated and explained by means of numerical simulations. The second part presents experiments which demonstrate the enhanced capabilities of this dispersion optimized CPCF for ultrashort pulse delivery.

4.1 Introduction

In the past decade, photonic crystal fibers have revolutionized the field of lightwave technology, enabling control of the linear and nonlinear optical properties of fibers to an extent impossible with conventional fibers [9, 34, 36, 80–83]. A particularly interesting class of such fibers are hollow-core fibers (HCFs, [84]). In these fibers, the light is effectively confined to an air-filled core surrounded by a regular periodic photonic cladding. Depending on the photonic crystal properties of the cladding, the guiding mechanism is either photonic bandgap guiding, c.f. Sec. 2.4.3, or quasi guiding, c.f. Sec. 2.4.4. Given the high index contrast between air and glass, a guiding bandwidth of up to 100 nm is obtainable with losses well below 1 dB/m [47, 85]. It has been discovered that interactions of the core mode with interface modes guided in the first material ring are detrimental to the transmission of the fiber and therefore must be avoided to attain such excellent transmission properties [47, 86–88].

As there is only little overlap of the guided mode with the surrounding glass structure, the hollow-core concept enables very small nonlinearities, which makes these fibers highly interesting for guiding ultrashort pulses, i.e., less than 100 fs duration. Such pulses would otherwise immediately suffer from excessive nonlinear optical effects in a glass core. So far, improvements of HCFs have mainly targeted the losses of such structures. However, one disadvantageous aspect of nearly all HCF concepts discussed to date are their dispersion properties. As material dispersion is nearly negligible in these structures, the dispersion is dominated by the strong third-order dispersion of the resonant waveguide structure [85, 89]. In fact, while the second-order dispersion of these fibers is vanishing for one particular zero dispersion wavelength in their transmission band, their third-order waveguide dispersion is only about one order of magnitude weaker than that of

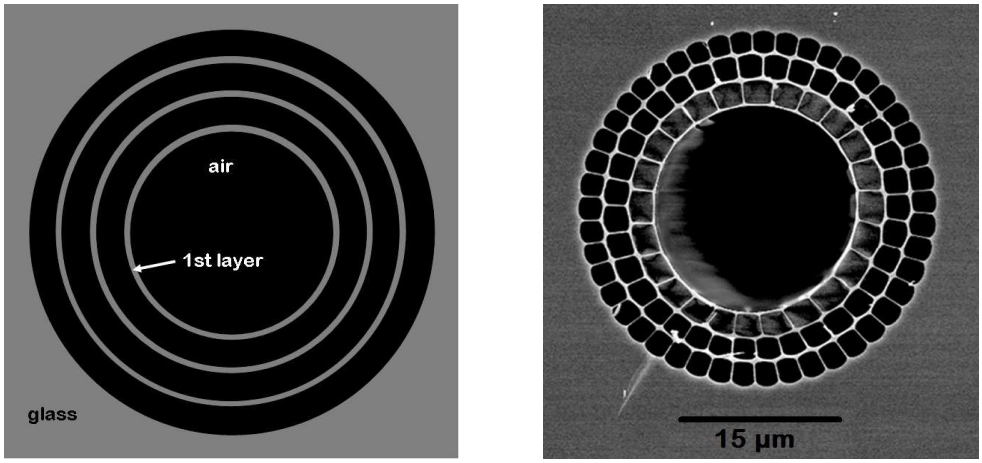

Figure 4.1: *Left*: Concept of an equidistant air/glass Bragg-fiber, which is used as a model system to explain the dispersion properties of chirped photonic crystal fibers. The number of layers, and the effect of their spacing and their thickness is investigated. *Right:* A realization of such an air/glass Bragg fiber with nano-support bridges between the glass rings [79].

bulk glass. While third-order dispersion is of little concern for the guiding of picosecond pulses, pulses of 100 fs duration or less experience strong temporal broadening in such fibers, devaluing the usefulness of the hollow core concept. Recently, several suggestions were made to overcome this inherent weakness of the HCF. Couny et al. have proposed guiding in a photonic crystal fiber that has no photonic band gaps [48]. Their fiber consists of a periodic Kagome structure and exhibits very wide quasi-guiding bands with little dispersion ($\beta_2 \approx 22000$ fs^2/m and $\beta_3 \approx 10^4$ fs^3/m at 800 nm wavelength). In terms of dispersion, the performance of the Kagome structure is surpassed by the CPCF presented here. Both approaches do not employ a photonic band gap for guiding. Quite clearly, also, both new concepts trade the low losses possible with conventional HCFs for improved dispersion characteristics.

In the following section, a detailed theoretical analysis of the guiding properties of chirped photonic crystal fibers, as used in Ref. [50] is presented and the potential of modified geometries for further improvement of such structures is analyzed. The analysis starts with an investigation of the dispersion properties in a perfectly symmetrical structure consisting of several free standing glass rings. Figure 4.1 (left side) shows such a structure used in the theoretical model, while the right side shows a real fiber following this concept realized by Vienne et al. [79]. In a first step, more and more rings are added while the dispersion and losses are monitored, then the thickness and the spacing of the cladding rings are modified in order to reveal the basic mechanisms influencing the guiding properties and to identify key-parameters for future fiber designs. The findings of this hypothetic structure are then applied to a more realistic adaption of the real fiber designs and an FEM method is employed to accurately calculate the guiding properties

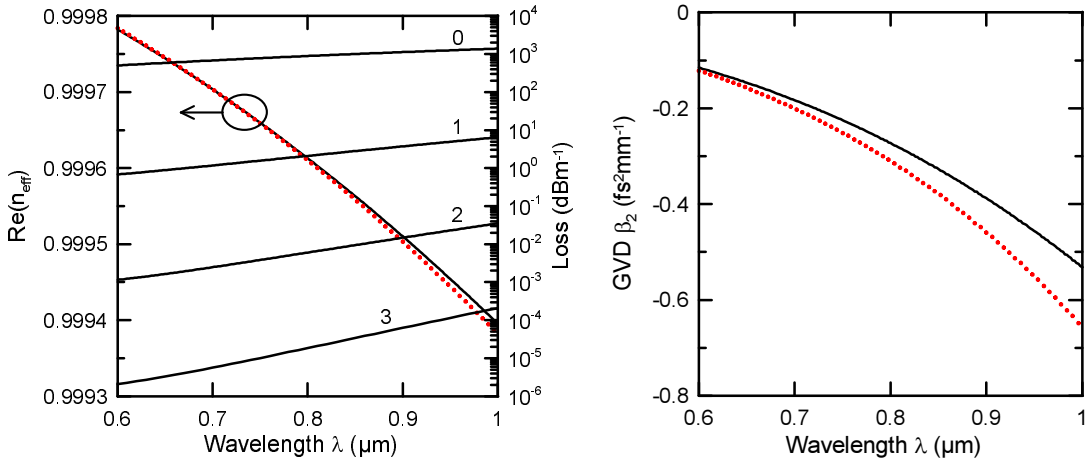

Figure 4.2: *Left:* The real part of $n_{\text{eff}}(\lambda)$ for the capillary (black line) and for a 1-ring structure ($d_1 = 157\,\text{nm}$, red line) with a 11 μm core diameter and wavelength dependent loss for the capillary (0), and for 1, 2, and 3 rings of 157 nm thicknesses at a spacing of 7.19 μm obtained from the radial transfer matrix method. The numbers next to the loss lines indicate the number of cladding rings. *Right:* The GVD of the capillary (red line) and of the single ring structure (black line). The GVD curves for the second and third ring added cannot be distinguished from the single-ring structure.

of a CPCF.

4.2 Analysis of the guiding properties of a chirped Bragg fiber

For a deeper analysis of the guiding properties of chirped fiber structures, first the theoretical model is reduced to a much simpler system, that can be analytically understood. This system is a set of free-standing glass rings building a radially symmetric Bragg fiber as sketched in Fig. 4.1. In a second step the effect of a geometrical chirp on the optical properties in this simple hollow-core waveguide geometry is investigated.

Many variants of fibers similar to the free standing Bragg fiber, mainly employing dielectric layers rather than glass and air interfaces, have already been theoretically explored and the mathematical are ready-to-use [90–93]. This is exploited in the following to give a basis for describing the CPCF. Because the waveguide modes are obtainable from the solution of a transcendental equation, accurate results are readily available. The radial transfer matrix method [90, 94], extended to the treatment of leaky modes [93, 95], is used to obtain the dispersion relation $\beta(\omega)$ with the complex propagation constant β and the effective index n_{eff} of the modes HE_{mn}, EH_{mn}, TE_{0n}, or TM_{0n}. Here m and n are the azimuthal and radial mode indices, respectively. The cylindrically symmetrical arrangement of alternating refractive index between the values 1 (air) to 1.51 (soft glass) is subsequently investigated. Focusing only on the principles of hollow-core guid-

ance in such ring structures and disregarding the effects from the support bridges in a real structure. This allows for simple but accurate estimation of the guiding properties in a chirped fiber structure.

The gedanken experiment starts with a single capillary, i. e. an infinitely long circular air hole of radius ρ inside a glass block. The core resonance condition for the HE_{11} mode is approximately given by [90, 96]

$$(k_0^{\perp})\rho = j_{01} \approx 2.4048\,, \tag{4.1}$$

with $k_0^{\perp}$ the radial wavenumber of the propagating mode and j_{01} the first zero of the Bessel function J_0. The radial wavenumber $k_i^{\perp}$ in the ith layer is given by $k_i^{\perp} = ((\omega/c)^2 n_i^2 - \beta^2)^{\frac{1}{2}}$, with the refractive index n_i of layer i. The propagation loss of the waveguide is determined by the imaginary part of β (c.f. Eq. 3.6), c.f. Sec. 2.2. The loss of the HE_{11} mode in the discussed capillary is given in a very good approximation [97] by the equation:

$$\alpha = \Im(\beta) = \left(\frac{j_{01}c}{\omega}\right)^2 \rho^{-3} \left(\frac{\frac{1}{2}(n_1^2+1)}{\sqrt{n_1^2-1}}\right)\,, \tag{4.2}$$

For a wavelength of 800 nm and a capillary with 11 μm core radius, the resulting loss is more than 500 dB m^{-1}. Figure 4.2 depicts the dispersion in terms of GVD and n_{eff} as well as the loss of the structure for different numbers of layers. All curves are calculated from the exact dispersion relation. The loss of the capillary discussed above is referred to as zero-layer cladding. The obvious conclusion of Fig. 4.2 is that in large hollow core fibers the group velocity dispersion is small compared to solid-core fibers; at the cost of transmissivity. One straight-forward means of reducing the radiation losses is to increase the number of alternating low- and high-index layers with individual thickness d_i around this central core [90]. If a particular high- or low-index layer is in antiresonance, the radiation losses appear strongly reduced due to radial Bragg reflection [90].

One has to distinguish between layers of resonant and antiresonant thickness. In case of $(k_i^{\perp})r >\approx 6$, where the zeros of the Bessel function $J_0(x)$ are approximately spaced by π and for $m = 1$, antiresonance means [90, 96]

$$(k_i^{\perp})d_i = (2l+1)\frac{\pi}{2}\,, \tag{4.3}$$

whereas resonance refers to

$$(k_i^{\perp})d_i = (2l+2)\frac{\pi}{2} \tag{4.4}$$

with l being a non-negative integer. The case with $l = 0$ is named the first anti-resonance. Vectorial effects of the hybrid HE_{mn} and EH_{mn} modes at the interfaces, however, lead to deviations from this ideal behavior obtained for pure TE_{0n} or TM_{0n} modes [90].

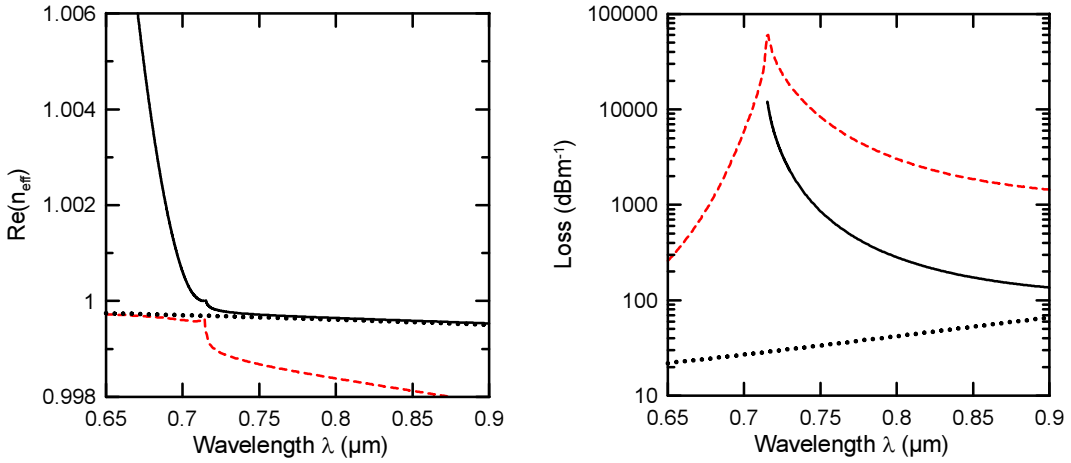

Figure 4.3: Wavelength dependence of the real part of the effective index (left) and of the losses (right) for the guided HE_{11} mode in a glass capillary with inner diameter 11 μm and ring thickness $d_1 = 157$ nm (solid black lines) and $d_1 = 314$ nm (dashed black and red lines). In the latter case, two branches of the dispersion relation coexist, which are indicated in black and red.

4.2.1 Layers of antiresonant thickness

In a first calculation the ring thickness is adjusted according to the antiresonance condition at a free space wavelength $\lambda = 700$ nm. The effective index of the system with different numbers of layers is calculated and shown in Fig. 4.2 with the number of the anti-resonant layer printed next to the respective line. Obviously, the introduction of a second layer noticeably changes the dispersion curve. Still, at the design wavelength (here 700 nm), the real parts of the two computed refractive indices cross because the core is at resonance while the first ring is simultaneously at anti-resonance, i.e., Eqs. 4.1 and 4.3 are fulfilled at the same time for this wavelength. This condition cannot be achieved for all other wavelengths, and, as a result, the second interface pushes the real part of the modal index into its own antiresonance, leading to deviations from the capillary (zero layers) dispersion. Adding additional alternating glass-air layers of the appropriate antiresonant thickness does not produce any further noticeable changes in the real part of the effective index. The loss, on the other hand, is monotonically reduced by adding more layers of the same antiresonance thickness, as can be seen in Fig. 4.2. From this calculation follows that in the case of an ideal antiresonant Bragg fiber, the dispersion is determined by the diameter and thickness of the first layer, while the losses can be reduced by additional antiresonant layers.

4.2.2 Layers of resonant thickness

Going back to the case of one glass ring in air, if the thickness of this layer is detuned from the antiresonance, there will be a new wavelength where Eqs. 4.1 and 4.3 are

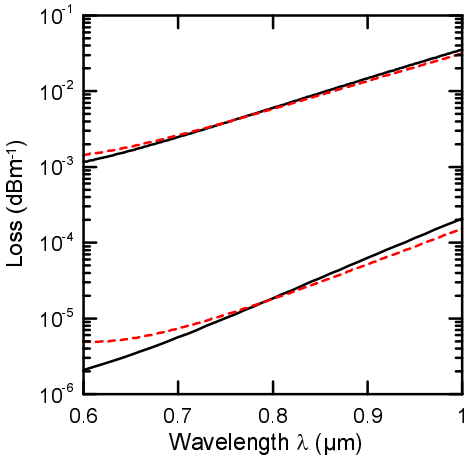

Figure 4.4: Wavelength dependent losses for the unchirped Bragg fiber (black curves) and for the chirped Bragg fiber (red curves) for 2 glass rings (larger loss, top curves) and for three rings (lower loss, bottom curves).

simultaneously fulfilled, leading to a different crossing point of the two dispersion curves. Moreover, at this point the largest reflectivity enhancement will occur. One should keep in mind that the loss of the capillary grows quadratically with the wavelength (see Eq. 4.2), i. e., shifting the antiresonance wavelength to a larger wavelength does not always lead to a smaller total loss than at the original antiresonant wavelength.

The most prominent change of the dispersion curve for a single glass ring occurs if one increases the ring thickness to meet the resonance condition Eq. 4.3 instead. This ring then acts as a waveguide core by itself, and a new ring-shaped mode with larger losses for $n_{\text{eff}} < 1$ appears. In the region where the core and the ring mode are simultaneously resonant, these two modes interact and give two separated branches of the dispersion relation, as is shown in Fig. 4.3. Also, around this wavelength (700 nm) the loss is dramatically increased for those parts of the branches that asymptotically converge toward the original, antiresonant ring. However, because the mode in the high-index ring is (in addition) index guided, the loss vanishes for $n_{\text{eff}} > 1$. The general behavior of the dispersion relation of the glass ring widely resembles anticrossing of modes in different types of photonic bandgap fibers, e.g., the anticrossing of the core and surface mode in hollow core fibers, and the one between core and leaky mode in a solid-core photonic bandgap fiber [98]. Due to the azimuthal symmetry such coupling only occurs between modes of the same azimuthal quantum number.

Layers of different thickness

In the following, the influence of a systematic detuning of more reflection layers in order to enlarge the wavelength region of low losses is investigated. Further it is compared to the “single”-cell approach of many layers designed for antiresonance at the same wavelength. Depending on the spectral region of interest, one could design a chirped

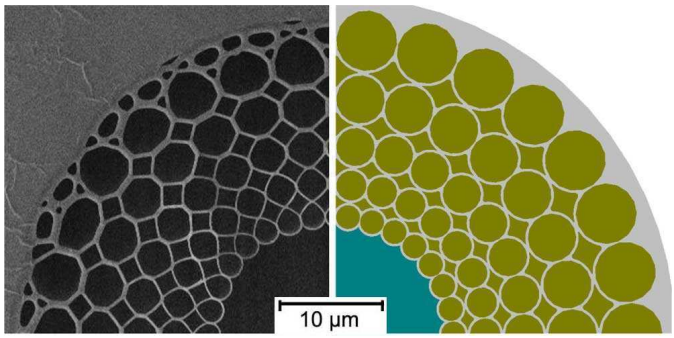

Figure 4.5: Structure of a chirped photonic crystal fiber. *Left:* Scanning electron micrograph of a manufactured fiber [50] (details in Sec. 4.5.1). *Right:* Schematics of the geometric model used in the FEM calculation. The light gray areas indicate glass around the hollow core. Hollow regions of the cladding are marked in green. The geometrical objects are defined in a polygonal format.

structure where the first layer is antiresonant at a certain wavelength, the second one at a second (larger) wavelength, and the third one for yet another larger wavelength. Similar chirping has been employed in different photonic structures such as waveguides [99] and mirrors [100, 101]. The use of chirping in Bragg fibers with a solid core was also investigated [102]. None of the previous approaches pursued had the purpose to spectrally distribute detrimental dispersive resonances and neither of these effects appears to play a role in hollow-core photonic crystal fibers. This argument can be understood by comparing the original unchirped Bragg fiber (Fig. 4.2) with two glass rings and three glass rings to a chirped Bragg fiber, where the first ring is unchanged (antiresonant at 700 nm), the second glass ring is antiresonant at 800 nm, i.e., $d = 176$ nm, and the third one in the three ring-structure is antiresonant at 900 nm, i.e., $d = 199$ nm. Because the real part of the effective refractive index is mainly given by the air core resonance condition, the air rings of constant thickness of 7.19 μm are automatically antiresonant, as one can see from Eqs. 4.3 and 4.4. The results are shown in Fig. 4.4. One clearly sees the intended behavior of decreasing the losses at 800 nm and 900 nm compared to the unchirped fiber, yet at the expense of increased losses for 700 nm. However, the absolute values of the loss at the longer wavelengths are still higher than for 700 nm due to the general trend of larger losses at longer wavelengths [see Eq. 4.2]. Additionally, given the large bandwidth of the antiresonances, the low-loss bandwidth is already relatively large in the unchirped structure. Therefore, the effect of a wavelength spacing of 100 nm for the chirping of the structure is not very pronounced. Obviously, design wavelengths of 700 nm, 1000 nm, and 1300 nm appear to be more useful because this would lead to a more substantial increase of the bandwidth.

4.3 Accurate calculation of a chirped fiber

For a more qualitative analysis of the CPCF fiber structure a finite element method is used, c.f. Sec. 3.2. The FEM provides a very efficient and accurate way to calculate the complex effective refractive index of a PCF. Figure 4.5 shows the used geometrical abstraction of the fabricated chirped fiber compared to a micrograph of a fiber sample. The computational costs were considerably reduced, taking advantage of the two orthogonal mirror symmetry planes ($x = 0$, $y = 0$) of the ideal structure. The effective refractive index was calculated in a 200 nm band covering the typical Ti:sapphire wavelength. Typically, such sequences exhibit many narrowband resonances as shown in Figs 4.6 (a)-(d). While the losses between the resonances are as low as 0.3 dB/m, this value increases to some 20 dB/m exactly on resonance. On resonance, the numerical simulations clearly identify localization of the mode field in the one ring of the structure.

Local dispersion properties and resonance modes

This mode resembles the occurrence of whispering-gallery modes in related geometries. Similar findings have also been discussed as surface modes in slightly different geometries [47, 87, 88]. To further support this assumption, the matrix method is employed to analytically calculate the dispersion relation of the fundamental mode of a ring with a radius of 11.0 μm and a thickness of 500 nm. With the quantum number $m = 59$, the mode pattern depicted in Fig. 4.6 (d) is calculated. It shows a strong similarity to the mode field pattern in Fig. 4.6 (b) with a node in radial direction in the ring center. The corresponding ring mode shows $2m$ field maxima on the circumference of the ring. In particular, the spacings between subsequent maxima of these modes are nearly identical in the FEM calculation and in the analytical model. Nevertheless, due to the azimuthal inhomogeneity of the real structure in Fig. 4.6 (b), there is strong coupling between the mode guided in the core and the ring mode. Additionally, the mode guided in the innermost ring of the glass structure shows leaking into the outer cladding regions. The described leaking is shown in the video-file [103] in Ref. [50]. In combination, these two mechanisms explain the spectral localization of losses with the appearance of resonances in the modes of the innermost ring of the fiber structure.

To further investigate this effect, the spectral spacing of the different modes of the first ring (which can couple resonantly) is calculated, i. e., with the same propagation constant (or equivalently with the same effective index) as the core mode. Due to the large core, the effective index of the CPCF does not change significantly with the wavelength. Therefore a constant effective index of $n_{\text{eff}} = 0.9997$ is used to obtain the wavelength of ring modes of different azimuthal quantum number and different number of nodes in radial direction. The same analytical method as in Sec. 4.2 is used. For the first-order ring mode, a wavelength spacing of 6 nm between $m = 100$ and $m = 101$ is obtained. There is another mode with $m = 95$ and $m = 96$ with a wavelength spacing of 5.7 nm at an offset of 1nm. Finally, a higher-order mode [see Fig. 4.6(d)] is found with $m = 59$ and $m = 60$ and one radial node in the ring center, with a wavelength spacing of the resonances of 4.7 nm at another offset. Consequently, for the CPCF one

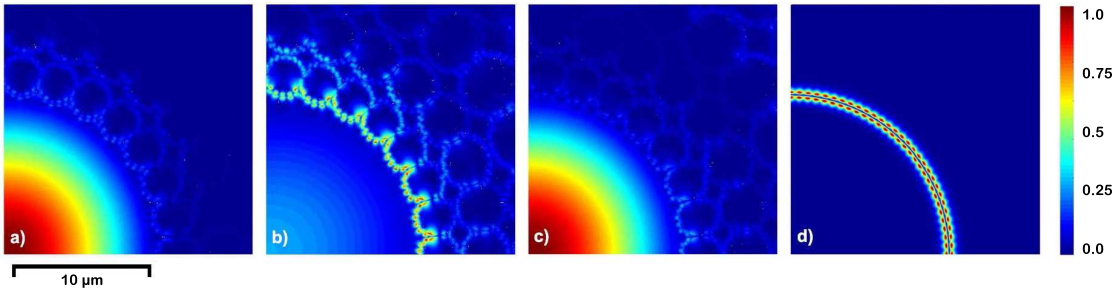

Figure 4.6: Mode fields in the vicinity of a resonance of the innermost glass layer (a) one wavelength step below resonance ($\lambda = 712.8\,\mathrm{nm}$), (b) at resonance ($\lambda = 713.4\,\mathrm{nm}$), (c) one step above resonance ($\lambda = 714\,\mathrm{nm}$). (d) Analytically computed mode pattern of the $m = 59$ mode of a dielectric ring structure ($n = 1.51$) with $11\,\mu\mathrm{m}$ core radius and 500 nm thickness. Color coding indicates the modulus of the electric field on a linear scale. In regions of very low losses, the field distributions are much more concentrated to the hollow core of the CPCF.

can expect a wavelength spacing of the strong resonances caused by modes of the first ring in the range of 1 nm to 6 nm. On the other hand, the coupling strength of the core mode to these ring modes strongly depends on the variation of the dielectric structure in azimuthal direction, in particular on the Fourier decomposition of these variations. Therefore, the different ring modes lead to different resonance strength. In the numerical simulations of the CPCF shown in Fig. 4.7 this simple model is confirmed by the exact numerical simulation of the real structure. Figure 4.7 shows the energy fraction guided in the core, which allows for the identification of the spectral position of the cladding resonances. The spectral spacing as well as the different resonance strength is confirmed to be compatible with the above findings.

Global dispersion properties

Regular HCFs are operated in the photonic bandgap of the periodic cladding. Hence, the only photonic states are localized states at defects (surface mode, core mode) [47, 86–88]. In contrast, in the non-periodic cladding many local defect modes exist, which is similar to photonic quasi-crystals [104]. These defects may also appear deeper in the cladding, which also leads to a much narrower wavelength spacing. However, these modes lead to smaller resonances than the modes of the first ring, which makes them of less importance for the total dispersion of the fiber. Figure 4.8 shows the prototypical behavior of the dispersion and the loss in the immediate vicinity of one mode of the innermost ring, further illustrating the major influence of these resonances on the propagation in CPCFs. Quite clearly, the occurrence of a transmission dip is accompanied by a characteristic strong peak of the imaginary part of the refractive index [cf. Fig. 4.8 (c)], which coincides with the appearance of a ring mode with index m. Crossing this resonance, the light guided in the core also switches modes, as is indicated by different colors for

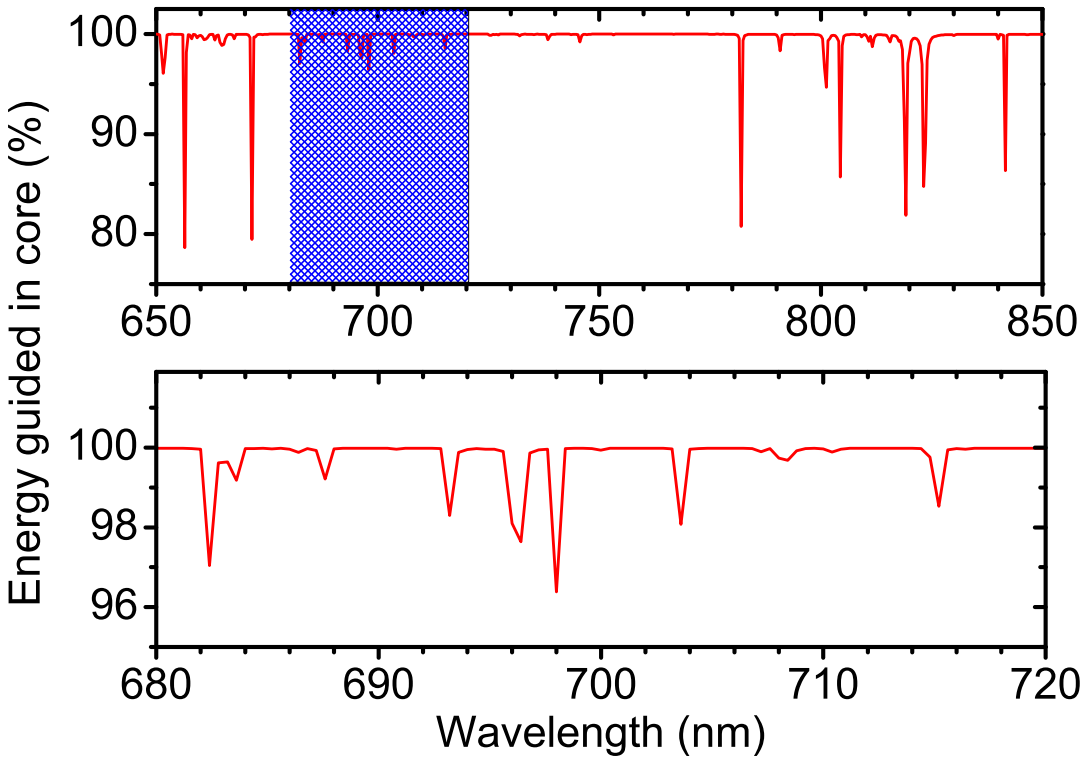

Figure 4.7: The energy fraction guided in the core calculated for a support thickness of $d = 400\,\text{nm}$. Several cladding resonances can be identified and their spectral spacing is found to be in the range between 1 and 6 nm is confirmed.

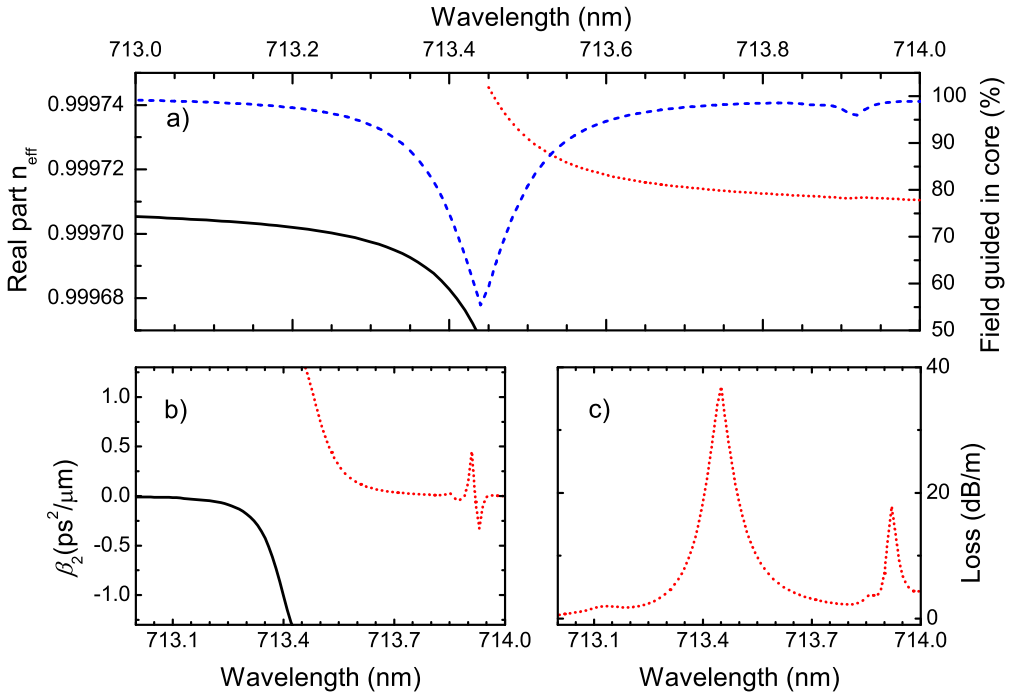

Figure 4.8: Characteristics of a narrowband resonance in a CPCF. (a) Real part of the refractive index (red and black line, left axis) and field content of the hollow core region (blue line, right axis). Red and black colors of the real part of the refractive index indicate the transition between different modes at resonance. (b) Second-order dispersion $\beta_2(\omega)$. (c) Losses of the fiber.

the real part of the effective index in Fig. 4.8 (a). Clearly, the transmission dip also manifests itself with light guided in the cladding, see Fig. 4.6 (b) and dotted line in Fig. 4.8 (a). Finally, Fig. 4.8 (b) illustrates the consequences of the sharp resonances on the resulting dispersion of the fiber, which may exhibit extremely large values $|\beta_2|$ in excess of $1000\,\mathrm{ps}^2/\mathrm{mm}$. It is noteworthy, that the smallest variations of fiber geometry will immediately lead to a shift of the resonances. Considering that the resonance width is well below a nanometer, a variation of the radius on the order of 1% will already lead to substantial changes, which translates into mechanical tolerances of a few nanometers for the fiber geometry, a precision that is certainly impossible to maintain in a fiber drawing process and which also explains why such sharp resonances could not be observed in experimental investigations of the fiber dispersion. Structural variations may occur, both due to small longitudinal variations of the fiber geometry during the drawing process as well as to deviations from a perfect 30-fold rotational symmetry. Experimental investigations [50] also indicate that both contributions appear to be of about equal importance. For a more realistic description of the propagation behavior in CPCFs and to account for geometrical variations of the fiber during the drawing process, therefore the procedure originally described in [50] is used to account for geometry variations. For this purpose, the simulation results are convolved with a Gaussian of 10 nm full width at half maximum, which has lead to a good agreement between numerical simulations and measured values [49, 105, 106]. Appearance of ring-mode resonances is the key effect for understanding the guiding process in CPCFs. As the order of these modes is quite high and because many rings actually contribute to the resonances, there is in fact a large number of such sharp resonances distributed over the entire transmission wavelength range of such a fiber. However, as the CPCF structure does not employ identical cells, the resonances cannot compound, and realistic structure size variations further serve to smear out the resonances, lessening any detrimental effect that may arise from them at the expense of an increased overall loss background. The wavelength-dependent losses and also the dispersion must therefore be understood as being governed by the spectral density of the ring-mode resonances rather than stemming from the spectral dependence of one localized mode. While CPCF designs can easily be adapted to avoid the occurrence of a particular resonance at any given wavelength, one ultimately seeks for designs that avoid the occurrence of such resonances over as wide a wavelength range as possible. In the following section, it is discussed whether and how global design parameters, such as the chirp or duty cycle of the structure, can be used to modify the guiding properties of the fiber designs.

4.4 Geometry dependence of the guiding properties

For further understanding of the guiding process a series of numerical simulations, in which two primary parameters of the geometric structure were varied, are performed. In the first series of simulations, the air fill factor of the structure is changed, i.e., the wall thickness d of the glass tubes is varied, c.f. Fig. 4.9. In the second series, the cell ellipticity, i.e., the ratio of radial and azimuthal axes of the unit cells is varied, Fig. 4.10.

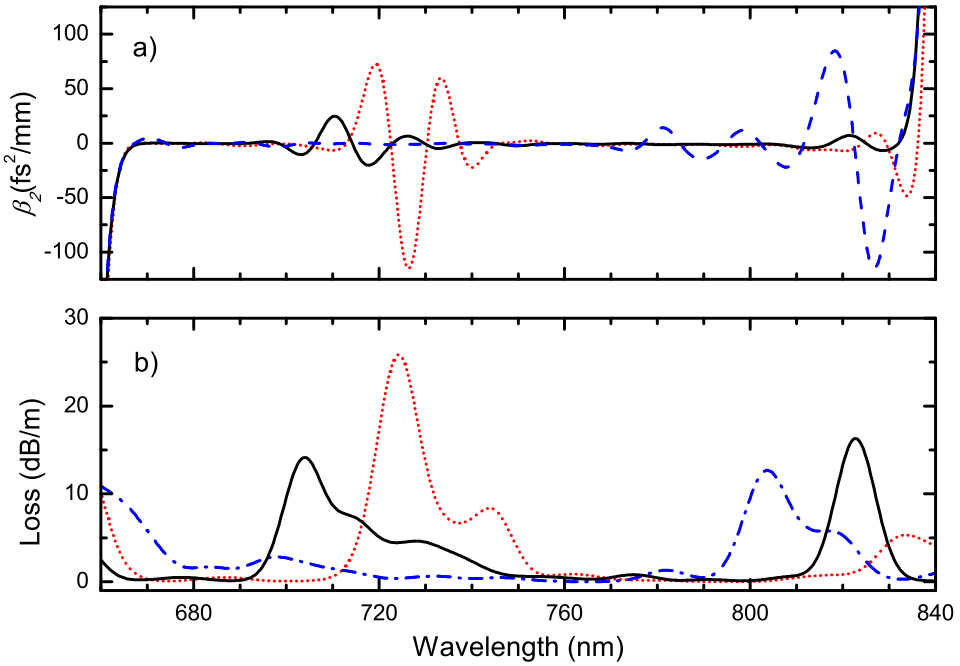

Figure 4.9: Numerical calculation of (a) $\beta_2(\omega)$ and (b) the loss of different CPCFs with varying wall thickness d in the design. red: $d = 300\,\text{nm}$, blue: $d = 400\,\text{nm}$, black: $d = 500\,\text{nm}$.

These simulations are carried out over a 200 nm bandwidth with a 0.4 nm step size and have been convolved with a 10 nm Gaussian, as discussed above.

Figure 4.9 (a) shows the resulting dispersion profiles with maximum excursion that have now been appreciably reduced to the range from -100 to $+100\,\text{fs}^2/\text{mm}$, which must be compared to the ps^2/mm scale employed in Fig. 4.8 (b). The largest excursions appear exactly at the locations of transmission dips and often exhibit a characteristic dependence resembling the sinc function, which has also been observed in experimental investigations [50]. These examples further confirm that not only the circumference of the first glass ring influences the position of the resonances but also the width of this structure. Nevertheless, the spacing of about 120 nm between these transmission dips remains remarkably unchanged, furtherer highlighting the importance of modes propagating inside the innermost ring. For the central 60 nm range in between the dissipative resonances, typical losses of 0.28 ± 0.2 dB/m are observed together with dispersion values $\beta_2 = -1.5 \pm 0.8\,\text{fs}^2/\text{mm}$. These values as well as the strength of the resonances show little systematic variation with the parameter d (ring thickness), underlining the robustness of the CPCF concept against manufacturing variations.

In a second series of numerical simulations the ellipticity of the unit cells is varied, see Fig. 4.10. To characterize the ellipticity, the ratio of azimuthal and radial axis of the unit cells of the cylindrical lattice, d_a and d_r, respectively, is used. The geometry parameter is defined as $\chi = d_a/d_r$. Values $0 < \chi < 1$ are defined with the major unit cell axis being

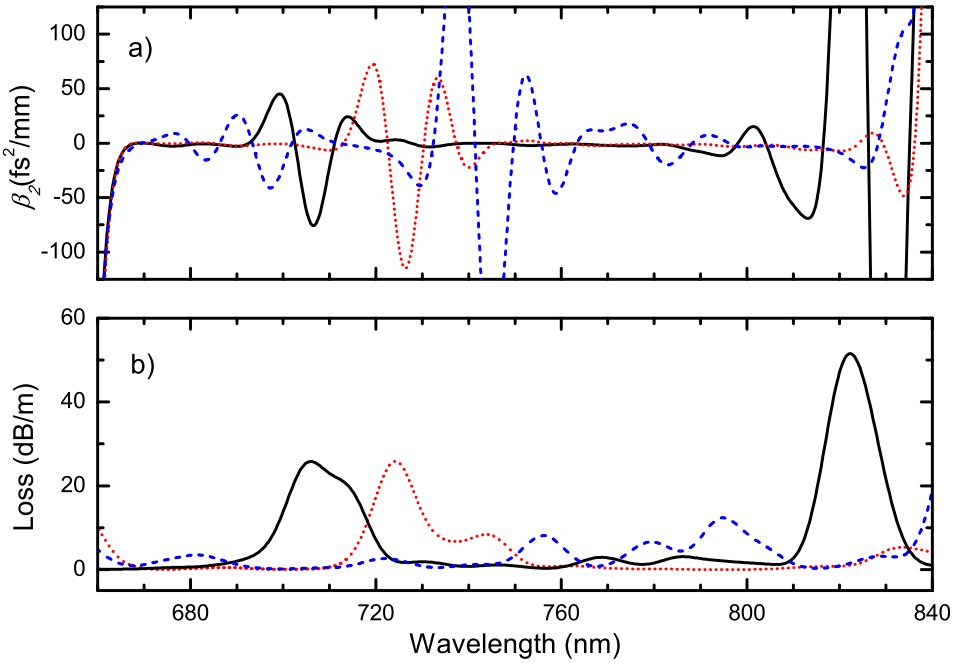

Figure 4.10: Calculation of $\beta_2(\omega)$ (a) and loss (b) of a CPCF in dependence of the ratio of azimuthal and radial axis of the unit cells χ. blue: $\chi = 0.8$, black: $\chi = 1.2$, red:$\chi = 1.9$.

the radial axis d_r; $\chi > 1$ indicates tangential orientation of the major axis of the unit cell. These simulations indicate a similar behavior as in Fig. 4.9 (a), with characteristically shaped dispersive resonances spaced at about 120 nm. Yet one noticeable trend in these simulations is the growing roughness of the dispersion in between the resonances for decreasing χ. In the case of lowest χ, it is difficult to differentiate between resonances and transmission bands as the dispersion generally shows many excursions; the transmission is generally quite low and lacks characteristic dips unlike all other cases discussed before.

Nevertheless, these exemplary structure variations further confirm that the global spectral behavior of the transmission properties is mainly ruled by the occurrence of resonances of modes localized in the innermost glass ring of the structure. Even quite massive structure variations appear to have remarkably little influence on the spacing of the resonances, on the loss and dispersion in between them, and on the characteristic shape of the dispersion on resonance. Therefore the CPCF concept appears rather robust in terms of manufacturing errors. In fact, small variations of the ring thickness of the fiber geometry during the drawing process appear to be of major importance for ensuring the smooth dispersion properties of these designs. However, lateral stress resulting in strong ellipticity must be prevented because this is severely influencing the dispersion properties of the fiber.

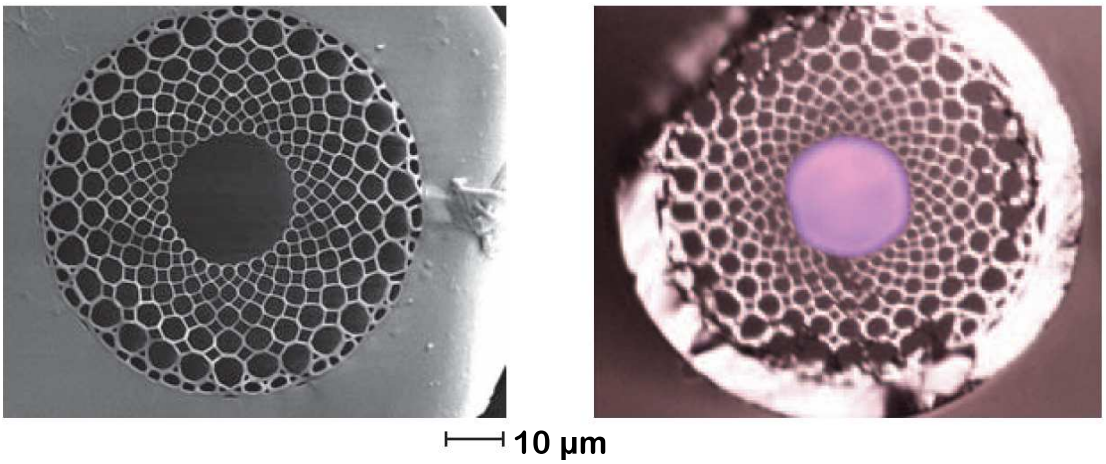

Figure 4.11: *Left:* Scanning electron micrograph of the fabricated fiber. *Right:* Optical micrograph of same the fiber. In addition to an illumination of the front facet, white light was also coupled into the fiber, which guides visible light at 720 nm and in the blue spectral region.

4.5 Fiber samples and measured optical properties

The previous section discussed the expected guiding properties of a chirped photonic crystal fiber. The fabrication of the suggested chirped "free-standing-ring" structure is virtually impossible, although Ref. [79] does report progress for a similar structure without a chirp. In practical terms, the introduction of a chirp in the photonic cladding tends to result in unstable, difficult to draw, fiber layouts. However, the concept of building preforms by using capillaries of different diameter was successful. The suggested layout in Sec. 4.4 anticipates this issue and the numerical model was chosen based on the fiber that was eventually drawn. Figure 4.11 shows micrographs of the drawn structure, fabricated by Julia Skibina (Saratov State University) at facilities of Nanostructured Glass Technology Comp. in Saratov, Russia.

4.5.1 Fiber fabrication

The fiber is produced using the stack and draw technology [9, 42, 43], which has become a standard technique to produce PCFs with solid as well as with hollow cores. Figure 4.12 illustrates the fabrication process in a schematic diagram and shows pictures of the preform preparation process and of the CPCF drawing. In a first step, several capillaries are produced and stacked together to build the raw preform. This raw preform [Fig.4.12 (a)] already resembles the desired geometrical layout of the final drawn fiber, however its diameter is still in the 10 cm range. In the case of the CPCF, the raw preform is built from capillaries with different diameter. The preform is then heated for the first time [Fig.4.12 (b)] and the diameter is reduced and fused into another glass tube that will become the solid glass cladding. This microstructured preform, or cane, is then fed into

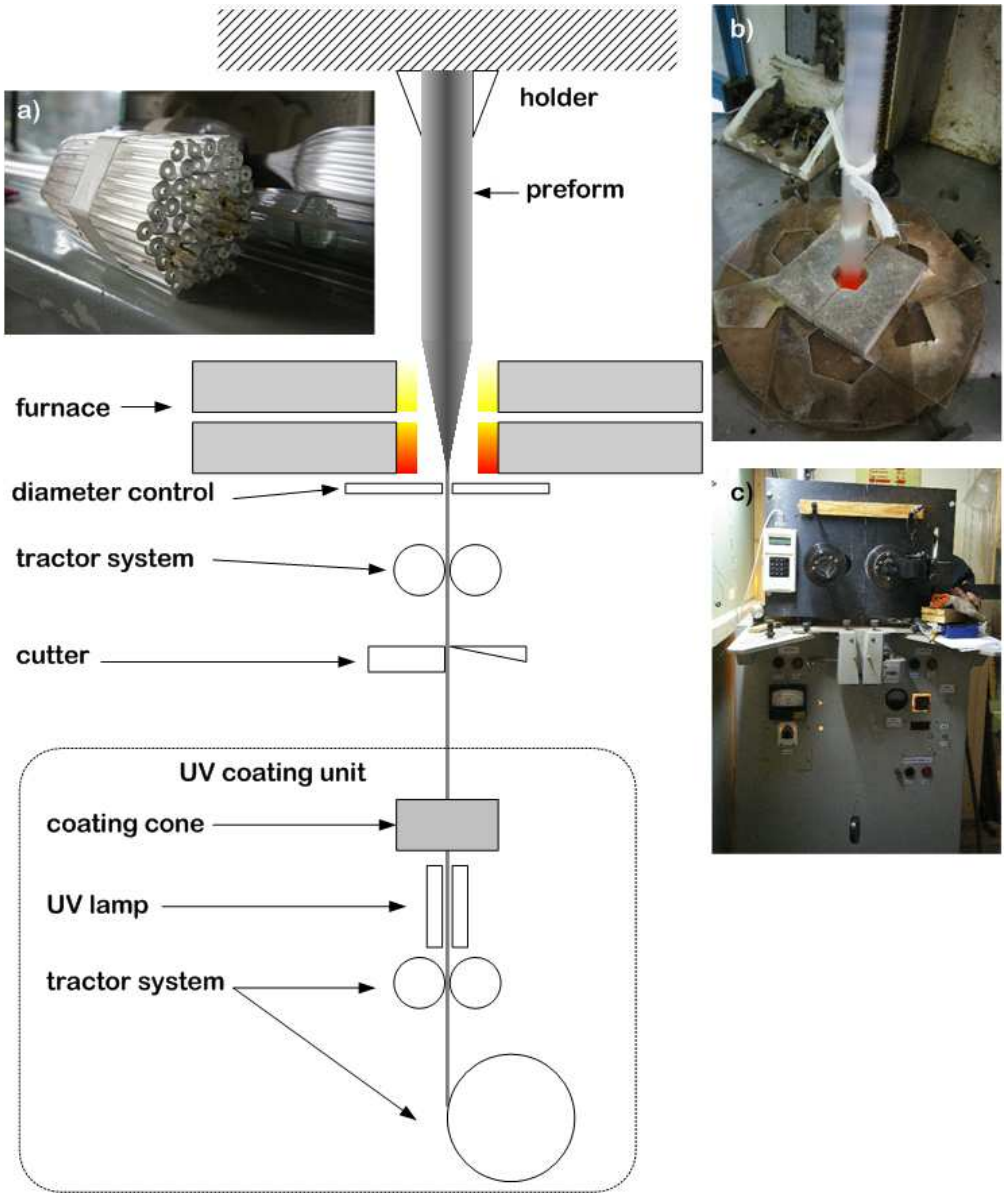

Figure 4.12: Schematic diagram of the fiber fabrication process. (The assembly of the preform is not shown.) (a) A photograph of a PCF preform as used in the drawing process. (b) The preform fed into the furnace. (c) The diameter control and cutting unit.

the furnace and drawn into the fiber. The drawing usually takes place in a drawing tower and the hot fiber is drawn vertically. During the drawing process the fiber diameter is reduced to its final size. Depending on the drawing technique, the fiber diameter could be reduced stepwise. The fiber diameter and the drawing speed as well as other parameters are continuously monitored [Fig.4.12 (c)]. Important parameters are: e.g., the drawing speed, the pressure applied inside the hollow bores to prevent collapsing, the heat of the furnace, and the fiber temperature. After reaching the intended diameter and structure, most commercial fibers are fed into a UV coating unit to receive a polymer cladding to protect the fiber and to make it more robust. Given the technical situation in the Saratov facility, the coating step must be skipped and the fiber samples are produced without a polymer coating, resulting in rather fragile fibers.

To create a CPCF, the fiber preform is assembled from five circular layers of glass tubes of varying diameters, each layer consisting of 30 identical cells. The ratio of inner to outer diameter of each individual tube is 0.85. The entire fiber structure is made from the glass C89-1, which is a soft optical glass composed of 72% silica, 16% Na_2O and smaller amounts of CaO, MgO and BaO. This glass is nearly identical to Schott crown glass K7 [21]. It has the same average refractive index for visible wavelength of $n = 1.519$ and also a very similar material dispersion indicated by the Abbe number

$$V = \frac{n(587.6\,\mathrm{nm}) - 1}{n(486.1\,\mathrm{nm}) - n(656.3\,\mathrm{nm})} = 60. \tag{4.5}$$

This glass is chosen for its excellent thermo-elastic properties and its suitability for the fiber drawing process. Using soft-glass technology, fiber lengths up to 1 km can be manufactured at the Saratov facility. The micrographs in Fig. 4.11 shows a fiber that is drawn to a core diameter of 22 μm. Additionally a second fiber is manufactured with a diameter of 53 μm. In the case of the 22-μm-core fiber, a wall thickness of the innermost ring of a little less than 500 nm is measured.

The fiber geometry received after the drawing process and used for the experiments in Sec. 4.6.1 and Sec. 4.6.2 consists of a hollow core surrounded by a chirped five-layer photonic cladding, with each layer comprising 30 identical cylindrical cells. The geometric average of the cell radius versus layer number varied linearly from 1.35 μm to an outermost value of 2.6 μm. In addition to the central bores of the cylindrical cells, interstitial holes with a diamond-like shape appear. Although there is apparently strong stress to the individual cell during the drawing process, this does not cause a major distortion of the global circular symmetry of the fiber. In fact, as careful analysis of Fig. 4.11 reveals, deviations of the fiber structure from circularity amount to only 2% of the radius, that is, 250 nm (r.m.s.). The optical micrograph in Fig. 4.11 (right side) reveals a clean HE11 mode profile, with white light being coupled into the far fiber end face. It is also indicative of two strong transmission bands in the blue and red spectral range. Based on measures taken from the micrograph shown in Fig. 4.11 (left side) the FEM model of Sec. 4.4 has been adjusted to calculate the guiding properties of the real fiber.

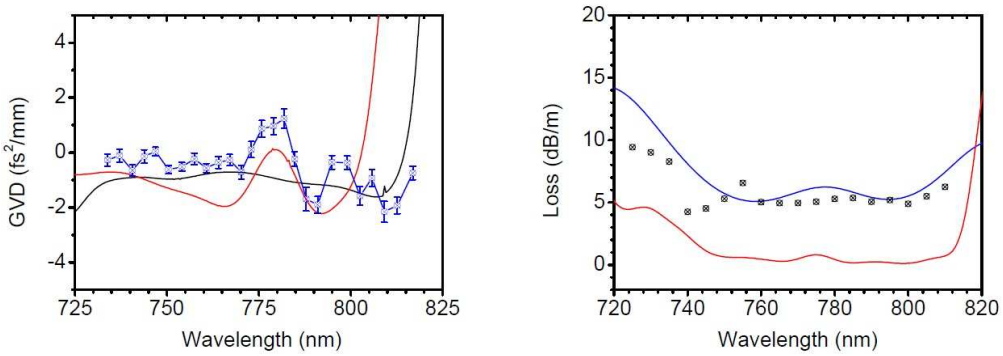

Figure 4.13: *Left:* Measured GVD (blue symbols) of the CPCF shown in Fig. 4.11. The black and the red line represent the numerical results obtained from the calculations of Sec. 4.4. *Right:* Measured loss of the CPCF sample (black symbols) and the numerical simulation (red line). The blue line represents data of an additional loss measurement with a SC source.

4.5.2 Optical properties

For characterization of the fiber samples, a tunable mode-locked Ti: sapphire laser (Spectra- Physics Tsunami) is used as the light source. This laser is tunable in the range from 730 nm to 830 nm and delivers pulses of 100 fs duration over the whole range. In this range, calibrated loss measurements of the fibers are conducted with the cut-back method (see also Sec. 3.1.2). Outside this range, the measurements are augmented with transmission measurements using a white-light continuum source (Crystal Fibres, Femtowhite). The GVD is measured by spectral interferometry [62]. The method is explained in Sec. 3.1.1. The scans are statistically evaluated with care, indicating typical standard deviations on the order of $200 - 300\,\mathrm{fs}^2/\mathrm{m}$. A small number of 12 individual measurements have to be discarded, as markedly higher standard deviations indicate strong variations of laser parameters, most likely due to an atmospheric water resonance at this particular wavelength.

Figure 4.13 shows the measured GVD (left) and loss (right) data as well as the results obtained from numerical simulations for the 22- μm-core-size fiber. The measured GVD data is given as dots with error bars; the measured loss is given as a blue solid line (from the white-light measurement) or as black crossed (cut-back method). The numerical simulations apply a convolution with a Gaussian of 25 nm width, accounting for 3% geometrical size variations of the fiber. Simulations for two differnt ring thicknesses are shown. The error bars in the GVD measurement are deduced from the standard deviation of the total of approximately 250 group-delay measurements for each given wavelength. The 22 μm fiber sample clearly shows a non-vanishing yet still very small negative dispersion value of about 500 fs^2/m. The transmission band of this fiber, however, encompasses a width of only 50 nm (solid blue line and black symbols, Fig. 4.13). The spectral loss profile of the measurements presented in Fig. 4.13 shows a good agreement with the profile calculated with the FEM method ($d = 400\,\mathrm{nm}$) in Sec. 4.4 (shown

here as a red line), however, the absolute value of the calculated losses is constantly 10 dB/m lower than the measured loss. The higher real loss is suspected to be caused by manufacturing imperfections, resulting in random scatting and wavelength independent light leakage at cladding defects. In fact, the fiber is observed to show visible scattering on the entire length of the sample.

Compared to other chirped photonic structures [99, 100], the CPCFs do not show any marked dispersion effect from the chirping itself. In fact, the dispersion of the CPCF in the transmission band closely resembles that of simple optical capillaries [107]. In contrast to one-dimensional photonic structures, the main effect of the chirp is spectral distribution of sharp resonances of the different cell sizes, similar to the effect of the small geometrical imperfections on the structure, but on a wider scale. The effective mode field area of this fiber is $A_{\text{eff}} = \pi r_{\text{eff}}^2 \approx 190\,\mu\text{m}^2$ and the light is almost exclusively guided in air. This results in a negligible nonlinearity for pulses obtained from an oscillator.

4.6 Demonstration of fs-guiding

The main application for a CPCF with a flat dispersion profile is the delivery of ultrashort laser pulses on a meter range. Conventional index guiding fibers with their extremely low losses govern pulse delivery at telecom wavelengths and pulse durations of several picoseconds over a range of hundreds of kilometers. Photonic bandgap fibers with their remarkably low losses and engineerable dispersion have proven suitable for the delivery of different wavelengths and pulse durations of some hundred femtoseconds and several hundred meters distance. However, the delivery of ultrashort laser pulses with duration of less than 50 fs, available from many oscillator laser sources, is extremely challenging with conventional fibers or PCFs. The limiting factors are dispersion and self-phase modulation. For femtosecond pulses, the SPM is especially a limiting factor; even moderate average powers result in extremely high peak intensities; and a huge nonlinear phase shift (Eq. 2.3.1) therefore occurs if the pulses are short enough. Hollow core photonic band gap fibers such as the commercially available HC-800-01 fiber by NKT Photonics [108] effectively bypass the SPM issue because the electric field is guided in the core with a virtually vanishing nonlinearity. Taking this idea to an extreme, the hollow core could be evacuated or flooded with helium to further reduce the nonlinearity.

While exhibiting extremely low losses and an engineerable transmission bandwidth, the major drawback of photonic band gap fibers is the strong slope of the GVD profile (see data in Ref. [108]), resulting in a significant third oder dispersion in the order of $1000\,\text{fs}^3/\text{m}$. Especially for ultrashort pulses, with less than 100 fs pulse duration, this TOD has a detrimental effect on the temporal structure of the guided pulse. The $22\,\mu$m CPCF not only has very small GVD values, but also a flat dispersion profile with virtually vanishing TOD, which makes the CPCF the ideal fiber for ultrashort pulse delivery. Figure 4.15 plots the resulting output pulse duration after 1 meter propagation for the CPCF (black line) and the HC-800 fiber (red line). This calculation illustrates the pulse delivery capabilities of the different fiber types. The CPCF clearly reduces the critical time τ_c ($T_{\text{out}}/T_{\text{in}}(\tau_c) = 2$) from 110 fs to 20 fs.

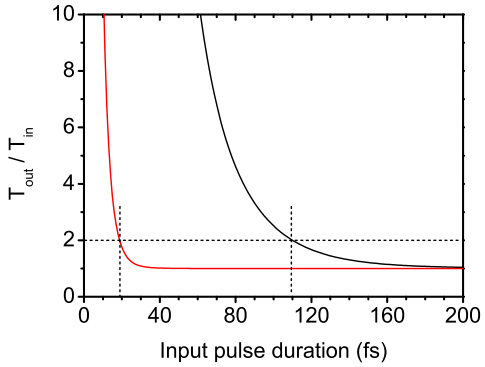

Figure 4.14: The calculated output pulse duration for different input pulse durations and a wavelength of 790 nm after 1 meter propagation in a CPCF (black curve) and an HC-800-01 fiber. The output pulses duration is normalized to the input pulse duration. The dashed lines show the chritical limit of a two times longer output pulse.

The following presents of two experiments demonstrating the enhanced delivery capabilities of a CPCF. The first one compares the guiding performance of the CPCF with the HC-800 fiber. The second experiment demonstrates the guiding of sub-20-fs pulses employing a pre-compensation setup. Both experiments set the current records for the shortest pulses delivered over a meter distance [50, 67].

4.6.1 Comparison between the CPCF and a conventional PCF

Figure 4.15 shows the field development during propagation in 20 cm of CPCF and HC-800-01 for a 50 fs (FWHM) Gaussian pulse. For the simulation, a split-Step Fourier method (assuming vanishing nonlinearity) has been used. The calculation is based on the GVD and loss profiles from Sec. 4.5.2. The the zero on the time axis refers to the relative position of the input pulse in a frame moving with v_g of the input pulse. In agreement with Fig. 4.14, the pulse is not significantly broadened during propagation in the CPCF, while the temporal profile is completely destroyed within the conventional PCF. A more detailed analysis of the latter (Fig. 4.15) reveals details of the broadening effects during the propagation in the TOD dominanted HC-800-01 fiber before the 50 fs input pulse finally becomes a severely distorted series of pulses with a picosecond time signature:

- The peak intensity drops to about 50% of the original intensity in the first centimeters of propagation.
- The pulse duration is constantly increasing.
- The pulse broadens asymmetrically in time with some 10 satellites arising at negative delays, i.e., before the main pulse arrives.

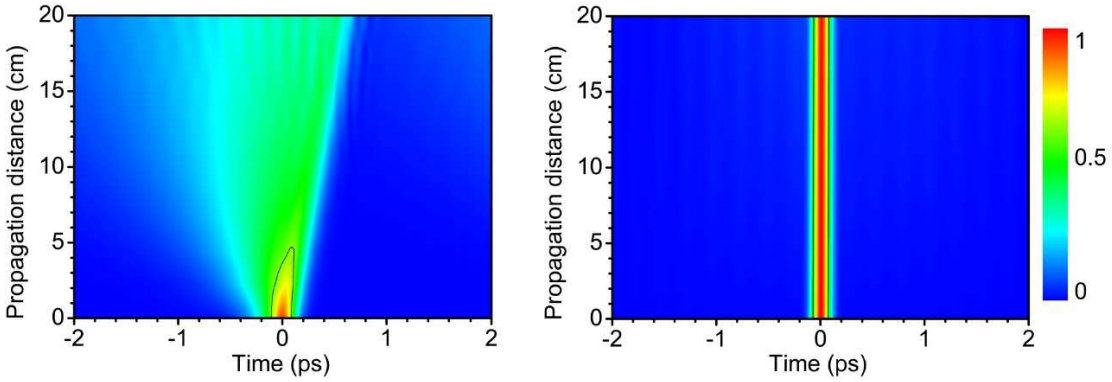

Figure 4.15: *Left:* Calculated electric field envelope (normalized) for a 50-fs pulse in an HC-800-01 fiber at a center wavelength of 800 nm. *Right:* The same pulse propagating in a CPCF. For both fibers the detailed dispersion data from a FEM calculation was used. While the pulse maintains its shape in a CPCF, the temporal structure changes completely in the HC-800-01 fiber.

A propagation experiment was performed to test the numerical predictions and the delivery capabilities of the CPCF at their limits. The experiment used a Ti:sapphire oscillator (Femtolasers femtosource) delivering 13-fs pulses at a repetition rate of 80 MHz; this input pulse duration is even shorter than the critical time τ_c of the CPCF. The pulse duration was chosen to allow the dispersive effects of the CPCF to have a significant influence during the propagation. The pulse duration of these input pulses was measured with an autocorrelation measurement (shown in Fig. 4.16 as blue curve); for the input pulse a hyperbolic secant temporal profile was assumed and the pulse duration has been calculated accordingly. In the first part of the experiment, the pulses are coupled into one meter of HC-800 fiber. On the left side of Fig. 4.16, the measured autocorrelation of the output signal (black symbol) is plotted on a picosecond time scale. The measured autocorrelation shows a remarkable agreement with the autocorrelation calculated from the field using the model above. As expected, the pulse has changed its temporal structure completely and a typical triangular shaped autocorrelation appears.

In the second part of the experiment the same input pulses are coupled into one meter of the 22 μm CPCF sample and the output autocorrelation is again recorded. The measured data is given in Fig. 4.16 on the right hand side on a femtosecond scale. This time, a completely different effect is observed. The autocorrelation preserves its bell-shape, and still assuming a hyperbolic secant temporal structure, an output pulse duration of 25 fs is calculated. Together with the calculations, the assumption that the pulse shape has not significantly changed is reasonable, especially since measured data again agrees well with the calculated trace from the split-Step Fourier method. During one meter of propagation in the CPCF the pulse duration has only doubled and the excellent pulse shape is preserved. A pulse energy of 1.3 nJ is delivered.

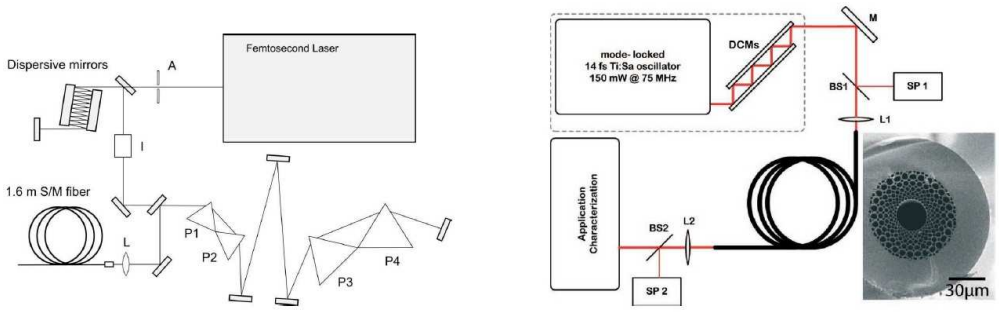

Figure 4.16: The measured autocorrelation signals after 1m of HC-800 fiber(black curve, left side), with an output pulse duration of 3.5 ps; and after one m of CPCF (black curve, right side), with an output pulse duration of only 25 fs. The blue curves in both graphs show the autocorrelation of the 13-fs input pulse. The red curves are the calculated autocorrelation traces from the same model as in Fig. 4.15. The change of the timescale is noteworthy.

This experiment was the first demonstration of guiding in a CPCF and of delivery of 25 fs pulses over a meter distance in a flexible fiber.

4.6.2 Pre-compensated guiding

For the experiments, a CPCF fiber with a core diameter of 26 μm and a five layer photonic cladding was used. The FEM calculations have shown that the slightly increased core diameter does change the absolute dispersion values, but not the qualitative globally flat profile which is virtually constant at a value $\beta_2 = 0.5\,\mathrm{fs}^2/\mathrm{mm}$. In particular, there is no detrimental strong high order dispersion in the wavelength range between 700 and 800 nm as observed in regular hollow core PCFs. Given a one meter length of the fiber and an extra amount of $500\,\mathrm{fs}^2$ for air paths, lenses, and beam splitters, one therefore roughly estimates a necessary $-1000\,\mathrm{fs}^2$ second order dispersion to be pre-compensated. Compared to the large mode area fiber concept of Ref. [109] a 30 times smaller dispersion needs to be compensated, dispersion oscillations [110] are not expected to play a role, and self-phase modulation is not limiting the maximum pulse energy. The most effective way to pre-compensate such a small amount of second order dispersion is the use of chirped mirrors. Compared to other methods, such as prisms or grating based compensation, this method does not create unwanted third order dispersion. And, more importantly, the pre-compensation is readily implemented with no more than 8 bounces off chirped mirrors, each compensating for $\approx 125\,\mathrm{fs}^2$ second order dispersion.

The setup as shown in Fig. 4.17 (right side), consists of a mode-locked Ti:sapphire laser oscillator, the dispersion pre-compensation, and the CPCF with its coupling optics. Beam splitters are used to enable characterization of the pulses from the laser and after transmission through the fiber. The oscillator generates 14 fs pulses at a repetition rate of 75 MHz with a pulse energy of 2 nJ, which translates into peak powers of

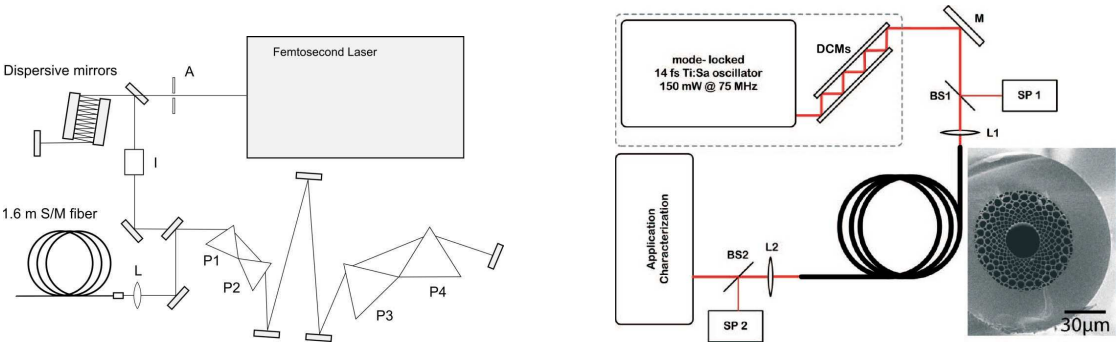

Figure 4.17: *Left:* The setup required to pre-compensate 1.6 meter of commercial LMA fiber (picture taken from Ref. [109]). The setup employs 52 bounces off dispersion compensating mirrors and two prism pairs. *Right:* The setup built to pre-compensate 1 meter of CPCF. This setup requires only 8 bounces off dispersion compensating mirrors.

700 kW at the laser output. In order to ideally match the guiding window of the CPCF, the center wavelength of the oscillator was shifted to 755 nm, i.e., 40 nm below the center wavelength of Ti:sapphire gain. Coupling was accomplished with molded aspheric lenses in order to keep dispersive contributions to a minimum. The total transmission efficiency of the system, including mirror losses, coupling losses, and guiding losses of the fiber, was measured as 8%, with a total delivered power of 10 mW after the fiber. These values can be significantly improved using fibers with larger diameters, as already indicated in [50]. A further reduction of the losses to the theoretical limit of approximately 5 dB/m [111] appears possible by improved manufacturing technologies, therefore reducing the scattering losses inside the hollow core of the fiber.

The input to the delivery system as well as the output from the fiber were carefully characterized by measurements of the interferometric autocorrelation and of the optical spectrum. The interferometric Autocorrelation allowed for a relatively quick comparative scannig over many different chirped mirror combinations. The measured interferometric autocorrelation of the shortest delivered pulses is shown in Fig. 4.18 (a). Figure 4.18 (b) shows the spectral power density of the input pulse (red) and the delivered pulse (black). Comparing the two power spectra, one finds that the laser spectrum appears shifted by about 5 nm towards the red and that there is also a slight reduction in bandwidth, which sets a limit to the obtainable pulse Fourier-limited pulse duration at 17 fs, as shown in Fig. 4.18 (c) as the red curve. The shift is well explained by the asymmetric loss profile of the CPCF sample, which effectively shifts the center wavelength.

In addition to the changed spectrum, the measured IAC after fiber propagation is a further indication that the temporal pulse structure has slightly changed. Considering the pre-compensation and re-compression during the fiber propagation, many changes in the temporal structure could be expected. For further analysis of the modified temporal structure at the output, the intensity autocorrelation was extracted from the measured traces and then a reconstruction similar to the PICASO method [70] was employed, c.f.

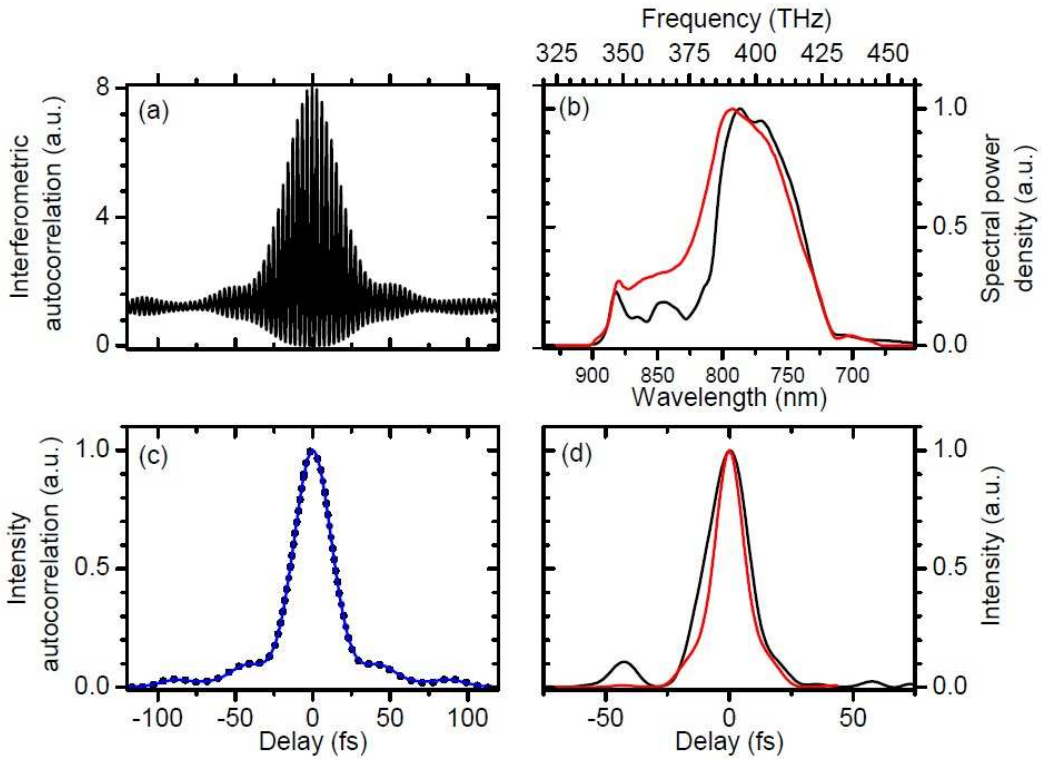

Figure 4.18: (a) Interferometric autocorrelation signal measured after the propagation. (b) Power density before (red) and after (black) the CPCF. (c) Intensity autocorrelation signals extracted from the measured signal (blue) and calculated for the reconstructed pulse shape (black dots). (d) Reconstructed temporal pulse shape (black) and the bandwidth limited pulse (red) calculated from the spectrum shown in (b).

Sec. 3.1.3. This algorithm iteratively fits a phase to the measured spectrum in order to match the calculated with the measured correlation function. Such pulse shape retrieval is certainly not expected to be unambiguous. Yet, given the close proximity of the pulses to their bandwidth limit, a much more reliable estimate of the pulse duration is than simple assumption of a fixed pulse shape is expected. For example, simple assumption of a hyperbolic secant pulse shape leads to an estimated pulse duration of 19 fs. Results of the phase retrieval are shown in Fig. 4.18 (d), indicating a pulse duration of 19.4 fs, which is only 15% above the Fourier limit and the shortest pulse duration ever transported through a fiber. The analysis indicates the presence of only a small satellite pulse, carrying less than 10% of the pulse energy. Compared to previous examples of fiber-based pulse delivery, the pulse contrast has to be considered excellent, with only small traces of a continuum background and no indications of pulse fragmentation. Despite the transmission losses of the fiber, a peak power of 50 kW is therefore still delivered at the end of the fiber, i.e., a value that would have caused severe distortions in any solid-core fiber.

4.7 Conclusion and outlook

This chapter has introduced the idea of a CPCF and presented a theoretical model to understand the unprecedented guiding properties. Even for a quasi-guiding fiber, the dispersion ($\beta_2(\omega)$) of this fiber is remarkably small and in the range of a few fs^2/mm. Additionally, the fiber shows a flat dispersion profile in a transmission band at Ti:sapphire wavelengths. An FEM-based modeling has been proven to allow for accurate and efficient calculation of the guiding properties over a vast wavelength range. High precision GVD and loss measurements are presented, which show a very good agreement to the calculated guiding properties. Two experiments have been performed to test the ultrashort pulse delivery capabilities of the CPCF. The propagation of bandwidth-limited 13 fs pulses has confirmed all previously measured guiding properties and the experimental results agree with a split-step Fourier calculation. Finally, the CPCF is used in a precompensation setup to further reduce the delivered pulse duration. With such a setup, the delivery of sub-20 fs pulses has been demonstrated, which is a new world record for the delivery of an ultrashort pulse in a fiber.

The CPCF samples used in the experiments show relatively high losses of about 5 dB/m, however, the theoretical limit for the loss is much smaller. Improvements of the fiber fabrication process will improve the loss and bring them into the calculated range. Already, the demonstrated transmission of some 10% offers an easy but not very efficient way to deliver ultrashort pulses into experiments. Clearly the transmission efficiency needs to be improved, which is only an engineering problem. The propagation experiments were mainly directed towards pushing the possibilities of distortion-free delivery of ultrashort pulses through flexible waveguides. While a few years ago such femtosecond pulse delivery was limited to 100 fs pulse durations and above, the described scheme of combining an ultralow-dispersion hollow fiber with chirped mirrors has pushed the capabilities by a factor 5 into the sub-20 fs regime. The concept is readily scaled

to higher powers. While CPCF at this stage may still appear unsuitable for therapeutic methods in medical applications or material processing in industry, its potential in terms of temporal resolution lies at hand, e.g., for near-field optical probes, multi-photon imaging techniques or medical diagnostic applications relying on multi-photon excitation. Specifically designed hollow-core fibers therefore open a perspective for applications of femtosecond pulses that are unaccessible to fixed and unflexible arrangements on optical tables.

5 Nonlinear interactions in photonic crystal fibers with a liquid core

This chapter explains an idea to control the nonlinearity in a photonic fiber. Experiments with a water-filled photonic fiber are presented. These experiments have been performed to test a theoretical model describing the generation of a high-power supercontinuum developed by Anton Husakou and Joachim Hermann. The details of this model are explained and experimentally verified.

5.1 Introduction

A broadband, white-light source produced by high-intensity light pulses propagating in various media is a common definition for the term supercontinuum found in a photonics dictionary [112]. Additionally a supercontinuum exhibits high spatial and spectral coherence. The term itself is not restricted to a special kind of underlying nonlinear effect nor is a minimum bandwidth defined. For this work, a white light pulse with a width of at least one optical octave measured at -70 dB below peak is defined as a supercontinuum. The octave is motivated by an important application: f-to-$2f$ interferometry. The -70 dB limit is a common dynamic range of most optical spectrum analyzers.

The generation of supercontinua with ultrashort laser pulses started in 1970 with the work of Alfano and Shapiro [113], enabling the generation of coherent white-light laser beams encompassing one to several octaves of bandwidth [114]. Within the last 4 decades, consecutive decreasing of available pulse duration, increasing peak power, and the development of new materials have allowed supercontinua generation to be reported for many different geometries:

- SC generation in bulk solid or liquid media [115–117],
- SC generation in gas-filled hollow-fibers [58],
- SC generation in filaments [118],
- SC generation in nanowires [119],
- SC generation in tapers [120],
- SC generation in photonic crystal fibers (PCFs) [34, 36, 121].

Different nonlinear effects are involved in supercontinuum generation in different materials. The pulse duration and the pulse energy are also important parameters. Even the

same material can host different nonlinear effects. The generation of SC by picosecond pulses in water observed by Penzkofer et al. [122] shows different characteristics than the generation of SC in a water-filled photonic fiber as reported in this work. Compared to other systems, a fiber features a longer and higher confinement of the light. This results in more spectral change for comparable input parameters. Supercontinuum sources are already available as industrial products and are used in industrial processes as well as in many areas of modern science.The applications include optical coherence tomography [123], frequency metrology [34, 124, 125], and optical sensing [126, 127]. For many of these applications, guided fiber geometries are strongly favored and most commercial devices use either diode- or fiber-lasers directly coupled into the SC generating fiber.

For supercontinuum generation, a solid core fiber with a very small core diameter is usually used. In such a fiber, the light mode is confined to an area of only a few μm^2 and the core can be doped to increase the nonlinearity. Additionally, the spatially confined mode in a single-mode fiber prevents a nonlinearly induced spatial break-up of the beam [128] and allows for a more efficient exploitation of nonlinear optical effects, than spectral broadening in a bulk or liquid media does. In particular, supercontinuum generation in solid-core PCFs garnered extraordinary attention [34]. In PCFs, the supercontinua are generated by soliton fission [35], c.f 2.3.4. This allows for a large range of applications. A detailed review is found in Ref. [121]. Furthermore, soliton-induced SC generation has proven extremely successful for obtaining bandwidths that may encompass up to 4 octaves [129, 130].

The weaknesses of this concept are its lack of scalability and its restriction on oscillator pulse energies. Scaling of pulse energies into the microjoule regime is limited by the small fiber diameter and optical damage of the core material. Since soliton-induced SC generation relies on anomalous dispersion above the pump wavelength, it is intrinsically restricted to geometries with strong waveguide dispersion when Ti:sapphire lasers are used as pump sources. Dielectric hollow waveguides filled with a gas cannot be used for this purpose, because anomalous dispersion can only be achieved for relatively small diameters in the range of 10 to 80 μm, for which the loss in simple hollow capillaries is prohibitively high. Bandgap guiding in hollow-core PCFs, in contrast, allows for much lower losses at the same diameter. Filled with a suitable gas, hollow-core PCFs exhibit anomalous dispersion in the optical range but their bandgap-determined, intrinsically narrow transmission impedes their use for SC generation. In the following chapter, an alternative approach in which a hollow-core PCF is filled with a liquid is applied. In this case, the refractive index in the core is higher than in the cladding and excellent guiding is possible, ensured by a high air-filling factor in the air-glass cladding. Guiding in the liquid-filled hollow fiber is therefore similar to step-index fibers. Such a waveguide exploits the advantage of pumping in the anomalous dispersion regime at 1.2 mm, which is shown to enable a significantly enhanced supercontinuum bandwidth for pulse energies in the microjoule range. A preliminary, much simpler, set-up with a water-filled PCF for single-octave supercontinuum generation has already been employed by Bozolan et al. [131] using a pump wavelength of 980 nm, which is much closer to the zero-dispersion wavelength.

Numerical simulations confirm that despite a higher loss in water, spectral broadening

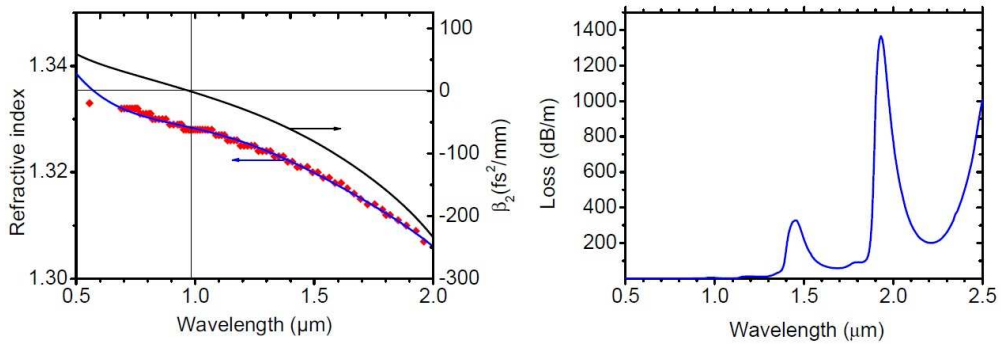

Figure 5.1: *Left:* The real part of the refractive index of water at 22°C and ambient pressure. Red diamonds show the measured data from Ref. [132] and the solid line refers to the model used in this work [133]. The dispersion curve calculated for a HC-800-01 PCF with a water-filled core is plotted as black line (right axis). *Right:* The losses of liquid water at 22°C and ambient pressure. The curve is calculated from the measured data of the imaginary part of the refractive index of water [134].

arises due to the emission of fundamental solitons formed from the fission of the input pulse for small pump intensities. This mechanism is comparable to SC generation in solid-core PCFs. Interestingly, at elevated pump intensities approaching 50 TW/cm^2, supercontinua exhibit a high coherence and the temporal profiles do not show splitting of the pump into fundamental solitons as was typically found in supercontinuum generation in solid-core PCFs. The large broadening here arises due to self-phase modulation combined with four-wave mixing. This is explained by the fact that the fission length is larger than the length, whereby spectral broadening caused by self-phase modulation exceeds one octave.

5.2 Linear optical properties of the filled fiber

The experiment is performed with the commercially available HC-800-01 hollow core photonic crystal fiber [108]. The fiber has a 7-cell core with a 9.5 μm inner diameter and has been designed to support transmission in its gas-filled core. As discussed before, the guiding mechanism is photonic bandgap guiding and the transmission band is a relatively narrow band between 790 and 870 nm. Due to the photonic bandgap guiding, the fiber has an engineerable zero dispersion wavelength (ZDW) and shows the typically strong TOD dispersion profile; the fiber exhibits zero dispersion at midband, i.e., at 830 nm.

Dispersion of the filled fiber

Filling the central core of the fiber with water dramatically changes the linear transmission properties of the fiber, resulting in the essential vanishing of band-gap effects and

narrow transmission bands. The guiding mechanism of light in the filled fiber is now similar to that in a step-index fiber because the refractive index in the core ($n_{\text{water}} \approx 1.33$ at 830 nm) is larger than the average index of the cladding. For the theoretical description of the linear waveguide properties of this water-filled PCF, the effective-cladding model is used. This model has been previously applied to explain the single-mode behavior [135] and to calculate the dispersion of solid-core PCFs [136].

The effective refractive index $n_{\text{eff}}(\omega)$ of the cladding is approximated by that of the fundamental space-filling mode of the photonic crystal using silica-air boundary conditions and periodicity conditions at the limits of an elementary cell. Using $n_{\text{eff}}(\omega)$ as the effective refractive index of the cladding and the refractive index $n_{\text{water}}(\omega)$ of water for the core (see Fig. 5.1), one solves the characteristic equation for the propagation constant $\beta(\omega)$ of the approximate step-index fiber. The curve of Fig. 5.1 (black line, left) shows $\beta_2(\omega)$ of the water filled HC-800-01 PCF. The zero-dispersion wavelength is at 985 nm, and the dispersion is anomalous above this wavelength. In the geometry considered here, the waveguide contribution to dispersion is small in comparison with the dispersion of bulk water, and the curve in Fig. 5.1 (black line, left) is almost identical to the dispersion curve of bulk water.

Losses of the filled fiber

To estimate the loss of the water-filled fiber, the measured loss of water as reported in [134] is used, c.f. Fig. 5.1 (right). The waveguide contribution of the loss is small compared to material loss of water and neglected in all numerical simulations. Water has a strong absorption at wavelengths larger than 1400 nm but a small loss deep into the UV for the considered propagation lengths. The water-filled PCF therefore offers a two-octave wide transmission band with dispersion ranging from +50 to -50 fs^2/mm.

5.3 Simulation of nonlinear propagation

5.3.1 Numerical model

The accurate simulation of the SC generation in the water-filled fiber requires solving the Maxwell equations 2.4 without using the SVEA (c.f. Sec. 2.13) because very short temporal features may occur. The nonlinear Schrödinger equation as presented in Sec. 2.3 is also formulated for the amplitude of the electric field, therefore, the NLS will also give incorrect results when the SVEA is violated. For the numerical simulation of the nonlinear pulse propagation in the waveguide, the so-called forward Maxwell equation [35, 136] is used. This equation does not use the slowly-varying envelope approximation and is written directly in terms of the electric field. This approach allows a correct description of ultrashort temporal features of the electric field or, correspondingly, extremely broad spectra. In this approach the dispersion is included to all orders. Nonlinear effects such as third harmonic generation and self-steepening are included intrinsically. In the

temporal domain, the equation is written as:

$$\frac{\partial E(z,\omega)}{\partial z} = -\frac{\alpha(\omega)}{2}E(z,\omega) + i\left(\beta(\omega) - \frac{n_g\omega}{c}\right)E(z,\omega) + i\frac{\omega^2}{2\beta(\omega)\epsilon_0 c}P_{NL}(z,\omega), \quad (5.1)$$

where $E(z,\omega)$ is the Fourier transform of $E(z,t)$, z the propagation coordinate, $\beta(\omega)$ the wavenumber of the waveguide, and $\alpha(\omega)$ the loss coefficient. Comparing this equation with Eq. 2.39, which is formulated in the other Fourier domain, the same mathematical structure is found, and the same numerical tools can be used to solve the propagation.

In Eq. 5.1 n_g is the effective group refractive index, which determines the velocity of the moving coordinate frame. $P_{NL}(z,\omega)$ is the Fourier transform of the time-dependent nonlinear polarization $P_{NL}(z,t)$, which includes an instantaneous contribution due to the electronic hyperpolarizability and a second non-instantaneous contribution

$$P_{NL}(z,t) = \epsilon_0\chi^{(3)}E^3(z,t) + \kappa_{slow}\frac{\epsilon_0\chi^{(3)}}{\tau_{slow}}E(z,t)\int_0^\infty E^2(z,t-\tau)\exp(-\tau/\tau_{slow})d\tau. \quad (5.2)$$

Here $\chi_{(3)} = (4/3)c\epsilon_0 n_W n_2$ is the third-order hyperpolarizability, and n_2 is the nonlinear refractive index. The second term describes a slow nonlinear response of the medium similar to the one introduced in Eq. 2.35. κ_{slow} determines the fraction of the retarded nonlinear response in water, and τ_{slow} is the decay time of the response. For the calculations presented, the parameters $n_2 = 1.5 \times 10^{-4}$ cm^2/TW [137], $\tau_{slow} = 120$ fs, and $\kappa_{slow} = 0.25$ [138] have been used. Although the fiber being considered supports a large number of modes, their influence was neglected since the input radiation was coupled exclusively to the fundamental mode and nonlinear energy transfer to higher-order modes can be neglected for the considered nonlinearities and propagation lengths.

5.3.2 Numerical results

The propagation equation Eq. 5.1 has been employed to simulate pulse propagation as well as supercontinuum generation for 40 fs pulses at 1200 nm by using the linear optical properties of the waveguide from Sec. 5.2 and the non-instantaneous nonlinear response function of water. The simulation was done for multiple intensities and presents two different peak intensities in order to illustrate two contrasting SC generation scenarios.

Low intensities

In the first simulation, a low peak intensity of 2 TW/cm^2 is assumed. The spectral and temporal evolution of the pulse for this simulation are presented in Fig. 5.2. The evolution of the temporal profile in Fig. 5.2(b) confirms fission of the input pulse into three fundamental solitons after a propagation length of about 0.6 cm, resulting in the formation of a supercontinuum. Details of the spectral broadening process are displayed in Fig. 5.2(a). For clarity, Fig. 5.3 shows a spectral (a) as well as temporal (b) snapshot after 1.6 cm propagation. In both domains, the pulses display the same features (spectral

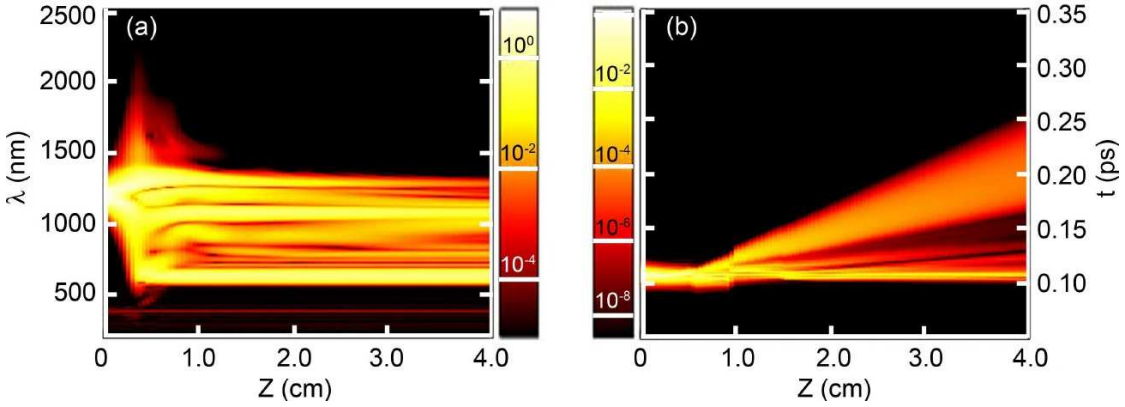

Figure 5.2: Evolution of spectrum $I(z, \lambda)$ (a) and of temporal profile $I(z, t)$ (b) with propagation for 40 fs, 2 TW/cm^2 pulses with central wavelength at 1200 nm and waveguide parameters as in Fig. 5.1.

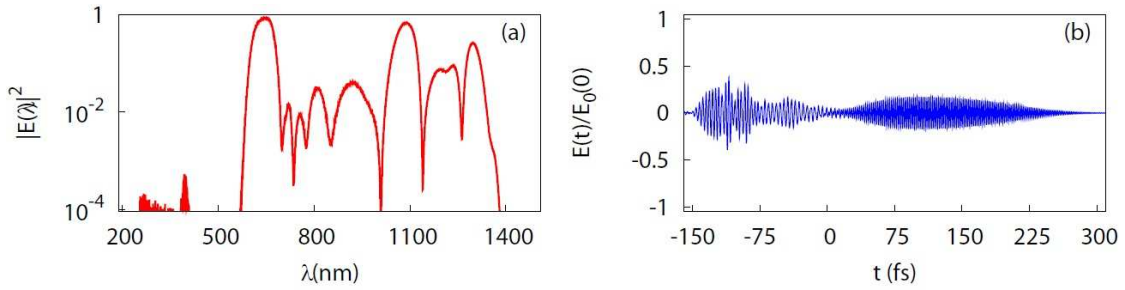

Figure 5.3: Spectrum (a) and temporal profile (b) after 1.6 cm propagation. The parameters are the same as in Fig. 5.2.

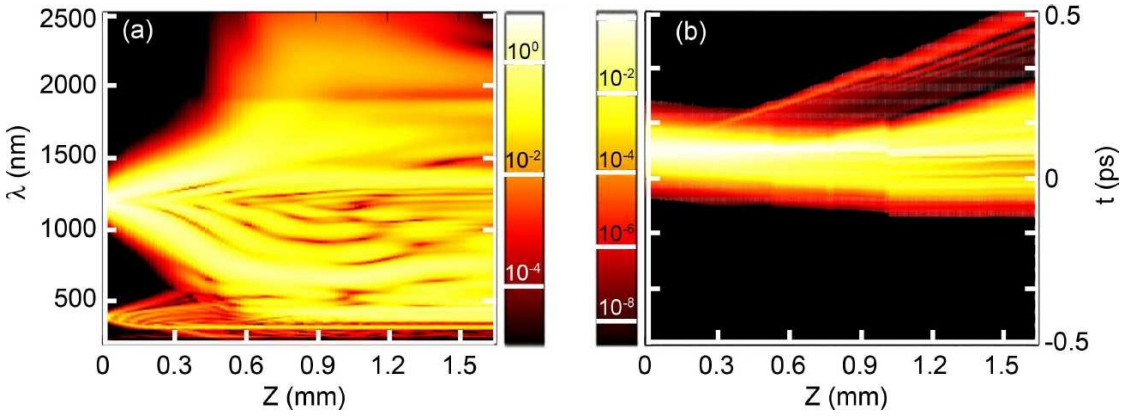

Figure 5.4: Evolution of spectrum $I(z, \lambda)$ (a) and temporal profile $I(z, t)$ (b) with propagation for 40 fs, 50 TW/cm^2 pulses with central wavelength at 1200 nm and waveguide parameters as in Fig. 5.1.

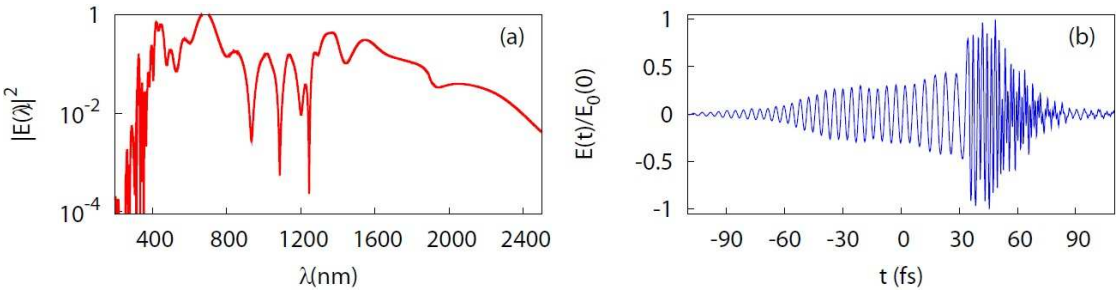

Figure 5.5: Spectrum (a) and temporal profile (b) after 0.46 nm for 40 fs, 50 TW/cm^2 pulses with central wavelength at 1200 nm.

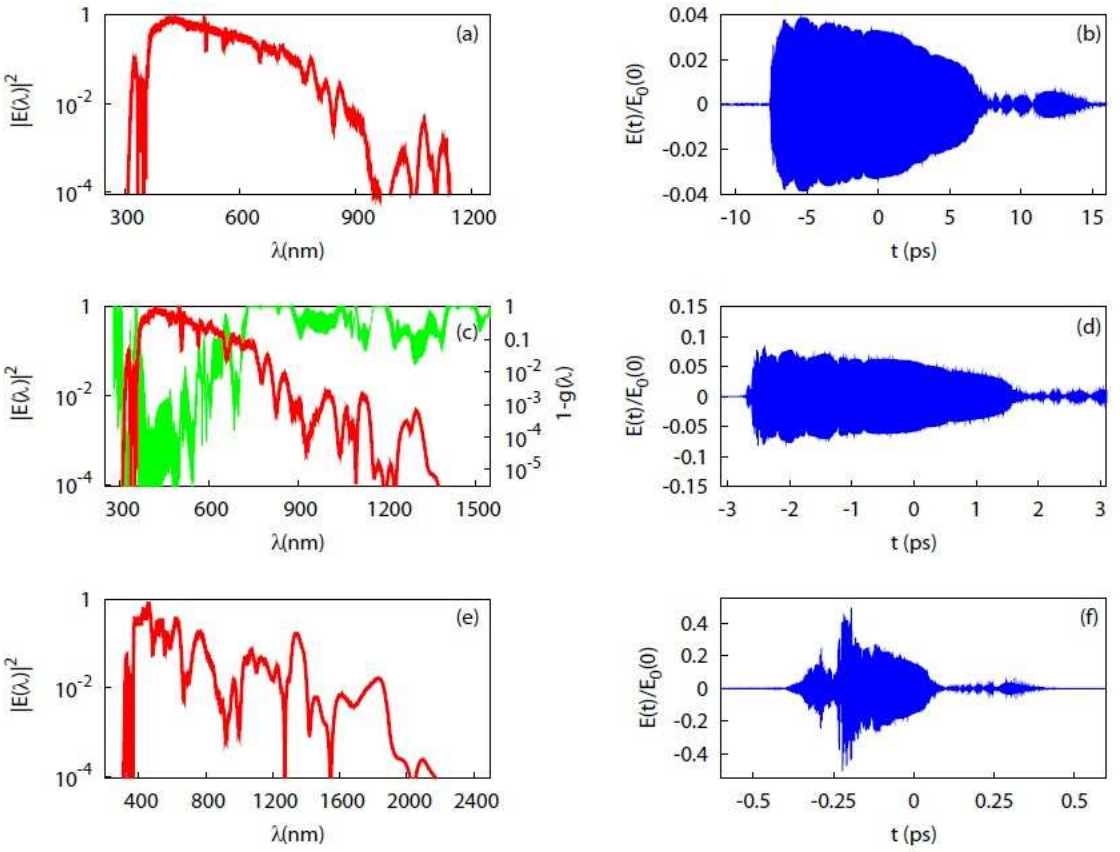

Figure 5.6: Spectra (a),(c),(e) and corresponding temporal profiles (b),(d),(f) for propagation distances of 8 cm (a),(b), 2.4 cm (c),(d), and 0.24 cm (e),(f). The input 40 fs pulses at 1200 nm have a peak intensity of 50 TW/cm^2. The fiber geometry corresponds to the experimental cross-section. In (c) the incoherence $1 - g(\lambda)$ is illustrated by the green curve.

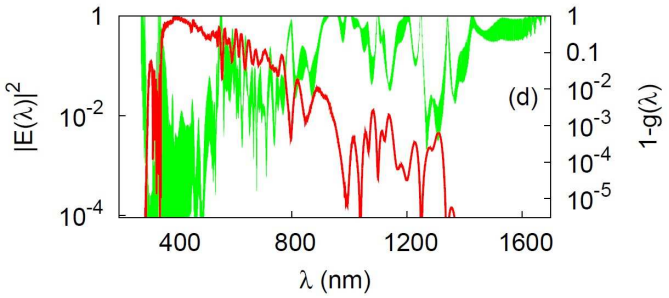

Figure 5.7: Spectrum (thick red curve) and incoherence function (thin green curve) for the model without the retarded nonlinearity contribution ($\kappa_{\mathrm{slow}} = 0$). The input 40-fs pulses at 1200 nm have a peak intensity of 50 TW/cm^2, the propagation distance is 2.4 cm.

width, spectral distribution, and sharp spikes in the temporal structure) as have been observed for solid-core PCFs. Analogous to the case of a solid-core PCF and using comparable intensities, therefore, supercontinuum generation in the water-filled PCFs is related to soliton dynamics and appears due to the emission of non-solitonic radiation at different frequency intervals [35, 136].

Since the chosen intensity is much smaller than the intensity used in the demonstration experiment, the results of this simulation cannot be used to explain the SC observed in the experiment. In the finding that a very efficient SC generation mechanism also exists for low pump intensities makes the concept of a liquid core fiber additionally promising for other pump sources with lower pulse energy.

High intensities

In order to explain the observed SC generation for pulse energies as used in this experiment, the simulation was repeated at a higher intensity of 50 TW/cm^2. The results of nonlinear pulse propagation at this energy are shown in Fig. 5.4. Again, a snapshot of the temporal and spectral profile after only 0.46 mm propagation length is shown separately in Fig. 5.5. In terms of intensities, this situation is now much closer to the experiment that will be described in Sec. 5.5. In this case, the spectrum already reaches two-octave coverage after only 0.6 mm propagation, see Fig. 5.4(a). In the snapshot in Fig. 5.5(a) the spectrum spans 390 to 1900 nm wavelength. However, in contrast to low intensities, no indications for fission of the pulse can be seen at this distance. Instead, the temporal profile in Fig. 5.5(b) shows a smooth pulse shape without the spikes characteristic of soliton fission processes. This is a clear indication that self-phase modulation dominates the spectral-broadening process. This means that the mechanism of supercontinuum generation fundamentally differs for different intensities, even though the pump is within the anomalous dispersion region in both cases.

The prevalence of self-phase modulation at higher intensities can be explained qualitatively by the fact that the length $L_{\mathrm{oct}} \approx L_{\mathrm{NL}}\omega_0/\Delta\omega_0$ at which self-phase modula-

tion leads to a spectral width exceeding one octave, is smaller than the fission length $L_{\text{fission}} \approx N L_{\text{NL}}$. The nonlinear length L_{NL} is defined as $L_{\text{NL}} = (\gamma P_0)^{-1}$ with the nonlinear coefficient γ, the central frequency and the spectral width of the input pulse ω_0 and $\Delta\omega_0$, respectively, and the soliton number $N = \sqrt{L_{\text{D}}/L_{\text{NL}}}$, $L_{\text{D}} = (\tau_0)^2/|\beta_2(\omega_0)|$ [17]. In the case of the low-intensity pulse, one can estimate $N = 5$ and $L_{\text{NL}} = 0.63\,\text{mm}$, $\omega_0/\Delta\omega_0 \approx 10$. Therefore, the fission length $L_{\text{fission}} \approx 5L_{\text{NL}}$ is smaller than $L_{\text{oct}} \approx 10L_{\text{NL}}$. In this case the mechanism of soliton-induced supercontinuum generation dominates over self-phase modulation. In the high-intensity case, $N = 29$ and $L_{\text{NL}} = 0.025\,\text{mm}$, the fission length is larger than the length $L_{\text{oct}} \approx 10L_{\text{NL}}$. Spectral broadening is therefore dominated by self-phase modulation. After the pulse has evolved to such broad spectrum, a higher-order soliton can no longer be formed, and the soliton fission effect does not appear due to the influence of loss and higher-order effects. Although soliton dynamics obviously do not play a role here, weak or anomalous dispersion is nevertheless an important requirement for the spectral broadening efficiency of the self-phase dominated mechanism. Strong normal dispersion effectively limits the spectral broadening effect due to temporal stretching and it also limits the decrease of the maximum intensity by dispersive effects. In Figs. 5.6(a)–5.6(f), the spectra and corresponding temporal shapes of the high-intensity pulses are presented for larger propagation lengths. Upon further propagation, the pulse envelope continues to smoothen and extends under the action of the group velocity dispersion to several picoseconds. At a propagation distance of 0.24 cm, the theoretical spectra show reasonable agreement with the experimental ones in Sec. 5.5. In the simulations, water absorption leads to extinction of the spectral components in the range above 1200 nm upon further propagation. It is important to note that in the experiment these components can be guided in the cladding modes of the fiber and contribute to the observed spectral power density at the fiber output. The field extension into the cladding is insignificant and the cladding itself does not contribute to the spectral broadening; cladding modes can preserve the radiation above 1300 nm that is coupled to them by fiber imperfections. Despite its obvious existence, this effect cannot easily be considered in the simulations. Note, however, that the numerically computed spectra are significantly broader than those for bulk water, even if an identical anomalous dispersion is considered (see, e.g., [115]). Focusing a laser tightly to a spot size comparable to the fiber diameter limits the effective interaction zone to a few hundred microns due to diffraction and the maximum obtainable nonlinearity due to the on-set of filamentation.

Improved coherence properties

In Fig. 5.6(c) the incoherence $1 - g(\lambda)$ is shown as the green curve. The displayed first-order coherence function $g(\lambda)$ is defined as

$$g(\lambda) = \Re\left[\frac{< E_a(\lambda)E_b^*(\lambda) >_{a,b,a\neq b}}{< E_a(\lambda)E_a^*(\lambda) >_a}\right], \tag{5.3}$$

where the average in the numerator is taken over all non-identical pairs of noise realizations a, b, while the average in the denominator is taken over all noise realizations [121]. The quantity $g(\lambda)$ directly corresponds to the visibility $V = g = (I_{\max} - I_{\min})/(I_{\max} + I_{\min})$ measured in interference experiments. Although the input pulse parameters correspond to a high soliton number $N = 29$, a high average output coherence of 0.97 is observed. This is an important feature since the spectrum becomes incoherent in soliton-induced supercontinuum generation if the soliton number is larger than $N \approx 10$ [121]. Despite the larger pulse energies and the relatively high soliton number, the coherence properties have therefore improved compared to solid-core PCFs in the nanojoule regime. These improved coherence properties appear because spectral broadening is now caused by self-phase modulation, which, in general, preserves a high coherence. This novel high-intensity regime appears interesting for the generation of highly coherent supercontinua with longer input pulses. In contrast, such conditions are difficult to meet in solid-core PCFs due the requirement of a soliton number $N \leq 10$ for maintenance of coherence.

Finally, in order to elucidate the role of the slow component in the nonlinear polarization Eq. (2), Fig. 5.7 shows simulation results computed with the same input parameters and at an identical propagation distance as in Fig. 5.6, but without the influence of the retarded nonlinearity, i.e., $\kappa_{\text{slow}} = 0$. It can be seen that the spectrum at 2.4 cm is slightly narrower than for the previous case and that the average coherence is roughly the same, i.e., 0.96. Therefore, a marked influence of the slow component is not expected.

5.4 Fiber preparation

The methods presented here were originally developed in the group of F. Mitschke to investigate the filling of PCFs with different dyes [139]. In collaboration with F. Mitschke the methods are adapted and improved for the experiments presented below.

5.4.1 Use of a fusion splicer to collapse the microstructure

The major difficulty in using water in a partially air-clad geometry arises from selective filling of the central hollow core. Several methods have been discussed for sealing the micro-channels in the cladding region lest intruding water corrupt the index contrast required for guiding in these fibers. Martelli et al. [140] suggested splicing of a fiber with a single hollow core to selectively seal off the air holes in the cladding. Huang et al. [141] demonstrated the use of a UV curable adhesive for the same purpose. Several publications suggest the use of a fusion splicer for collapsing the cladding part of the microstructure [142, 143]. These publications report using a pair of electrodes in front of the fiber tip. For the experiments presented here, this idea is adapted, improving the technique by shifting the electrodes of the fusion splicer approximately 100 μm in direction of the fiber, i.e., away from its end face [144]. This effectively avoids a reduction of the core diameter in the collapsed region. This bottleneck effect has previously been found disadvantageous for applications, since a reduction leads to a decreased filling rate and, more importantly, causes severe coupling problems.

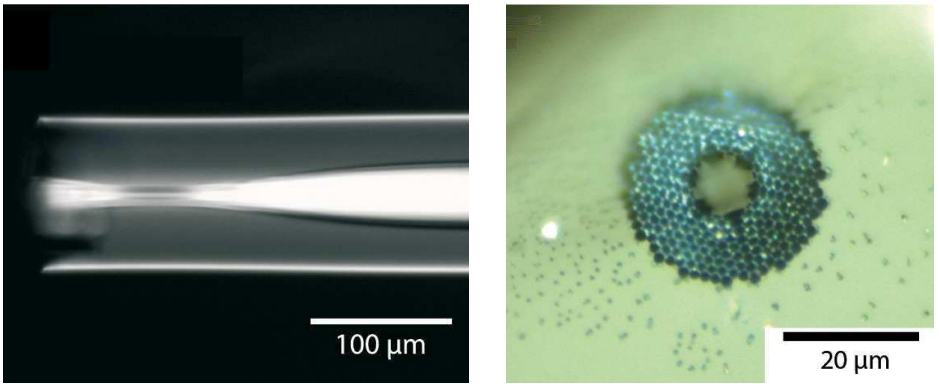

Figure 5.8: *Left:* Micrograph of the collapsed fiber as seen from the side. *Right:* Micrograph of the rear end of the fiber demonstrating that the core is selectively filled with water.

In the experiments, a standard single-mode-fiber fusion splicer (Fitel type S148S) is used. The device employs a distance of 1.6 mm between the electrodes and allows for current adjustment in the range from 8 to 14 mA. Compared to the parameters given in [143], a relatively low current of 9.41 mA is used at an increased arc exposure time of 550 ms [144]. The fiber is not pulled or otherwise mechanically stressed during the arc exposure. It is found that these parameters enable collapsing of the microstructured cladding without significantly reducing the diameter of the central hollow core. The absence of a bottleneck is proven by simultaneously filling a hollow fiber with water from both ends; identical filling velocities are observed. Figure 5.8 (left side) shows a micrograph of the partially collapsed fiber structure as seen from the side. This micrograph indicates a total length of the modified microstructure of about 380 μm, with the length of the collapsed region being less than 60 μm. As only the latter prevents index guiding, the resulting loss is minor compared to absorption losses in the water. A frontal micrograph image of the same fiber in shown on the right side of Fig 5.8. The rear end of the fiber is already mounted in a water reservoir and the core is filled with water. This picture proves that the core can be filled selectively with the method here presented and that no disturbing water will be observed in any of the cladding channels. The method is an easy-to-use, one-step method and is very reliable.

5.4.2 The use of a windowed cuvette

The problem for experiments in a liquid core fiber as prepared in Sec. 5.4 is the formation of a meniscus inside the fiber core. The shape of this surface is determined by fundamental mechanical capillary forces [142, 145, 146]. The orientation of the meniscus depends on the contact angle θ between the liquid and the fiber material [146, 147]. Figure 5.9 (left side) shows the meniscus for a wetting (a) and a non-wetting (b) liquid as well as a micrograph of a meniscus formed in a capillary of 50 μm diameter. Due to the different index of refraction, the bent surface of the meniscus acts like a lens. For

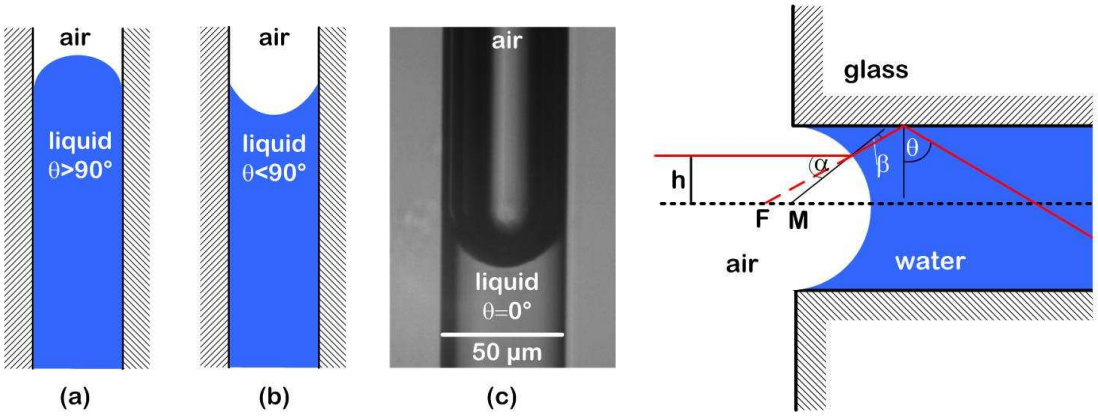

Figure 5.9: *Left* (a) and (b) show the typical shape of an air/liquid interface. Wetting liquids ($\theta < 90°$) have convex interfaces (a), while non-wetting liquids with $\theta > 90°$ have concave interfaces with air. (c) A micrograph of a water-filled capillary with 50 μm diameter. Since θ is almost zero for a glass/water surface, the interface is an almost spherical concave shape. *Right:* Optical beam path for a beam parallel to the distance h from the optical axis. If $\beta >\approx 52°$ the beam is totally reflected and guided in the water-filled core of the fiber.

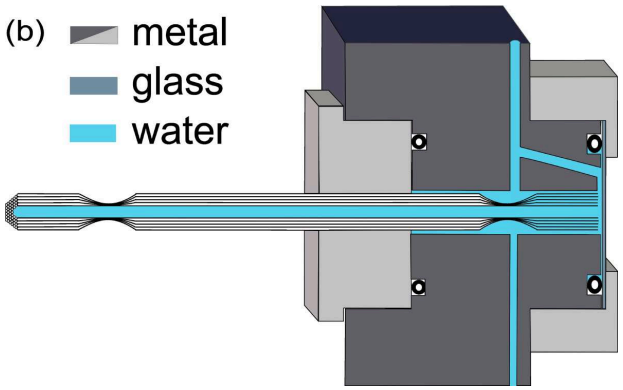

Figure 5.10: Sketch of the windowed cuvette built for the experiments. All water/air surfaces are technically prevented. The 500 μm window allows for the use of ultrashort laser pulses. The drainage channels enable quick and complete filling with any kind of liquid and prevent the formation of bubbles.

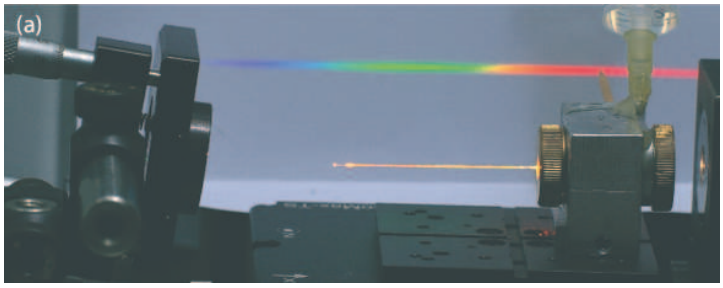

Figure 5.11: Photograph of the supercontinuum generated in the liquid core of the water-filled fiber mounted inside the windowed cuvette. Orientation is as in Fig. 5.10(b). The grating-dispersed supercontinuum has been projected onto a screen behind the set-up.

a core diameter of 10 μm, the surface is of almost ideal spherical shape which results in severe geometrical aberration. The focal lengths are spread out over some 5 μm and strong chromatic aberration is also created. As a result, the total amount of coupled energy is reduced to just a few percent. To avoid this effect, a windowed cuvette is used, see Fig. 5.10. This cell features drainage holes to prevent the formation of air bubbles. The fiber tip is located as close as possible to the thin glass window to avoid excessive dispersion on the input coupling side. An $f = 18$ mm lens is used for coupling into the fiber. This set-up enables an insertion efficiency of $> 30\%$ in the absence of absorption and nonlinear optical effects. For the experiments presented in the next section, a water-filled fiber with a length of 7.2 cm and a gap of approximately 500 μm between front end and window is chosen. The rear end of the fiber is not mounted into a second cuvette, as only the spectral characterization of the generated SC was planned. The meniscus at the rear end causes a strong divergence of the output beam. This, however, can be easily compensated by a simple lens.

5.5 Experiments

The experiments are performed with 45 fs laser pulses from an optical parametric amplifier (OPA), pumped by an 800 nm regenerative Ti:sapphire amplifier at a repetition rate of 1 kHz. The OPA is tuned to a center wavelength of 1.2 μm. The output power of the OPA is attenuated, and the energy per pulse launched into the core mode is 7 μJ, corresponding to an input peak power of approximately 150 MW. In the experiments, a total coupling and transmission efficiency of about 6% is observed, resulting in an output energy of the continuum of 390 nJ [144]. At first glance, this may seem to be a rather low value. However, it surpasses the computed transmission of 1200 nm light in a 7.2 cm long water column by a factor 100, cf. Fig. 5.1 (black line, left).

Figure 5.12(a) shows the spectral power density of the generated supercontinuum in a logarithmic plot. The spectrum, measured at -20 dB below peak, covers a bandwidth of 1.0 μm, ranging from 500 nm to 1.5 μm. The -30 dBm bandwidth spans a spectral range

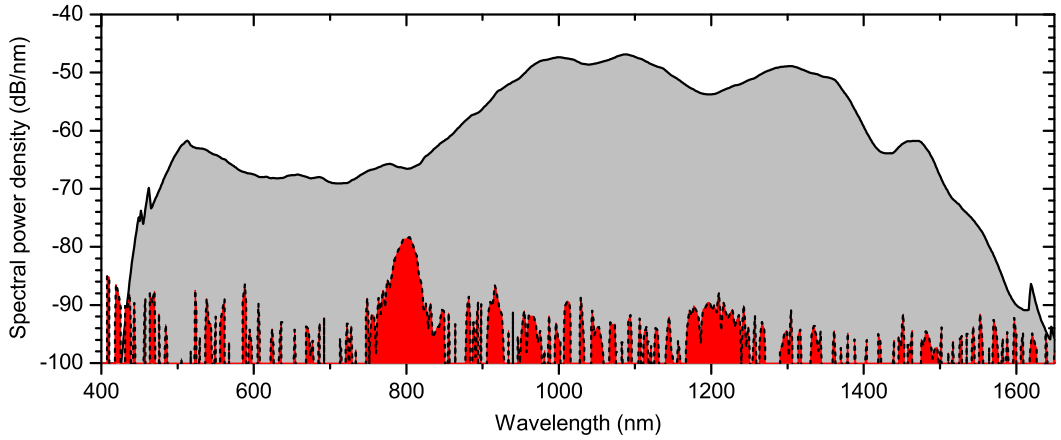

Figure 5.12: Measured spectra of a supercontinuum generated in 7.2 cm of water-filled hollow core fiber. Full range of the OSA on a logarithmic scale. Red colors indicate a background stemming from scattered light, recorded while no light was coupled into the water core.

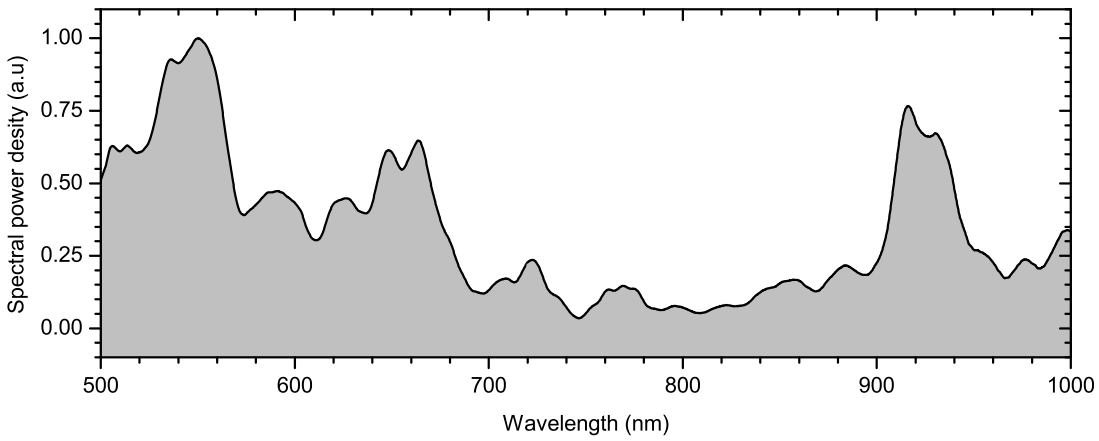

Figure 5.13: The measured spectra of a supercontinuum generated in the same fiber as in Fig. 5.12 on a linear scale; recorded between 500 nm and 1 μm with a high resolution spectrometer.

of $\approx 1.2\,\mu$m, starting at 430 nm and ranging to $\approx 1.6\,\mu$m. The significantly higher cut-off in the infrared is attributed to light that is guided in cladding modes because water absorption should otherwise inhibit supercontinuum generation above approximately $1.2\,\mu$m. For comparison, Fig. 5.12(a) also shows the background radiation, which is mainly caused by scattered laser light. One can identify the Ti:sapphire laser at 800 nm and the $1.2\,\mu$m signal wave of the OPA.

The supercontinua show the highest spectral power densities in the vicinity of the $1.2\,\mu$m OPA pump. The spectrum exhibits two symmetrical maxima at approximately 1100 and 1350 nm. In addition to the symmetric broadening, a second optical octave at roughly 10 times lower power densities can be seen below 800 nm [c.f. the linear plot in Fig. 5.13(b)]. The photograph of the spectrally dispersed supercontinuum in Fig. 5.11(a) further confirms coverage deep into the blue spectral range. Appearance of this band in the visible is only explainable by solitonic effects, as was discussed in Sec. 5.3.

5.6 Conclusions and outlook

The generation of a two-octave spanning supercontinuum in a liquid core PCF has been demonstrated. The fiber has been prepared in an one-step method using a standard fusion splicer. The coupling efficiency has been optimized using a windowed cuvette. The emitted white-light of 390 nJ power surpasses the strongest commercially available conventional source by a factor of 10. The numerical simulations show that two different generation mechanisms for ultra-broad supercontinua compete in a liquid core fiber. Depending on the soliton number of the input pulse, either self-phase modulation or soliton fission is the dominant mechanism. The demonstration experiment has been performed in the self-phase-modulation dominant regime. The advantage of this regime is a superior coherence compared to the solitonic regime.

The numerical simulations also reveal that the full spectral bandwidth is already generated in the first 0.5 mm of the fiber. Since no additional spectral components are generated during the rest of the propagation and the generated light suffers from high absorption above $1.5\mu m$, it seems reasonable to create extremely short fiber samples, which would offer even higher output power. However, the practical preparations of shorter liquid core fiber samples is technologically challenging.

The technology presented here makes the scaling of SC power into completely new ranges possible, since the nonlinear medium can be continuously replaced and cooled. Only pulse energy and pulse duration need to be carefully selected to keep the soliton number in the required range. As a final thought, entering solitonic generation regime would be promising, because the input power converts more efficiently into the output pulse and the broadening happens on a cm scale rather than on a sub mm scale. This latter fact especially would allow the study of the generation mechanism in greater detail by cutting back the fiber sample.

6 Two pulses: An optical transistor

In this chapter the nonlinear interaction between two ultrashort laser pulses during the propagation in a PCF is discussed. A novel interaction effect is observed. Calculations reveal that the physics of this effect can be used to create a transistor-like device for photons with the dispersion being the key parameter for this effect [148]. A number of criteria according to Miller [149] are presented, which allow a decision as to whether or not a specific optical switching effect can practically replace an electronic transistor. These criteria are then applied in a brief review of earlier work contributing to the realization of optical transistors. Then the idea of using the nonlinear interaction of two ultrashort pulses in a fiber as an optical transistor is presented. Based on the theoretical findings, an experiment is set up and the effect is demonstrated in a commercial PCF. Finally, the experimental results are compared with the numerical simulations carried out for the particular piece of fiber used in the experiments; excellent agreement is found.

6.1 The optical transistor: Overview

The transistor is one of the most important components in electronics. In 1956 the Nobel prize in physics was awarded to William B. Shockley, John Bardeen, and Walter H. Brattain *for their researches on semiconductors and their discovery of the transistor effect* [150–152]. The most common semiconductor transistor used today is, in fact, the bipolar-junction-transistor. A typical device is usually realized as a sandwich of either npn doped or pnp doped semiconductor layers. Figure 6.1 illustrates the schematic design and function of a pnp-type transistor. This type of transistor effectively works as a current amplifier, i.e., a small current between emitter and base allows controlling a much larger current between emitter and collector. Only a very small current from the base to the emitter is required in an electronic transistor because the switching is actually controlled by the potential in the emitter as illustrated in Fig. 6.1.

Translating this concept into photonics, not only would an optical transistor be able to switch a laser beam on and off by means of a secondary beam, but, additionally, a weak laser (small optical power) would be able to control a stronger beam (high optical power). The idea to build such a transistor-like device for photons rather than for electrons has been discussed ever since the invention of the laser. In the last few decades, the topic has become even more relevant with the rapid development of optical fiber communication networks.

Initial working optical transistor schemes were presented in the mid 1980s based on optical bistability [153–158]. The optical bistability was observed in a device combining a Kerr medium (gases, liquids, or semiconductors) with a Fabry-Pérot cavity. Also the

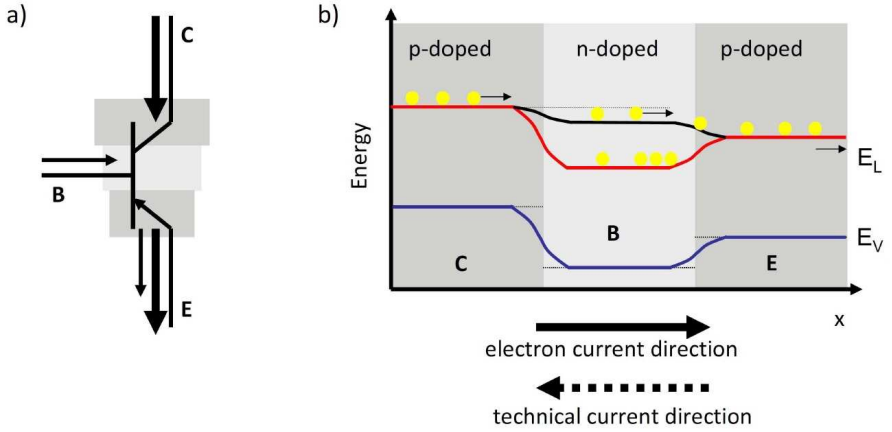

Figure 6.1: Schematic illustrations of an electronic transistor. (a) technical symbol of a pnp-transistor and an illustration of the electron current in the transistor. (b) Illustration of the electronic band model. The position of the conduction band in the p-doped layer (red or black level) depends on the potential (voltage) between the base (B) and the collector (C). This voltage controls the switching in the transistor. The small current from the base to the emitter (E) is based on electron hole recombination and hole transportation.

nonlinear absorption in a Fabry-Pérot cavity was used to demonstrate optical bistability [159]. Bistability devices depend on a strong $\chi^{(3)}$ which requires the operation close to a resonance; this operation is limited by two photon absorption [160].

Most publications about all-optical switching focus exclusively on the use of an optical transistor in a future, as-of-yet nonexistent, optical computer, and other very promising applications are often overlooked. Other important applications include: ultrafast optical switching in telecommunication networks, the switching of strong pulses with a weaker pulse in scientific experiments, and the creation of a photonic equivalent of an operational amplifier. Compared to the total number of different electronic realizations, the number of working photonic transistors is still small, and the research is still at a very early stage, although it has been more than 30 years since the first device was operational. Today, different concepts are evolving, but none has yet reached the stage of commercial use. In fact, most of the current concepts cannot be integrated and mass production still lies far in the future.

6.1.1 Criteria for practical optical logic

In order to assess different physical effects and to compare their performance as an optical transistor a list of criteria is needed. In Ref. [149], Miller presented a list of stringent criteria that he considered mandatory for any practical optical transistor to comply with. In the following, this list is reviewed, further developed, and the compliance of several optical transistor concepts is examined.

Basic transistor operation (fan-out and cascadability) An optical transistor must have the same switching behavior for light as the electronic transistor has for switching currents, i.e., a small amount of photons must switch a large amount. The technical terms used in electronics are fan-out and cascadability. The output of one device must be able to drive at least two subsequent devices of the same type. In practical terms this means that a lower pulse energy must be able to control a signal pulse with at lest double the pulse energy. At the very minimum, the wavelength, the temporal pulse profile, and the beam quality must be maintained for at least the signal pulse. This is the most basic criteria for an optical transistor. Surprisingly, many of the previously reported schemes fail already here.

Time scale of operation To illustrate the advantage of an optical transistor, the minimal response time of nonlinear optical effects is often quoted and the possibility of an increased number of logic operations per second is a common argument. However, current CMOS electronics already operate in the picosecond range [161–163] and future generations are likely to break the 100 fs mark [163]. Optical transistors are supposed to work in a network with electronic transistors. In order to fall into step with the electronic transistors the optical logic gate must work in the sub-100 fs regime. Alternatively, the devices must allow for massive parallelization to not slow down the network. As discussed in Sec. 4 optical propagation comes with some limitations and virtually loss-less transmission in optical waveguides needs to be rethought for such short pulses. Only extreme miniaturization and very short distances between the logic gates would allow for propagation effects to be neglected.

Energy conversion and conservation Every electronic logic operation requires electrical energy which is usually converted more or less directly into heat. A typical CPU can emit up to 125 W/cm^2 of heat [164]. The energy consumed by data centers in the US for 2011 is estimated to be over 100 billion kWh [164], however, a single logic operation in current silicon CMOS electronics requires only some femtojules of energy and in future generations this number will be reduced to a few ten attojoule [163]. This sets a performance goal for the optical logic. For an optical transistor operating at typical laser wavelengths (visible and close-to-visible wavelengths) this requires an operation with only some hundred photons. The number discussed here is the total amount of consumed energy in one logic gate, including losses in the waveguides, losses by thermal heating of the nonlinear material, as well as photons lost in other photonic effects.

Usability in logic gates The effect must also fulfill a number of practical criteria which allow for building complex optical logic devices. The quality of the signal and its level must be restored in every logic gate, i.e., degradations are not amplified but damped by the optical transistor (*logic-level restoration*). The input and the output signal should be easy to separate and not interfere with each other. Ideally, the device would feature separate input and output beams (*input/output isolation*). The operation point of the device should be robust, non-critical and the same for every device built of the same

type (*absence of critical biasing*). Furthermore, the logic operation should not depend on transmission loss, because the distance between the gates will vary in assembly. Defining a power threshold level cannot reliably distinguish between on and off unless the threshold is pushed close to zero. *(logic level independent of loss).*
The above criteria allow the performance of an optical effect to be evaluated. Except for fan-out and cascadability, none of them is a an absolutely necessary criterion, but non-compliance with each individual criterion decreases the likelihood of the effect becoming part of a future photonic technology implementing optical logic units.

6.1.2 Different optical transistor realization approaches

This section gives an overview on three selected recent research results in the field of optical switching and optical transistors. The performance is rated by the criteria developed. Each experiment follows a different approach and utilizes a different physical effect. All effects operate at a different combination of wavelength and pulse duration, and the criteria developed above need to be employed to compare their performance.

A single molecule optical transistor V. Sandoghdar's group in Zurich is working on the realization of an optical transistor by controlling the inversion of a single molecule [165]. In their scheme the signal pulse is carefully tuned to excitation of a single dye molecule. During the excitation, the dye molecules are embedded in a so-called organic crystalline matrix. Under these conditions a single molecule's excitation can be spectrally addressed. If the molecule is in the ground state, all the incoming light is absorbed, and no signal can be detected. In the presence of a gate beam, inversion is generated and the signal beam is transmitted or even amplified. Theoretical calculations show that this effect is capable of an 85% attenuation of a focussed plane wave signal beam [166]. However, because of additional loss channels the demonstrated attenuation was only about 10%. The potential of this idea is that the effect happens on the smallest length scale (a single molecule). However, it requires extremely deep temperatures, and the switching contrast is not sufficient, even when the theoretical limit is reached. The experiment does not demonstrate a small optical power controling a bigger one of the same type. A cw laser is used to control the molecule; which limits the operational time-scale as well as the cascadabiltiy of the device.

Electromagnetically induced transparency T.J. Kippenberg's group began to realize a micro-optomechanical device in Munich, and this work is now continued in Lausanne. The setup can be seen as a strict optomechanical analogue to electromagnetically induced transparency (EIT) [167]. The control beam is tuned to a sideband-transition of a micro-optomechanical system placed inside a cavity [168], and the signal beam simply probes the transparency of the cavity. The resonance as an optomechanical form of induced transparency can be mechanically tuned to every desired wavelength. This effect can be miniaturized and mass produced. A basic transistor operation has also been demonstrated, and the usability criteria can be fulfilled. However, the response

time of this system is limited to the lifetime of the optomechanical excitation, and the energy pumped into the resonance is lost and is directly heating the system.

Optical logic gates with tapered nano-fibers E. Mazur's group at Harvard University is working on the realization of optical transistors and logic gates using tapered nano-fibers (nanowires) with sub-μm diameter [169]. From this nanowire the group constructed a Sagnac interferometer. In front of the interferometer, a second input port is created splicing two wires together [170]. The effect appears when the coupling ratio in the interferometer is other than $\rho = 0.5$, e.g., $\rho = 0.45$. Because of the unequal intensity of light propagating clock-wise and counterclock-wise in the loop, the accumulated nonlinear phase is different for each direction, and the interferometer output depends on the total input power. Defining a certain output level as *on* and another as *off*, an optical switch is realized. Even an XOR or an NOR gate can be realized in theory. Because of the very small diameter of the fiber taper reasonable nonlinear effects are already observed at a pulse energy of only a few picojoule [171] and some sub-100 fs pulse duration. An advantage of this idea is that, although the effect is happening on the few hundred nanometer length scale, the tapered fibers provide an excellent interface between the macroscopic dimensions (where the light is coupled in) and the microscopic dimensions (where the effect happens). This effect is still failing on the usability criteria: the operation point is controlled via the coupling ratio, which is not yet reproducible and can not be controlled so far. Furthermore, the logic level is not independent of loss and is not restored.

6.2 Theoretical model for a new optical transistor effect

The challenge to create a photonic transistor is that there is no strong interaction between photons as there is for electrons. As bosons photons do not interact with each other directly while they are propagating in free space. The nonlinear polarization in a medium is required to relay between the photons, c.f. Eq. 2.28. To effectively drive such a nonlinear effect requires either a high number of photons, i.e., a high intensity, or a long interaction distance. If light is propagating in a medium at two very different wavelengths, the photons are traveling with different speed, which is further reducing the probability for a nonlinear interaction between two photons via the hosting media. Also the temporal profile of a pulse propagating in a medium is not maintained, which is an essential requirement to match the fan-out criteria. The pulse at signal wavelength must propagate as a soliton in the medium and must preserve its pulse shape, i.e., it must propagate in the anomalous dispersion regime. The solution for all the above problems is to choose a medium with a dispersion profile that features the same propagation speed (v_g) for two different wavelengths, one of which is located in a negative dispersion. The numerical simulations presented in this section will examine how two such pulses are interacting inside the hosting media.

6.2.1 Two pulse interaction and the white-hole event horizon

The effect discussed in this section was recently discovered in a numerical study by Demircan and Amiranashvili [148] at the Weierstrass Institute in Berlin. In collaboration with these authors, an experiment at the Max Born Institute was performed, and new numerical simulations based on measured dispersion values were conducted and the effect is demonstrated. This section will review the numerical results of Demican and Amiranashvili [148] in context of the experiments presented in this work.

The nonlinear interaction between two copropagating pulses approaching each other is discussed. Demircan and Amiranashvili [148] are referring to this interaction as a white hole optical event horizon. The term is best explained by T. Philbin in the original Ref. [172]: *A fast river flowing out into the sea, getting slower. Waves cannot enter the river beyond the point where the flow speed exceeds the wave velocity; the river resembles an object that nothing can enter: a white hole.* This just recently rediscovered phenomenon [172], presents an unexpected analogy between nonlinear fiber optics and the trapping of light in gravitational fields, i.e, an astronomic white hole. A more direct way to understand the underlying physics is that the two pulses approach each other slowly but never pass. When the pulses are close enough, the XPM is causing a frequency shift effecting a group velocity change and locking them together in time. The pulses propagate in sync for an extended distance and exchange energy before they eventually start to separate from eachother. Due to the dramatically enlarged effective interaction length, surprising effects occur. The effect is similar to the blue-shift reported when an ultrashort laser pulse interacts with a continuous wave [172] inside a fiber. This effect was initially referred to as the fiber-optical analogue of a white-hole event horizon, because it generates a conceptually similar frequency shift as a white hole in astrophysics. Using the same analogue, the interaction between two pulses as discussed in this work happens at the so-called group velocity event horizon.

Figure 6.2 illustrates the effects observed when the two pulses approach each other in a medium. If one pulse has only a slightly higher group velocity and the faster pulse is delayed to the slower one (1), the pulses will approach each other inside the medium (2). During that approach, one pulse is propagating as a stable soliton and the other as a dispersive wave. The faster pulse will then begin to be influenced by the polarization field that the slower pulse is creating (3). The closer the two pulses are, the stronger the interaction via the nonlinear polarization field (blue shaded area). The interaction is cross-phase modulation, c.f. Sec. 2.37. Assuming the initial conditions are well chosen, this will result in a gravity-like effect and has been used in [173] to explain propagation dynamics similar to those of quantum bouncing [174]. Here the bouncing effects a reflection of the dispersive wave packet off the accelerating soliton. During this bounce the frequency of the radiation is up-shifted (4), i.e., energy is transferred from one pulse to the other. The reflection of a dispersive wave packet (control pulse) at the group-velocity horizon of a fundamental soliton (signal pulse) represents a strong light-light interaction. It will be shown that the control pulse can very efficiently modify the duration, intensity, and carrier frequency of a signal pulse.

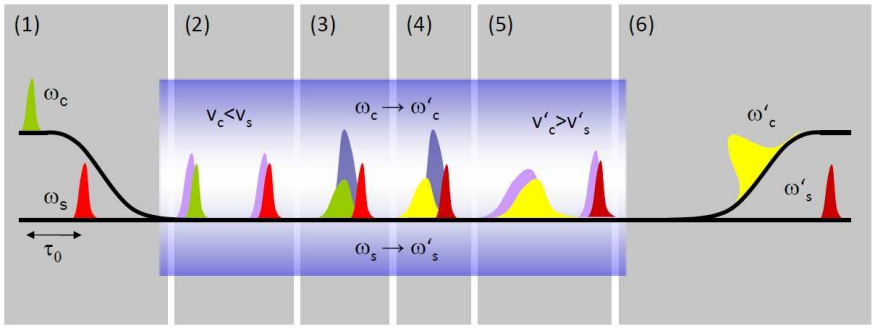

Figure 6.2: Schematic picture of the interaction of two pulses at the optical event horizon: *1.* The control pulse (ω_c, v_c) is launched after the signal pulse (ω_s, v_s) into the medium delayed by τ_0, *2.* The control pulse is slightly faster than the signal pulse; the delay is decreasing; and each pulse is creating its own polarization field (purple shade), *3.* The two pulses start to interact via the XPM effect (blue shade), *4.* Because of the interaction, the two pulses change color and velocity, *5.* the pulses now propagate interaction-free with their new velocity; the delay is increasing, and *6.* In free space the two pulses are traveling independently.

6.2.2 Numerical simulations of the two pulse interaction

The numerical simulations presented in this chapter demonstrate that the effect as discussed above is not limited to any specific kind of medium and will appear in any $\chi^{(3)}$ medium, i.e., in fibers (c.f. Sec. 2.37). The only requirements are that the dispersion profile of the medium allows a signal pulse (ω_s) and a control pulse (ω_c) to propagate with a similar group velocity and that the dispersion in the vicinity of the soliton is varying significantly. Figure 6.3 gives the dispersion as well as the group velocity of light in bulk fluoride glass as a function of of wavelength. The shown concave profile is quite common for most glasses and many other materials. The second requirement is defining pairs of suitable wavelength, e.g., in solid glass, the effect can be realized effectively only for technically difficult-to-handle wavelength pairs such as $\lambda_s \approx 3$ μm and $\lambda_c \approx 1.0 - 1.2$ μm. In the original paper, Demircan, et al. presented calculations for the fluoride glass shown in Fig 6.3. The dataset of the numerical simulations presented in the following are provided by A. Demircan and Sh. Amiranashvili. The simulations discuss two different scenarios: first, a faster control pulse and second, a slower control pulse.

The numerical model used

The optical fields handled in the discussed simulations contain considerably different frequencies ω_c and ω_s, such that the SVEA is violated (c.f. Eqn. 2.13) and a more sophisticated model needs to be used for correct numerical treatment of the propagation

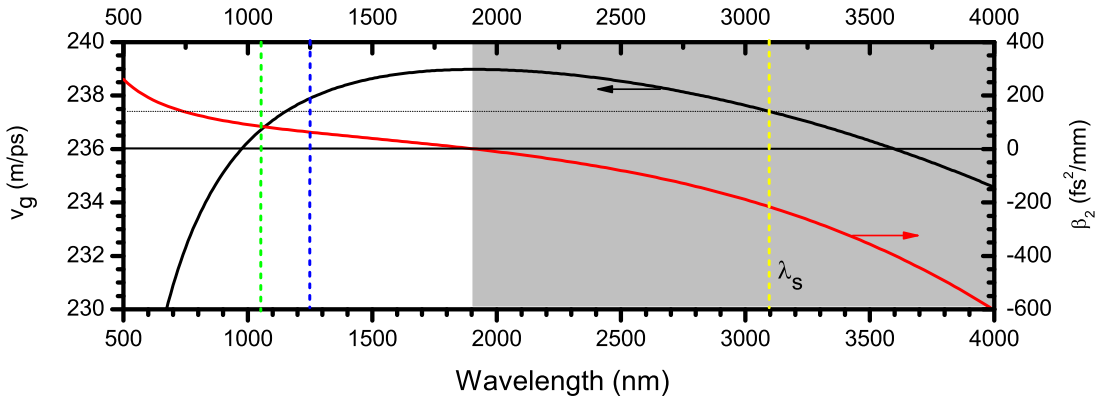

Figure 6.3: The group velocity v_g and the dispersion parameter β_2 for the fluoride glass used in the numerical simulations. The negative dispersion regime is gray shaded. The yellow dashed line gives the center wavelength of the solitonic signal pulse; the blue and green dashed lines give the center wavelengths of the slower and faster control pulses used in the experiment.

problem. A single-mode polarization-preserving waveguide is assumed, and the electric field $E(z,t)$ is written as a discrete sum in the spectral domain $E(z,t) = \sum_\omega E_\omega(z)e^{-i\omega t}$ with a real value. Here z refers to the propagation distance, and the two dependencies perpendicular to z are integrated out. In order to accurately model the propagation of ultrashort pulses, a complex valued analytic signal is introduced:

$$\mathcal{E}(z,t) = 2\sum_{\omega>0} E_\omega(z)e^{-i\omega t}. \tag{6.1}$$

As described in Eq. 2.8 this summation is carried out over spectral components with positive frequencies only. A more detailed description of the numerical model used is given in Amiranashvili et al. [175]. The propagation equation of $\mathcal{E}(z,t)$ in this model reads as

$$i\partial_z\mathcal{E}_\omega + \beta(\omega)\mathcal{E}_\omega + \frac{3\omega^2\chi}{8c^2\beta(\omega)}(|\mathcal{E}|^2\mathcal{E})_{\omega>0} = 0, \tag{6.2}$$

where parameter χ refers to the Kerr nonlinearity. If the SVEA criteria are met by the signal pulse, Eqn. 6.2 can be reduced to the nonlinear Schrödinger equation [17]. The nonlinearity parameter factors out to be $\gamma = (3\omega_s\chi)/[4\epsilon_0 c^2 n_g(\omega_s)S_{\text{eff}}]$, where S_{eff} is the effective fiber area. In order to dissect the shifting effect caused by the optical event horizon, all terms that may interfere with the scattering process at the optical event horizon are excluded from the calculation. In particular, Raman scattering is excluded, which induces the soliton self-frequency shift [27, 176] resulting in a strong influence on the soliton group velocity. This shift would interfere with the shift caused by the event horizon. Amiranashvili et al. [175] also point out that the Eqn. 6.2 is valid for a broad spectrum and avoids the use of the envelope. To model the dispersion more accurately,

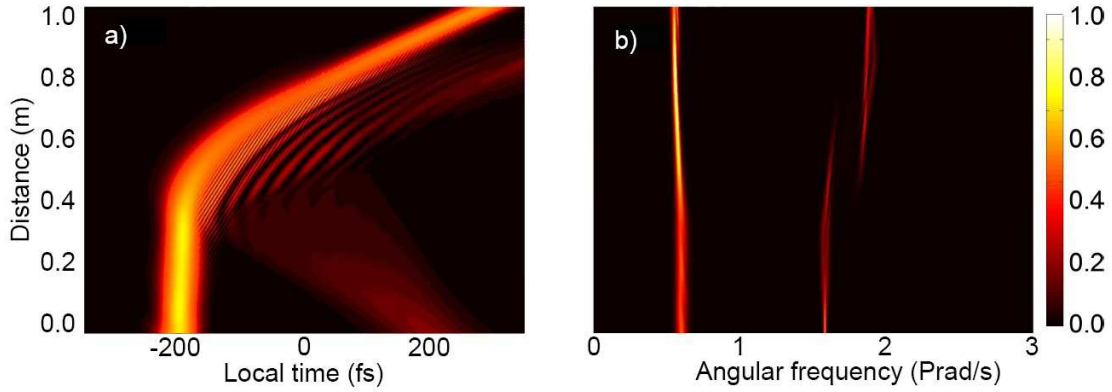

Figure 6.4: The dynamic process at the group velocity event horizon in the time (a) and spectral (b) domains. The fundamental soliton propagates with a carrier frequency of $\omega_s = 0.6\,\mathrm{Prad/s}$ and a faster control pulse at $\omega_c = 1.52\,\mathrm{Prad/s}$. This configuration represents a typical scattering process of a dispersive wave at an optical horizon of a soliton. Energy is transferred from the soliton to the dispersive wave. (Courtesy of A. Demircan)

an improved numerical description of the propagation constant $\beta(\omega)$ is used [177]. This prevents numerical stiffness in the simulations, but requires very accurate knowledge of the material's dispersion parameters.

A faster control pulse

Initially, the case of a faster control pulse slowly passing the signal soliton is simulated. According to the net-group velocity argument, the maximum effect should be observed when the following condition of the optical group-velocity horizon is fulfilled

$$\frac{c}{n_g(\omega_c)} > \frac{c}{n_g(\omega_s)} > \frac{c}{n_g(\omega_c) + \delta n}. \tag{6.3}$$

Here $n_g(\omega)$ refers to the group index, and δn is a nonlinear change of the refraction due to the presence of the strong signal pulse. Under this condition the control pulse approaches the soliton signal pulse from positive delays. At zero delay, the pulses start to overlap, and an extended XPM interaction builds up, preventing the pulses from crossing each other. Owing to this effect the two pulses will be temporally locked due to their mutual interaction. The simulations show that for a manipulation of an intense fundamental soliton by a weak control pulse, the dispersion values in the vicinity of the central frequency of the soliton have to vary significantly. To trap a weaker control pulse at the optical event horizon, the electric field intensity of the fundamental soliton has to exhibit a fast transient, which, in the experiment, is achieved by ultrashort pulse durations in the sub-100 fs regime. The calculated dynamics in both, the time and frequency domains are displayed in Fig. 6.4. For this calculation the soliton signal is injected 400 fs prior

to the control pulse. The amplitude $\mathcal{A}_c$ of the control pulse is significantly smaller than that of the signal soliton $\mathcal{A}_s$, and only the intensity-dependent refractive index change induced by the soliton is considered. A wavelength shift towards shorter wavelengths of the dispersive wave [172, 173] is observed for a frequency combination of $\omega_s = 0.6\,\mathrm{Prad/s}$ and $\omega_c = 1.52\,\mathrm{Prad/s}$ for the soliton and control pulse, respectively. The intensity of the soliton pulse is critical. It should be small and still induce a sufficient increase of the refractive index to build up a fiber-optical group velocity event horizon, involving a significant change of group velocities. In this simulation a fixed power ratio between signal and control pulse of 9 : 1 is used, and the intensity is controlled via the pulse duration. For Fig. 6.4 durations of $t_s = 21$ fs and $t_c = 70$ fs are chosen. For a medium with $\gamma = 0.1\,\mathrm{W^{-1}m^{-1}}$, this corresponds to peak powers of $P_s = 5.2\,\mathrm{kW}$ and $P_c = 0.58\,\mathrm{kW}$ for the signal pulse and the control pulse respectively. Describing the dynamics in detail, in Fig. 6.4 (a) the control pulse approaches the soliton until it reaches the trailing edge of the soliton. Then the XPM begins to induce a substantial frequency shift [178, 179] in both pulses. The central frequency of the trailing pulse is shifted to the blue and the central frequency of the leading pulse to the red [Fig. 6.4 (b)]. Instead of passing the slower signal pulse, the weak control pulse is reflected off the trailing edge of the soliton, because of the induced nonlinear refractive index change. During this reflection, both pulses are shifted in their frequency [c.f. Fig. 6.4 (b)] and consequently drift apart with their new group velocities determined by their new center frequency. The simulation reveals that the soliton signal pulse is also strongly affected by the reflection process. For a faster control pulse, the soliton is shifted towards longer wavelengths. In earlier simulations [172, 173] the red-shift of the soliton center wavelength and the change of the soliton group velocity interfered with the Raman effect. The novel shifting effect remained undiscovered. In this work the Raman effect is excluded, and the effect can be independently investigated. The wavelength shift in this calculation is understood as an energy transfer from the soliton to the control pulse during the collision. Because the control pulse is much weaker, the frequency shift of the soliton is smaller than that of the control pulse. However, the soliton center wavelength is still shifted by more than its half width, and the soliton is still propagating as a stable soliton after the reflection. This shifting effect (caused by a smaller control pulse) is an implementation of an optical transistor in close analogy to the electronic transistor described in the beginning of this section. The experiment in Sec. 6.3.3 will demonstrate this effect in a nonlinear photonic fiber.

A slower control pulse

If the signal pulse is faster than the control pulse the results change dramatically. In Fig. 6.5 the signal pulse still has the same frequency, but the control pulse is at $\omega_c = 1.8\,\mathrm{Prad/s}$. With the given dispersion profile of fluoride glass, the control pulse is now propagating slower (λ_s) than the signal soliton and needs to be injected in front of the soliton. Again, a reflection is observed (c.f. Fig. 6.5), however, this time the reflection is causing a frequency shift towards the ZDW, whereas previously the shift away from from the ZDW. The collision increases the group velocity of both pulses and energy is

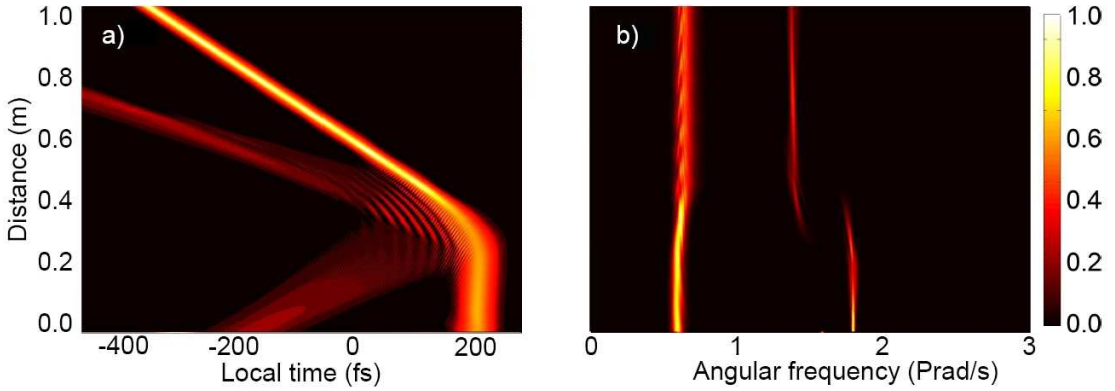

Figure 6.5: The dynamic process at the group velocity event horizon in the time (a) and spectral (b) domains. The fundamental soliton propagates with a carrier frequency of $\omega_s = 0.6\,\mathrm{Prad/s}$ and a slower control pulse at $\omega_c = 1.8\,\mathrm{Prad/s}$. This configuration represents a scattering process with a transfer of energy from the dispersive wave to the soliton. (Courtesy of A. Demircan)

transferred from the control pulse to the soliton. In particular, the frequency shifts are: $\omega_c = 1.8$ Prad/s $\rightarrow 1.45$ Prad/s and $\omega_s = 0.6$ Prad/s $\rightarrow 0.62$ Prad/s. An interesting feature of this particular type of interaction is the change in the soliton duration and peak power. After the reflection, the soliton is compressed to only 11 fs and has doubled its initial peak power. This significant change is caused by the strong dispersion value variation in the range of induced frequency shift. The compression mechanism is similar to soliton compression in a dispersion decreasing fiber, where the soliton adiabatically changes its shape due to the change of β_2 [17]. Theoretically the compression rate can be controlled by the control pulse intensity. However, changes of the control pulse parameters are always limited by the requirement to enable the scattering process at the optical event horizon. Consequently, with increasing control pulse energy, the control pulse will eventually only be partially reflected at the horizon, with the remaining part tunneling through.

Conclusions of the numerical simulations

The scattering of an optical pulse at an optical event horizon enables control of the properties of a strong signal light pulse with another weaker control light pulse without destroying the temporal structure of the signal light pulse. A careful, but still not critical selection of the center wavelengths (the group velocities) of the pulses allows for a control of the interaction in such a way the center wavelengths either strongly repel or attract each other. The resulting mutually induced shifts are perfectly efficient and can be used to create an optical transistor. The simulations demonstrate that even a 9 times weaker control pulse can switch a signal pulse in a non-ambiguous way. Such behavior has never been observed in any other previously proposed optical transistors.

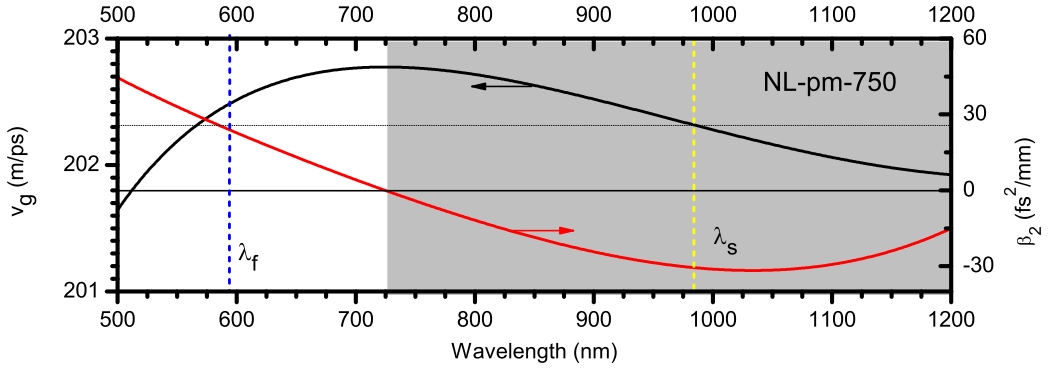

Figure 6.6: The group velocity v_g and the dispersion parameter β_2 for the polarization maintaining fiber NL-PM-750 [180] used in the experiments. The dispersion negative dispersion regime is gray shaded. The dashed lines give the center wavelengths of the two pulses used in the experiment.

The solitonic switching scheme is cascadable and therefore fulfills the two most stringent criteria for an optical transistor, i.e., fan out and cascadability. It is known that a non-exact fundamental soliton is changed into an exact soliton while propagating in a fiber. A degradation of the signal from an exact fundamental soliton can thereby amount up to 50% [17] (logic level restoration). Input and output pulses are separated, as they can here easily be filtered out spectrally (input/output isolation). The effect only requires the presence of a Kerr nonlinearity and a concave group delay $\beta_1(\omega)$, cf. Fig. 6.3, in a reasonably long waveguide. The engineering of the waveguide will allow to shift the soliton frequency into the more practical telecommunications range. Eventually this effect can even be implemented on an optical waveguide chip.

6.3 Experimental demonstration in a photonic crystal fiber

This section presents the experimental demonstration of the optical transistor implemented in a photonic crystal fiber. The use of this fiber allows to performing the experiment at about 600 nm (control pulse/ yellow pulse) and 1 μm (signal pulse/ red pulse). The experiment shows that the interaction of the two pulses at the optical event horizon results in a significant wavelength shift of both, the signal and the control pulses. While both shifts are of significant academic interest the shift of the red signal pulse, which is a soliton, is fulfilling all criteria for an optical transistor, and therefore, is of major importance for future applications. Implementation in a fiber is chosen because a fiber allows extended copropagation while confining the light to a very small core and maintaining a high intensity simultaneously. This is enhancing the nonlinear interaction between the pulses. Additionally, the dispersion of such a fiber is flexible and can be controlled by the geometrical parameters of the fiber's microstructure [135, 181] during the drawing process. A suitable dispersion profile (Fig. 6.6) is found for many commercial PCFs that were originally developed for supercontinuum generation [180, 182, 183] and for

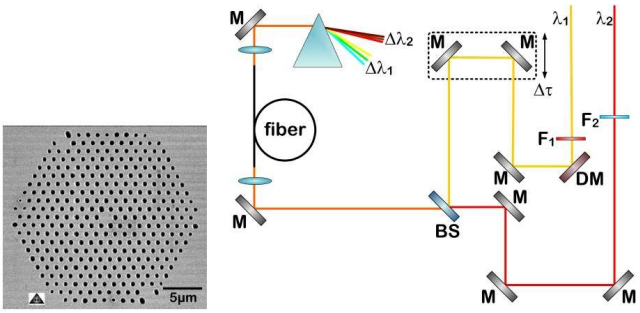

Figure 6.7: *Left:* SEM micrograph of the used fiber. *Right:* The setup of the experiment. Mirrors (M), a beamsplitter (BS), a dichroic mirror (DM), color glass filters (F), and lenses (L) are used to delay ($\Delta\tau$), to recombine, and to couple the yellow (λ_1) and red (λ_2) pulses into the fiber. Behind the fiber a spectrometer is used to measure the wavelength shift $\Delta\lambda$ of the pulses. This is illustrated here by a prism.

various signal and control wavelength combinations. The fiber used in the experiment was chosen because both the signal as well as the control wavelength can be detected with a compact CCD-based spectrometer, and the wavelengths can be generated with commercial lasers available at the Max Born Institute.

6.3.1 Setup of the experiment

A measurement and subsequent analysis of the dispersion properties revealed that the NL-PM-750 [180] fiber is well suited to demonstrate the effect at $\lambda_c = 580\,\text{nm}$ and $\lambda_s = 980\,\text{nm}$. The dispersion of this fiber is measured from 500 nm to 1.5 μm. The measurement confirmed the position of the two zero dispersion wavelengths, and allowed for a precise determination of the parameters for a broadband dispersion model [177]. The chosen wavelengths support the scenario of a slightly faster propagating control pulse, which has been numerically discussed above. To generate the pair of ultrashort laser pulses, an optical parametric amplifier (OPA) system is used. This laser system has two parametric units (TOPAS, Spectra Physics), both pumped at 800 nm by the same 45 fs pump pulse (Spitfire Pro, Spectra Physics) at a repetition rate of 1 kHz. With this system two independently tunable and perfectly synchronized laser pulses are generated (the signal pulse is an idler pulse of a parametric process, and the control pulse is a signal component of another parametric process), but both pulses have the same polarization when entering the experiment. Assuming that the generated pulses are bandwidth limited, a pulse duration of about 40 to 50 fs is calculated. Figure 6.7 illustrates the setup of the experiment and shows a micrograph of the fiber. The initial delay τ_0 between the two pulses can be controlled by the delay stage, and its position is measured with a digital micrometer screw gauge with an error of $\pm 0.001\,\text{mm}$. The initial zero delay point is precisely determined with a cross-correlation measurement. After the control pulse is delayed, the two beams are collinearly combined and are

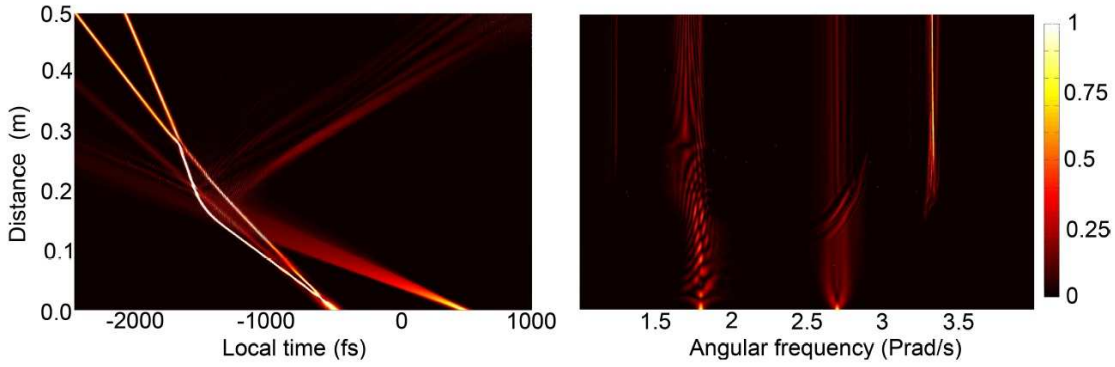

Figure 6.8: The dynamic process at the group velocity event horizon in the time (a) and spectral (b) domains. The initial delay between the pulses is 1 ps, the signal frequency is $\omega_s = 0.6\,\mathrm{Prad/s}$, and the control pulse frequency is $\omega_c = 1.52\,\mathrm{Prad/s}$, i.e., the control pulse is slightly faster.

coupled into a 49.5 cm long fiber using a lens with $f = 3.6\,\mathrm{mm}$. The fiber output is characterized with a compact CCD based spectrometer (Avantes, AvaSpec-3648 [184]). This spectrometer covers a range from 495 to 1024 nm with a resolution of 0.14 nm/pixel. Given the spectrally dependent quantum efficiency of the uncalibrated CCD sensor, all measured spectra are only of qualitative nature.

6.3.2 Numerical simulation of the experiment

To identify the relevant physical effects, a numerical simulation of the propagation in the fiber is performed, based on the dispersion model and the pulse parameters used in the experiment. As a typical example, the results for an initial delay of $\tau_0 = 1\,\mathrm{ps}$ are presented in Fig. 6.8. In comparison to the simulations in Sec. 6.2.2 and Fig. 6.4, this new simulation shows, with some minor deviations, the same characteristic features as in fluoride glass [148] with a faster control pulse. The most obvious deviation is found in the temporal domain where the signal pulse splits into two solitons immediately after entering the fiber. A closer look into the spectral domain (right side) reveals that these two solitons are separated in the spectral domain. Because of this separation, the soliton with the shorter wavelength is faster than the other, and the control pulse is only affected by the slower soliton (longer center-wavelength). During the interaction with the slower soliton, energy is transferred from the signal pulse to the control pulse. This causes a strong wavelength shift of the dispersive control pulse into the blue direction and a smaller shift of the soliton into the red direction.

Since neither the spectrum nor the temporal pulse profile can be measured inside the fiber, this simulation needs to be repeated for different initial delays between the pulses, and only the output spectrum is of experimental importance. In Fig.6.9 these calculated output spectra are plotted for different delays between the input pulses. At negative delays the control pulse is coupled into the fiber in front of the signal pulse and there

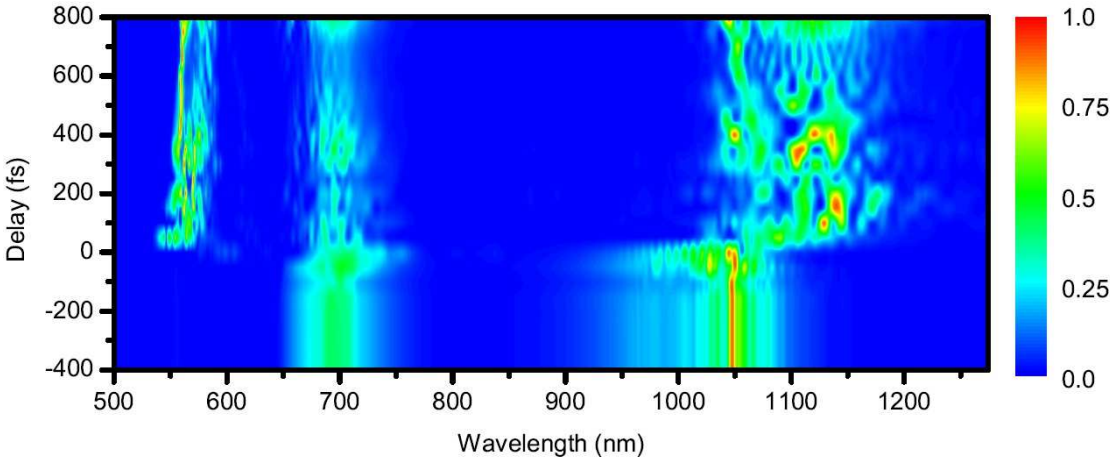

Figure 6.9: Calculated spectral intensity distribution for different delays. The input wavelengths are $\lambda_1 = 700\,\text{nm}$ and $\lambda_2 = 1050\,\text{nm}$.

will be no interaction, since even the faster of the two solitons is still slower than the control pulse [c.f. Fig. 6.8 (left)]. At zero delay the two pulses start to interact in the fiber, and wavelength shifts in the output-spectrum are observed.

6.3.3 Experimental results

In the experiment the output spectra for different delays between the input pulses are recorded and normalized. Figure 6.10 represents the typical results of such a measurement with input pulse energies of $P_\text{s} = 0.71\,\text{nJ}$ and $P_\text{c} = 0.19\,\text{nJ}$, i.e., a power level ratio of about $4:1$. At negative delays no nonlinear interaction between the two pulses is possible. Still, the control pulse shows pronounced spectral distortions, stemming from a combination of self-phase modulation and normal dispersion [17]. These distortions are verified in the simulations. In contrast to the control pulse, the signal pulse maintains its single-peaked spectral shape, the negative dispersion, and the resulting solitonic propagation. When the two pulses are launched into the fiber in close temporal proximity, a mutual interaction is observed, which gives rise to wavelength shifts up to 80 nm. Figure 6.10 is recorded in one continuous scan. Since the sensitivity of the CCD is much smaller for longer wavelengths, the shift of the signal pulse is barely visible and cannot be clearly identified in this figure. To quantify the redshift of the signal pulse the measurement is repeated at specific delays, with a 10 times longer exposure time as well as twice the number of averages. Figure 6.11 (right) shows the recorded spectra for the signal pulse, allowing for a more detailed inspection of the wavelength shift of the signal and control pulse. The data of the control pulse plotted in Fig. 6.11 (left) is measured with the same settings used for the scan in Fig. 6.10.

The effect of the strong red pulse on the weaker yellow one is particularly dramatic, in such a way that even very coarse wavelength filtering would lead to nearly 100%

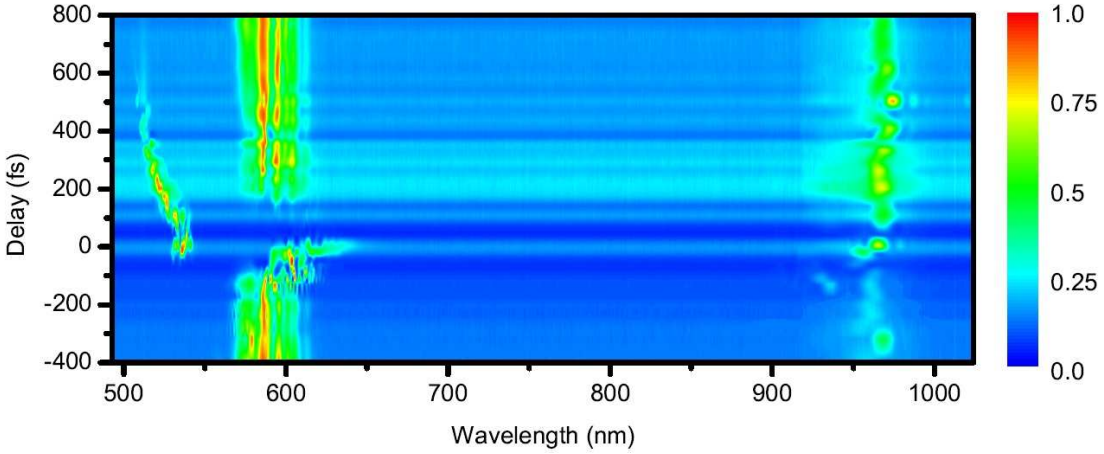

Figure 6.10: Measured spectral intensity distribution for different delays. The input wavelengths are $\lambda_1 = 680\,\text{nm}$ and $\lambda_2 = 980\,\text{nm}$.

switching contrast. However, the adverse yet much weaker action of the yellow pulse acting on the center wavelength of the soliton is even more interesting. For the first time ever, this shift fullfills all criteria for an optical transistor listed above. With the chosen pulse energy ratio, the observed shift of about 10 nm of the strong pulse is on the same order as the spectral width of the soliton itself.

The results for the experiment in Fig. 6.10 do agree qualitatively with the results of the numerical simulations in Fig. 6.9. All important features of the experimental trace can also be found in the simulation. It is important to note that the simulations are assuming slightly different wavelengths than later realized in the experiment, i.e., a different group velocity for the signal pulse was used. The remaining difference between the calculation and the experiment is explained by additional effects that are causing a different group velocity by shifting the center wavelengths or that are affecting the dispersion directly. Possible effects are the Raman self-frequency shift [17], a change of the (polarization) group velocity based on a combination of Kerr-nonlinearity, polarization effects [185], and a change of the group velocity dispersion caused by the solitonic propagation [186].

Robustness of the effect

The shift of the soliton center wavelength, here discussed as an optical transistor, must be robust against changes in pulse energy and uncritical in terms of timing between the two pulses, c.f. Sec. 6.1.1. The first issue is addressed in an experiment where the energy of the red pulse was varied from 0 (no pulse) to 0.37 nJ while the energy of the yellow pulse was kept constant at 0.72 nJ. Since the wavelength shift of the yellow pulse is proportional to the energy transfer during the reflection process, this shift is used as an indicator for the strength of the nonlinear interaction between the pulses. The results of this measurement are shown in Fig. 6.12. All spectra are recorded for a fixed

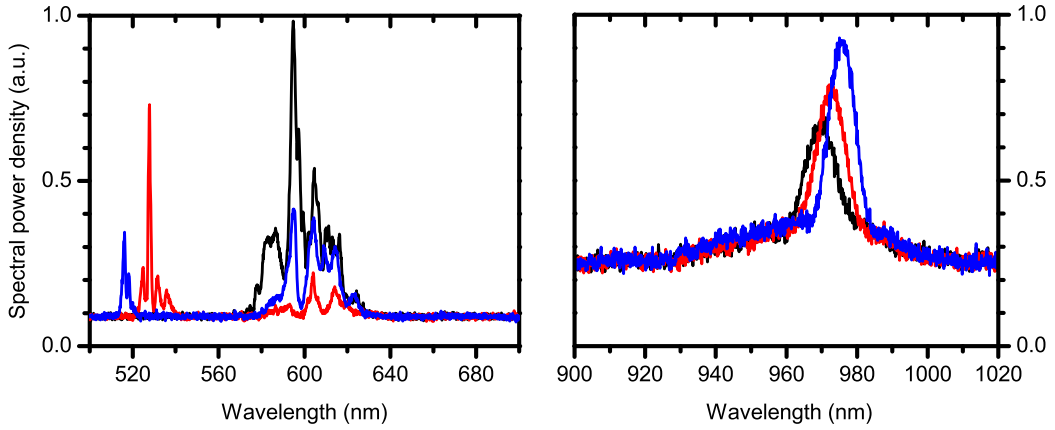

Figure 6.11: Selected spectra of the control (left) and signal (right) pulse at a delay τ_0 of -52 fs (black line), 72 fs (red line), and 114 fs (blue line).

delay of approximately 75 fs. The orange line in the back shows the output spectrum of only the yellow pulse propagating in the fiber; the spectrum is modulated by SPM, and dispersion effects are discussed above. The other spectra are recorded at different input power levels. The power is increasing from the back to the front. It is observed that an increasing amount of power is transfered by the reflection into the wavelength split component of the yellow pulse. This means that less power of the yellow pulse is tunneling trough the event horizon when the power of the red pulse is increased. The first shifting is observed between 0.12 and 0.21 nJ, that is exactly the amount of power used in the experiments of Sec. 6.3.3. The complete pulse is already reflected at an energy of 0.37 nJ (a power level ratio of 1:2). From this point on the reflection is not critical, and the magnitude of the wavelength shift only depends on the power level ratio. This measurement validates that if the signal pulse is stronger than the control pulse, then there is absolutely no critical bias.

The robustness in terms of timing is observed in the measured data (Fig. 6.10) as well as in the numerical simulation (Fig. 6.9). Both data sets indicate a critical delay of about ± 20 fs at zero delay, i.e., the half width of the initial pulses. This is explained by the existing temporal overlap of the pulses at injection. The portion of pulse intensity contained in the overlap cannot contribute to the nonlinear interaction and is lost; the optical event horizon is not created. As soon as there is no longer any significant temporal overlap between the pulses, the shift becomes stable and uncritical, i.e., virtually the same shift is observed for all delays.

6.4 Conclusions and outlook

The experiments presented in this section demonstrated a new concept for a fully functional optical transistor. The effect was experimentally demonstrated in a commercial photonic crystal fiber at a wavelength of 980 nm for a power ratio of 3.7 : 1 between the

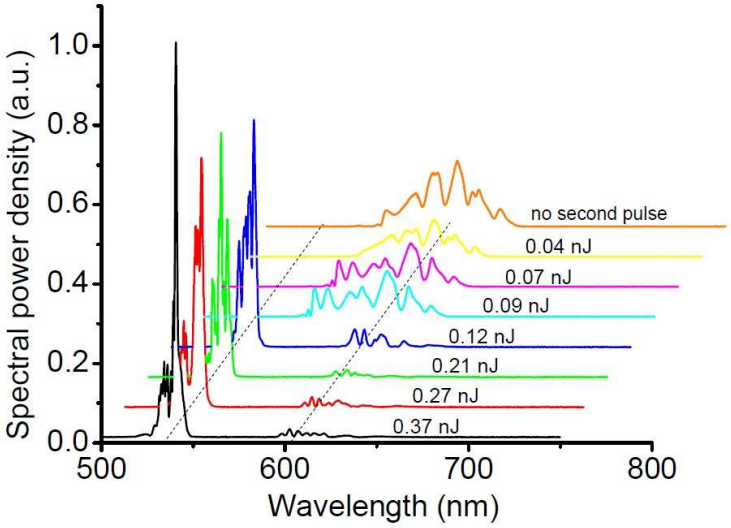

Figure 6.12: Measured output spectra of the yellow pulse for different input power at the red pulse, measured at a fixed delay of 75 fs. The power of the red pulse is increasing from the back to the front.

signal and the control pulse. Shifts of 80 nm for the dispersive wave and more than the spectral half width of the signal soliton were observed. The effect has been proven to be robust and not critical. In contrast to previous switching schemes, this effect does not rely on an enhanced nonlinearity but on an optimized dispersion. This is easier to realize and is more reliable. The numerical simulations agree well with experimental data and indicate that an even stronger effect could be observed in other materials. However, for most of these materials the signal wavelength is located in a technically challenging region.

In a future experiment the source must be improved. A source with MHz repetition rate will be beneficial for detection purposes and allow for a temporal characterization of the output pulses. An all-fiber setup would be a first step towards a practical implementation as optical logic unit. However, the propagation of ultrashort pulses in fiber is critical. In a next step the opportunities must be explored how this effect can be implemented in materials other than glass, e.g., in optical semiconductor waveguides written on a chip.

7 Conclusion and outlook

This work introduced novel fiber designs to control the dispersion and nonlinearity in photonic fibers. Several effects were pushed beyond the generally accepted borders of fiber optics. These demonstrations reach from unprecedented avoidance of linear and nonlinear optical effects to the very opposite, i.e., a dramatic increase of nonlinear effects for supercontinuum generation and optical switching, enabling novel applications that were previously considered impossible.

The chirped fiber

The first fiber design discussed was a hollow core fiber with a radially chirped microstructured cladding. It has been theoretically shown and experimentally demonstrated that the chirp significantly reduces the dispersion in a broad spectral range. The physical mechanisms behind the high-fidelity guiding mechanisms were explored and modeled in great detail, revealing the key function of the innermost cladding layer together with the absence of resonantly enhanced guiding in the outer layers of the photonic cladding. These new fibers are ideal for the delivery of ultrashort laser pulses. Pulses as short as 25 fs were delivered over a 1 meter distance without any compensation. Notably, employing a compensation scheme allowed even the delivery of sub-20-fs pulses. While this guiding mechanism so far limited losses to a few dB/m, such value already opens a perspective for the fiber-based delivery of 20-fs pulses in medical diagnostics and for biological applications that were previously considered impossible. All important fiber parameters are identified and a further optimization for any desired wavelength is possible. A genetic algorithm will work best to optimize an existing fiber layout.

The fiber with a liquid core

In a second experiment, the highly important mechanism of soliton induced supercontinuum generation was investigated and scaled to a new regime of 390 nJ pulse energies, using a water-filled hollow-core fiber. Other than simple white-light generation in bulk or liquid media, soliton induced supercontinuum generation enables to reach much wider bandwidths, as it exploits a combination of linear and nonlinear processes to quickly expand the spectrum beyond the optical octave. A two octave spanning supercontinuum was demonstrated and numerical simulations identified the underlying mechanism. This supercontinuum has about 10 times more energy than any comparable previously generated supercontinuum in a conventional fiber. Further scaling of the pulse energy is possible, since the liquid core concept does not suffer damage limitations and the liquid can be easily replaced, even before the next pulse. A continuous flow of the liquid will cool the glass structure and will allow for much higher average power levels. This fiber

with a liquid core is an ideal medium for nonlinear optical applications of supercontinua, where otherwise the relatively small peak powers appear as a bottleneck for further optical processing.

Two pulse interaction

Finally, a novel concept for building an optical transistor was experimentally demonstrated. This concept is based on the enhancing the nonlinear interaction between two optical pulses in a significant way, such that for the first time it was possible to switch a strong optical pulse with weaker control pulse. Moreover, the concept fulfills an arduous set of other criteria, including fan-out and cascadability that so far only very few claimed optical transistors have been found to comply with. The demonstrated effect results in a significant frequency shift of both pulses. The effect is demonstrated in a fiber, but is not limited to this photonic system. Other than in earlier approaches the effect does not require an enhanced nonlinearity; the key parameter is the dispersion. The effect can be implemented in many materials; the most fascinating idea is miniaturization to an optical transistor on a chip. This will lead to integrated optical logic and ultrafast optical switches. The delay dependence of the effect can be utilized to tune a strong laser pulse with a weaker one. Other optical analoga to electronic devices will now be built, e.g., an optical operational amplifiers.

Closing remarks

These results have created a significant shift in the conceptualization and experimental use of photonic crystal fibers and revolutionized the approach to all-optical transistors. Practical applications, previously unimaginable, are now within reach. Further research and development of these topics will turn flexible delivery fantasies into realities and unlock the door to a brave new world of optical logic.

List of acronyms

AC	autocorrelation
CPCF	chirped photonic crystal fiber
DFWM	degenerate four-wave mixing
DOS	density of optical states
FEM	finite element method
FWM	four-wave mixing
GD	group delay
GDD	group delay dispersion
GVD	group velocity dispersion
HCF	hollow core fibers
IAC	interferometric autocorrelation
LMA	large mode area (fiber)
NLS	nonlinear Schrödinger equation
NSR	non-solitonic radiation
PCF	photonic crystal fiber
RAM	random access memory
SC	supercontinuum
SPM	self phase modulation
SVEA	slowly-varying envelope approximation
TOD	third order dispersion
XPM	cross-phase modulation
ZDW	zero dispersion wavelength

Bibliography

[1] A. G. Bell; *On the Production and Reproduction of Sound by Light: the Photophone*; American Association for the Advancement of Science, Proceedings of **29**, 115 (1880).

[2] D. Colladon; *On the reflections of a ray of light inside a parabolic liquid stream*; Comptes Rendus **15**, 800 (1842).

[3] B. I. Hirschowitz, L. E. Curtiss, C. W. Peters, and H. M. Pollard; *Demonstration of a new gastroscope, the fiberscope*; Gastroenterology **35**, 50 (1958).

[4] C. K. Kao and G. A. Hockham; *Dielectric-fibre Surface Waveguides for Optical Frequencies*; Proceedings of the IEE **113**, 1151 (1966).

[5] C. K. Kao; *Nobel Lecture: Sand from centuries past: Send future voices fast*; Rev. Mod. Phys. **82**, 2299 (2010).

[6] W. Boyle and G. E. Smith; *Charge Coupled Semiconductor Devices*; Bell Sys. Tech. J **49**, 587 (1970).

[7] Nobelprize.org; *The Nobel Prize in Physics 2009*; The Official Web Site of the Nobel Prize: `http://nobelprize.org/nobel_prizes/physics/laureates/2009/` (2011).

[8] D. Qian, M. F. Huang, E. Ip, Y. K. Huang, Y. Shao, J. Hu, and T. Wang; *101.7-Tb/s PDM-128QAM - OFDM transmission over 3×55-km SSMF using pilot-based phase noise mitigation*; in *OFC-NFOEC 2011*; PDPB5 (2011).

[9] P. Russell; *Photonic Crystal Fibers*; Science **299**, 358 (2003).

[10] J. Maxwell; *On Physical Lines of Force*; Philosophical Magazine and Journal of Science **25**, 161 (1861).

[11] M. Born and E. Wolf; *Principles of optics.*; 7th edition (Cambridge University Press, Cambridge, 1999).

[12] J.-C. Diels and W. Rudolph; *Ultrashort Laser Pulse Phenomena* (Academic Press, San Diego, 1996).

[13] A. Yariv and P. Yeh; *Optical waves in crystals*; 2nd edition (John Wiley & Sons, Hoboken, 1984).

[14] T. Brabec and F. Krausz; *Nonlinear Optical Pulse Propagation in the Single-Cycle Regime*; Phys. Rev. Lett. **78**, 3282 (1997).

[15] M. A. Porras; *Propagation of single-cycle pulsed light beams in dispersive media*; Phys. Rev. A **60**, 5069 (1999).

[16] P. Kinsler and G. H. C. New; *Few-cycle pulse propagation*; Phys. Rev. A **67**, 023813 (2003).

[17] G. P. Agrawal; *Nonlinear Fiber Optics*; 3rd edition (Academic Press, San Diego, 2003).

[18] D. C. Hutchings, M. Sheik-Bahae, D. J. Hagan, and E. W. Van Stryland; *Kramers-Krönig relations in nonlinear optics*; Optical and Quantum Electronics **24**, 1 (1992).

[19] J. D. Jackson; *Classical Electrodynamics*; 2nd edition (John Wiley & Sons, New York, 1975).

[20] I. H. Malitson; *Interspecimen Comparison of the Refractive Index of Fused Silica*; J. Opt. Soc. Am. **55**, 1205 (1965).

[21] Schott North America Inc.; *Optical Glass Catalogue*; SCHOTT North America, Inc., 555 Taxter Road, Elmsford, NY 10523, USA, and online: `http://www.us.schott.com` (2011).

[22] W. Sellmeier; Ann. Physik. Chem **143**, 271 (1871).

[23] R. W. Boyd; *Nonlinear Optics*; 2nd edition (Academic Press, London, 2003).

[24] G. Boyd and A. Kleinman; *Parametric interaction of focused Gaussian light beams*; J. App. Phys. **39**, 3597 (1968).

[25] F. Shimizu; *Frequency Broadening in Liquids by a Short Light Pulse*; Phys. Rev. Lett. **19**, 1097 (1967).

[26] R. H. Stolen and C. Lin; *Self-phase-modulation in silica optical fibers*; Phys. Rev. A **17**, 1448 (1978).

[27] R. H. Stolen, J. P. Gordon, W. J. Tomlinson, and H. A. Haus; *Raman response function of silica-core fibers*; J. Opt. Soc. Am. B **6**, 1159 (1989).

[28] S. V. Chernikov and P. V. Mamyshev; *Femtosecond soliton propagation in fibers with slowly decreasing dispersion*; J. Opt. Soc. Am. B **8**, 1633 (1991).

[29] P. V. Mamyshev and S. V. Chernikov; *Ultrashort-pulse propagation in optical fibers*; Opt. Lett. **15**, 1076 (1990).

[30] Q. Lin and G. Agrawal; *An accurate model for the Raman response function in silica fibers*; in *Lasers and Electro-Optics, Quantum Electronics and Laser Science Conference. CLEO/QELS 2006*; CMW5 (2006).

[31] S. Blair and K. Wagner; *(2+1)-D propagation of spatio-temporal solitary waves including higher-order corrections*; Optical and Quantum Electronics **30**, 697 (1998).

[32] A. L. Gaeta; *Catastrophic Collapse of Ultrashort Pulses*; Phys. Rev. Lett. **84**, 3582 (2000).

[33] B. Kibler, J. M. Dudley, and S. Coen; *Supercontinuum generation and nonlinear pulse propagation in photonic crystal fiber: influence of the frequency-dependent effective mode area*; Appl. Phys. B **81**, 337 (2005).

[34] J. K. Ranka, R. S. Windeler, and A. J. Stentz; *Visible continuum generation in air-silica microstructure optical fibers with anomalous dispersion at 800 nm*; Opt. Lett. **25**, 25 (2000).

[35] A. V. Husakou and J. Herrmann; *Supercontinuum Generation of Higher-Order Solitons by Fission in Photonic Crystal Fibers*; Phys. Rev. Lett. **87**, 203901 (2001).

[36] J. Herrmann, U. Griebner, N. Zhavoronkov, A. Husakou, D. Nickel, J. C. Knight, W. J. Wadsworth, P. S. J. Russell, and G. Korn; *Experimental Evidence for Supercontinuum Generation by Fission of Higher-Order Solitons in Photonic Fibers*; Phys. Rev. Lett. **88**, 173901 (2002).

[37] Y. Kodama and A. Hasegawa; *Nonlinear pulse propagation in a monomode dielectric guide*; IEEE Journal of Quantum Electronics **23**, 510 (1987).

[38] P. K. A. Wai, C. R. Menyuk, H. H. Chen, and Y. C. Lee; *Soliton at the zero-group-dispersion wavelength of a single-mode fiber*; Opt. Lett. **12**, 628 (1987).

[39] N. Akhmediev and M. Karlsson; *Cherenkov radiation emitted by solitons in optical fibers*; Phys. Rev. A **51**, 2602 (1995).

[40] J. N. Elgin, T. Brabec, and S. M. J. Kelly; *A perturbative theory of soliton propagation in the presence of third order dispersion*; Opt. Commun. **114**, 321 (1995).

[41] P. V. Kaiser and H. W. Astle; *Low-loss single-material fibers made from pure silica*; Bell Syst. Tech. J. **53**, 1021 (1974).

[42] J. C. Knight, T. A. Birks, P. S. J. Russell, and D. M. Atkin; *All-silica single-mode optical fiber with photonic crystal cladding*; Opt. Lett. **21**, 1547 (1996).

[43] P. Russell; *Photonic-Crystal Fibers*; J. Lightwave Technol. **24**, 4729 (2006).

[44] F. Benabid, F. Couny, P. Light, and P. J. Roberts; *Photonic-Crystal Fibers: Hollow-core PCFs enable high nonlinearity at low light levels*; Laser Focus World **44** (2008).

[45] J. D. Joannopoulos, R. D. Meade, and J. N. Winn; *Photonic Crystals: Molding the Flow of Light*; 2nd edition (Princeton University Press, Princeton, 2008).

[46] W. Reeves, J. Knight, P. Russell, and P. Roberts; *Demonstration of ultra-flattened dispersion in photonic crystal fibers*; Opt. Express **10**, 609 (2002).

[47] C. M. Smith, N. Venkataraman, M. T. Gallagher, D. Muller, J. A. West, N. F. Borrelli, D. C. Allan, and K. W. Koch; *Low-loss hollow-core silica/air photonic bandgap fibre*; Nature **424**, 657 (2003).

[48] F. Couny, F. Benabid, P. J. Roberts, P. S. Light, and M. G. Raymer; *Generation and Photonic Guidance of Multi-Octave Optical-Frequency Combs*; Science **318**, 1118 (2007).

[49] S.-J. Im, A. Husakou, and J. Herrmann; *Guiding properties and dispersion control of kagome lattice hollow-core photonic crystal fibers*; Opt. Express **17**, 13050 (2009).

[50] J. S. Skibina, R. Iliew, J. Bethge, M. Bock, D. Fischer, V. I. Beloglasov, R. Wedell, and G. Steinmeyer; *A chirped photonic-crystal fibre*; Nat. Photon. **2**, 679 (2008).

[51] R. Paschotta; *Encyclopedia of Laser Physics and Technology*; 1st edition (Wiley-VCH, Weinheim, 2008).

[52] E. R. Peck and K. Reeder; *Dispersion of Air*; J. Opt. Soc. Am. **62**, 958 (1972).

[53] C. Mahnke and F. Mitschke; *A useful approximation for the cladding index of holey fibers*; Appl. Phys. B **99**, 241 (2010).

[54] G. Sansone, G. Steinmeyer, C. Vozzi, S. Stagira, M. Nisoli, S. De Silvestri, K. Starke, D. Ristau, B. Schenkel, J. Biegert, A. Gosteva, and U. Keller; *Mirror dispersion control of a hollow fiber supercontinuum*; Appl. Phys. B **78**, 551 (2004).

[55] B. Schenkel, R. Paschotta, and U. Keller; *Pulse compression with supercontinuum generation in microstructure fibers*; J. Opt. Soc. Am. B **22**, 687 (2005).

[56] M. Zavelani-Rossi, G. Cerullo, S. De Silvestri, L. Gallmann, N. Matuschek, G. Steinmeyer, U. Keller, G. Angelow, V. Scheuer, and T. Tschudi; *Pulse compression over a 170-THz bandwidth in the visible by use of only chirped mirrors*; Opt. Lett. **26**, 1155 (2001).

[57] A. Baltuška, T. Fuji, and T. Kobayashi; *Visible pulse compression to 4 fs by optical parametric amplification and programmable dispersion control*; Opt. Lett. **27**, 306 (2002).

[58] M. Nisoli, S. De Silvestri, O. Svelto, R. Szipöcs, K. Ferencz, C. Spielmann, S. Sartania, and F. Krausz; *Compression of high-energy laser pulses below 5 fs*; Opt. Lett. **22**, 522 (1997).

[59] A. Gosteva, M. Haiml, R. Paschotta, and U. Keller; *Noise-related resolution limit of dispersion measurements with white-light interferometers*; J. Opt. Soc. Am. B **22**, 1868 (2005).

[60] L. Cohen; *Comparison of single-mode fiber dispersion measurement techniques*; J. Lightwave Technol. **3**, 958 (1985).

[61] S. Diddams and J.-C. Diels; *Dispersion measurements with white-light interferometry*; J. Opt. Soc. Am. B **13**, 1120 (1996).

[62] F. Reynaud, F. Salin, and A. Barthélemy; *Measurement of phase shifts introduced by nonlinear optical phenomena on subpicosecond pulses*; Opt. Lett. **14**, 275 (1989).

[63] P. Hlubina, M. Szpulak, D. Ciprian, T. Martynkien, and W. Urbanczyk; *Measurement of the group dispersion of the fundamental mode of holey fiber by white-light spectral interferometry*; Opt. Express **15**, 11073 (2007).

[64] M. Takeda, H. Ina, and S. Kobayashi; *Fourier-transform method of fringe-pattern analysis for computer-based topography and interferometry*; J. Opt. Soc. Am. **72**, 156 (1982).

[65] J. Bethge and G. Steinmeyer; *Numerical fringe pattern demodulation strategies in interferometry*; Rev. Sci. Instrum. **79**, 073102 (2008).

[66] G. Stibenz, C. Ropers, C. Lienau, C. Warmuth, A. Wyatt, I. Walmsley, and G. Steinmeyer; *Advanced methods for the characterization of few-cycle light pulses: a comparison*; Appl. Phys. B **83**, 511 (2006).

[67] T. Le, J. Bethge, J. Skibina, and G. Steinmeyer; *Hollow fiber for flexible sub-20-fs pulse delivery*; Opt. Lett. **36**, 442 (2011).

[68] A. Härkönen, J. Paajaste, S. Suomalainen, J.-P. Alanko, C. Grebing, R. Koskinen, G. Steinmeyer, and M. Guina; *Picosecond passively mode-locked GaSb-based semiconductor disk laser operating at 2 μm*; Opt. Lett. **35**, 4090 (2010).

[69] G. Krauss, S. Lohss, T. Hanke, A. Sell, S. Eggert, R. Huber, and A. Leitenstorfer; *Synthesis of a single cycle of light with compact erbium-doped fibre technology*; Nat. Photon. **4**, 33 (2010).

[70] J. W. Nicholson, J. Jasapara, W. Rudolph, F. G. Omenetto, and A. J. Taylor; *Full-field characterization of femtosecond pulses by spectrum and cross-correlation measurements*; Opt. Lett. **24**, 1774 (1999).

[71] S. De Silvestri, M. Nisoli, G. Sansone, S. Stagira, and O. Svelto; *Few-Cycle Laser Pulse Generation and its Applications*; volume 95 of *Topics in Applied Physics* (Springer, Berlin, 2004).

[72] J. Pomplun, L. Zschiedrich, R. Klose, F. Schmidt, and S. Burger; *Finite element simulation of radiation losses in photonic crystal fibers*; phys. stat. sol. (a) **204**, 3822 (2007).

[73] P. Monk; *Finite Element Methods for Maxwell's Equations* (Oxford University Press, Oxford, 2003).

[74] A. Cucinotta, S. Selleri, L. Vincetti, and M. Zoboli; *Holey fiber analysis through the finite-element method*; IEEE Photonics Technology Letters **14**, 1530 (2002).

[75] F. Brechet, J. Marcou, D. Pagnoux, and P. Roy; *Complete Analysis of the Characteristics of Propagation in Photonic Crystal Fibers by the Finite Element Method*; Optical Fiber Technology **6**, 181 (2000).

[76] R. Holzlohner, S. Burger, and P. Roberts; *Efficient optimization of hollow-core photonic crystal fiber design using the finite-element method*; J. Eur. Opt. Soc. **1**, 06011 (2006).

[77] S. Burger, L. Zschiedrich, J. Pomplun, and F. Schmidt; *JCMsuite: An Adaptive FEM Solver or Precise Simulations in Nano-Optics*; in *Lasers and Electro-Optics, Quantum Electronics and Laser Science Conference. CLEO/QELS 2008*; ITuE4 (2008).

[78] JCMwave; *Complete Finite Element Technology for Optical Simulations*; JCM-Suite version of 2009, JCMwave GmbH, Bolivarallee 22,14050 Berlin; website: `http://www.jcmwave.com/` (2011).

[79] G. Vienne, Y. Xu, C. Jakobsen, H.-J. Deyerl, J. Jensen, T. Sorensen, T. Hansen, Y. Huang, M. Terrel, R. Lee, N. Mortensen, J. Broeng, H. Simonsen, A. Bjarklev, and A. Yariv; *Ultra-large bandwidth hollow-core guiding in all-silica Bragg fibers with nano-supports*; Opt. Express **12**, 3500 (2004).

[80] J. C. Knight, J. Broeng, T. A. Birks, and P. S. J. Russell; *Photonic Band Gap Guidance in Optical Fibers*; Science **282**, 1476 (1998).

[81] A. Bjarklev, J. Broeng, and A. S. Bjarklev; *Photonic Crystal Fibers* (Kluwer, New York, 2003).

[82] M. Moenster, P. Glas, R. Iliew, R. Wedell, and G. Steinmeyer; *Microstructure Fiber Soliton Laser*; IEEE Photonics Technology Letters **18**, 2502 (2006).

[83] M. Moenster, G. Steinmeyer, R. Iliew, F. Lederer, and K. Petermann; *Analytical relation between effective mode field area and waveguide dispersion in microstructure fibers*; Opt. Lett. **31**, 3249 (2006).

[84] R. F. Cregan, B. J. Mangan, J. C. Knight, T. A. Birks, P. S. J. Russell, P. J. Roberts, and D. C. Allan; *Single-Mode Photonic Band Gap Guidance of Light in Air*; Science **285**, 1537 (1999).

[85] F. Luan, J. Knight, P. Russell, S. Campbell, D. Xiao, D. Reid, B. Mangan, D. Williams, and P. Roberts; *Femtosecond soliton pulse delivery at 800 nm wavelength in hollow-core photonic bandgap fibers*; Opt. Express **12**, 835 (2004).

[86] K. Saitoh, N. Mortensen, and M. Koshiba; *Air-core photonic band-gap fibers: the impact of surface modes*; Opt. Express **12**, 394 (2004).

[87] J. West, C. Smith, N. Borrelli, D. Allan, and K. Koch; *Surface modes in air-core photonic band-gap fibers*; Opt. Express **12**, 1485 (2004).

[88] G. Humbert, J. Knight, G. Bouwmans, P. Russell, D. Williams, P. Roberts, and B. Mangan; *Hollow core photonic crystal fibers for beam delivery*; Opt. Express **12**, 1477 (2004).

[89] D. G. Ouzounov, F. R. Ahmad, D. Muller, N. Venkataraman, M. T. Gallagher, M. G. Thomas, J. Silcox, K. W. Koch, and A. L. Gaeta; *Generation of Megawatt Optical Solitons in Hollow-Core Photonic Band-Gap Fibers*; Science **301**, 1702 (2003).

[90] P. Yeh, A. Yariv, and E. Marom; *Theory of Bragg fiber*; J. Opt. Soc. Am. **68**, 1196 (1978).

[91] J.-L. Archambault, R. Black, S. Lacroix, and J. Bures; *Loss calculations for antiresonant waveguides*; J. Lightwave Technol. **11**, 416 (1993).

[92] K. J. Rowland, V. S. Afshar, and T. M. Monro; *Novel Low-Loss Bandgaps in All-Silica Bragg Fibers*; J. Lightwave Technol. **26**, 43 (2008).

[93] S. Johnson, M. Ibanescu, M. Skorobogatiy, O. Weisberg, T. Engeness, M. Soljacic, S. Jacobs, J. Joannopoulos, and Y. Fink; *Low-loss asymptotically single-mode propagation in large-core Omniguide fibers*; Opt. Express **9**, 748 (2001).

[94] K. Morishita, Y. Obata, and N. Kumagai; *An Exact Analysis of Propagation Modes Group Velocity for in Optical Fibers*; IEEE Transactions on Microwave Theory and Techniques **30**, 1821 (1982).

[95] R. Iliew, C. Etrich, and F. Lederer; *Remote coupling in Bragg fibers*; Opt. Lett. **29**, 1596 (2004).

[96] J. Marcou, F. Brechet, and P. Roy; *Design of weakly guiding Bragg fibres for chromatic dispersion shifting towards short wavelengths*; Journal of Optics A **3**, 144 (2001).

[97] J. Harrington, C. Rabii, and D. Gibson; *Transmission properties of hollow glass waveguides for the delivery of surgical laser power*; IEEE Journal of Selected Topics in Quantum Electronics **5**, 948 (1999).

[98] G. Renversez, P. Boyer, and A. Sagrini; *Antiresonant reflecting optical waveguide microstructured fibers revisited: a new analysis based on leaky mode coupling*; Opt. Express **14**, 5682 (2006).

[99] F. Ouellette; *Dispersion cancellation using linearly chirped Bragg grating filters in optical waveguides*; Opt. Lett. **12**, 847 (1987).

[100] R. Szipőcs, K. Ferencz, C. Spielmann, and F. Krausz; *Chirped multilayer coatings for broadband dispersion control in femtosecond lasers*; Opt. Lett. **19**, 201 (1994).

[101] N. Matuschek, F. Kärtner, and U. Keller; *Analytical design of double-chirped mirrors with custom-tailored dispersion characteristics*; IEEE Journal of Quantum Electronics **35**, 129 (199).

[102] M. Hisatomi, M. C. Parker, and S. D. Walker; *Binary Multi-Zoned Microstructured Fiber: A Comparative Dispersion Analysis of Radially Chirped Bragg Fiber*; J. Lightwave Technol. **23**, 3551 (2005).

[103] J. S. Skibina, R. Iliew, J. Bethge, M. Bock, D. Fischer, V. I. Beloglasov, R. Wedell, and G. Steinmeyer; *Modes in a CPCF*; Supplementary information (video) in Nature Photonics, online: `www.nature.com/nphoton/journal/v2/n11/suppinfo/nphoton.2008.203_S1.html` (2011).

[104] Y. S. Chan, C. T. Chan, and Z. Y. Liu; *Photonic Band Gaps in Two Dimensional Photonic Quasicrystals*; Phys. Rev. Lett. **80**, 956 (1998).

[105] A. Husakou and J. Herrmann; *Dispersion control in ultrabroadband dielectric-coated metallic hollow waveguides*; Opt. Express **16**, 3834 (2008).

[106] A. Husakou and J. Herrmann; *Chirped multilayer hollow waveguides with broadband transmission*; Opt. Express **17**, 3025 (2009).

[107] E. A. J. Marcatili and R. A. Schmeltzer; *Hollow metallic and dielectric waveguides for long distance optical transmission and lasers*; Bell Syst. Tech. J. **43**, 1783 (1964).

[108] NKT-Photonics; *HC 800-01 Hollow Core Photonic Fiber*; product data sheet, NKT Photonics A/S, Blokken 84, 3460 Birkerød, Denmark, and online: `http://www.nktphotonics.com/files/files/HC-800-01-100409.pdf` (2011).

[109] T. Le, G. Tempea, Z. Cheng, M. Hofer, and A. Stingl; *Routes to fiber delivery of ultra-short laser pulses in the 25 fs regime*; Opt. Express **17**, 1240 (2009).

[110] G. Steinmeyer; *Dispersion oscillations in ultrafast phase-correction devices*; IEEE Journal of Quantum Electronics **39**, 1027 (2003).

[111] J. Bethge, G. Steinmeyer, S. Burger, F. Lederer, and R. Iliew; *Guiding Properties of Chirped Photonic Crystal Fibers*; J. Lightwave Technol. **27**, 1698 (2009).

[112] *Supercontinuum light*; Photonics Dictonary, Laurin Publishing, and online: `http://www.photonics.com/Dictionary` (2011).

[113] R. R. Alfano and S. L. Shapiro; *Observation of Self-Phase Modulation and Small-Scale Filaments in Crystals and Glasses*; Phys. Rev. Lett. **24**, 592 (1970).

[114] R. R. Alfano; *The Supercontinuum Laser Source*; 2nd edition (Springer, New York, 2005).

[115] A. Brodeur and S. L. Chin; *Ultrafast white-light continuum generation and self-focusing in transparent condensed media*; J. Opt. Soc. Am. B **16**, 637 (1999).

[116] M. Bradler, P. Baum, and E. Riedle; *Femtosecond continuum generation in bulk laser host materials with sub-microjoule pump pulses*; Appl. Phys. B **97**, 561 (2009).

[117] W. Liu, O. Kosareva, I. Golubtsov, A. Iwasaki, A. Becker, V. Kandidov, and S. Chin; *Femtosecond laser pulse filamentation versus optical breakdown*; Appl. Phys. B **76**, 215 (2003).

[118] A. Braun, G. Korn, X. Liu, D. Du, J. Squier, and G. Mourou; *Self-channeling of high-peak-power femtosecond laser pulses in air*; Opt. Lett. **20**, 73 (1995).

[119] M. A. Foster, A. C. Turner, M. Lipson, and A. L. Gaeta; *Nonlinear optics in photonic nanowires*; Opt. Express **16**, 1300 (2008).

[120] T. A. Birks, W. J. Wadsworth, and P. S. J. Russell; *Supercontinuum generation in tapered fibers*; Opt. Lett. **25**, 1415 (2000).

[121] J. M. Dudley, G. Genty, and S. Coen; *Supercontinuum generation in photonic crystal fiber*; Rev. Mod. Phys. **78**, 1135 (2006).

[122] A. Penzkofer, A. Laubereau, and W. Kaiser; *Stimulated Short-Wave Radiation due to Single-Frequency Resonances of* $\chi^{(3)}$; Phys. Rev. Lett. **31**, 863 (1973).

[123] I. Hartl, X. D. Li, C. Chudoba, R. K. Ghanta, T. H. Ko, J. G. Fujimoto, J. K. Ranka, and R. S. Windeler; *Ultrahigh-resolution optical coherence tomography using continuum generation in an air-silica microstructure optical fiber*; Opt. Lett. **26**, 608 (2001).

[124] D. J. Jones, S. A. Diddams, J. K. Ranka, A. Stentz, R. S. Windeler, J. L. Hall, and S. T. Cundiff; *Carrier-Envelope Phase Control of Femtosecond Mode-Locked Lasers and Direct Optical Frequency Synthesis*; Science **288**, 635 (2000).

[125] J. Ye, H. Schnatz, and L. Hollberg; *Optical frequency combs: from frequency metrology to optical phase control*; IEEE Journal of Selected Topics in Quantum Electronics **9**, 1041 (2003).

[126] M. Ere-Tassou, C. Przygodzki, E. Fertein, and H. Delbarre; *Femtosecond laser source for real-time atmospheric gas sensing in the UV-visible*; Opt. Commun. **220**, 215 (2003).

[127] Y. Sych, R. Engelbrecht, B. Schmauss, D. Kozlov, T. Seeger, and A. Leipertz; *Broadband time-domain absorption spectroscopy with a ns-pulse supercontinuum source*; Opt. Express **18**, 22762 (2010).

[128] V. I. Bespalov and V. I. Talanov; *Filamentary Structure of Light Beams in Nonlinear Liquids*; Soviet Journal of Experimental and Theoretical Physics Letters **3**, 307 (1966).

[129] P. Glas, D. Fischer, G. Steinmeyer, A. Husakou, J. Herrmann, R. Iliew, N. Skibina, V. Beloglasov, and Y. Skibina; *Supercontinuum generation in a two-dimensional photonic kagome crystal*; Appl. Phys. B **81**, 209 (2005).

[130] G. Qin, X. Yan, C. Kito, M. Liao, C. Chaudhari, T. Suzuki, and Y. Ohishi; *Ultrabroadband supercontinuum generation from ultraviolet to 6.28 micrometer in a fluoride fiber*; Appl. Phys. Lett. **95**, 161103 (2009).

[131] A. Bozolan, C. J. de Matos, C. M. B. Cordeiro, E. M. dos Santos, and J. Travers; *Supercontinuum generation in a water-core photonic crystal fiber*; Opt. Express **16**, 9671 (2008).

[132] K. F. Palmer and W. Dudley; *Optical properties of water in the near infrared*; J. Opt. Soc. Am. **64**, 1107 (1974).

[133] M. A. Khashan and A. Y. Nassif; *Accurate determination of solid and liquid dispersions from spectra channeled with the Fabry-Perot interferometer*; Appl. Opt. **36**, 6843 (1997).

[134] L. Kou, D. Labrie, and P. Chylek; *Refractive indices of water and ice in the 0.65- to 2.5-μm spectral range*; Appl. Opt. **32**, 3531 (1993).

[135] T. A. Birks, J. C. Knight, and P. S. Russell; *Endlessly single-mode photonic crystal fiber*; Opt. Lett. **22**, 961 (1997).

[136] A. V. Husakou and J. Herrmann; *Supercontinuum generation, four-wave mixing, and fission of higher-order solitons in photonic-crystal fibers*; J. Opt. Soc. Am. B **19**, 2171 (2002).

[137] C. L. Arnold, A. Heisterkamp, W. Ertmer, and H. Lubatschowski; *Computational model for nonlinear plasma formation in high NA micromachining of transparent materials and biological cells*; Opt. Express **15**, 10303 (2007).

[138] I. Santa, P. Foggi, R. Righini, and J. H. Williams; *Time-Resolved Optical Kerr Effect Measurements in Aqueous Ionic Solutions*; J. Phys. Chem. **98**, 7692 (1994).

[139] G. Schulz; *Experimentelle Untersuchungen an mikrostrukturierten Glasfasern mit Flüssigkeitsgefülltem Kern*; Master's thesis; Universität Rostock (2009).

[140] C. Martelli, J. Canning, K. Lyytikainen, and N. Groothoff; *Water-core Fresnel fiber*; Opt. Express **13**, 3890 (2005).

[141] Y. Huang, Y. Xu, and A. Yariv; *Fabrication of functional microstructured optical fibers through a selective-filling technique*; Appl. Phys. Lett. **85**, 5182 (2004).

[142] K. Nielsen, D. Noordegraaf, T. Sörensen, A. Bjarklev, and T. P. Hansen; *Selective filling of photonic crystal fibres*; Journal of Optics A **7**, L13 (2005).

[143] L. Xiao, W. Jin, M. Demokan, H. Ho, Y. Hoo, and C. Zhao; *Fabrication of selective injection microstructured optical fibers with a conventional fusion splicer*; Opt. Express **13**, 9014 (2005).

[144] J. Bethge, A. Husakou, F. Mitschke, F. Noack, U. Griebner, G. Steinmeyer, and J. Herrmann; *Two-octave supercontinuum generation in a water-filled photonic crystal fiber*; Opt. Express **18**, 6230 (2010).

[145] B. V. Zhmud, F. Tiberg, and K. Hallstensson; *Dynamics of Capillary Rise*; Journal of Colloid and Interface Science **228**, 263 (2000).

[146] F. M. White; *Viscous Fluid Flow* (McGraw-Hill Education, Kingston, 1991).

[147] J. Zeng; *On Modeling of Capillary Filling*; Application Note, Coventor Inc., 4000 Centregreen Way, suite 190, 27513 Cary, NC, USA, and online: `http://www.coventor.com/pdfs/on_modeling_of_capillary_filling.pdf` (2011).

[148] A. Demircan, S. Amiranashvili, and G. Steinmeyer; *Controlling light by light with an optical event horizon*; Phys. Rev. Lett. **106**, 163901 (2011).

[149] D. A. B. Miller; *Are optical transistors the logical next step?*; Nat Photon. **4**, 3 (2010).

[150] Nobelprize.org; *The Nobel Prize in Physics 1956*; The Official Web Site of the Nobel Prize: `http://nobelprize.org/nobel_prizes/physics/laureates/1956/` (2011).

[151] J. Bardeen and W. H. Brattain; *The Transistor, A Semi-Conductor Triode*; Phys. Rev. **74**, 230 (1948).

[152] I. Ross; *The invention of the transistor*; Proceedings of the IEEE **86**, 7 (1998).

[153] D. Miller, S. Smith, and C. Seaton; *Optical bistability in semiconductors*; IEEE Journal of Quantum Electronics **17**, 312 (1981).

[154] S. Smith and B. Wherrett; *Optical bistability in semiconductors*; Lecture Notes in Physics **182**, 1 (1983).

[155] E. Abraham and S. D. Smith; *Optical bistability and related devices*; Reports on Progress in Physics **45**, 815 (1982).

[156] K. Jain and G. W. Pratt, Jr.; *Optical transistor*; Appl. Phys. Lett. **28**, 719 (1976).

[157] L. A. Orozco, A. T. Rosenberger, and H. J. Kimble; *Intrinsic Dynamical Instability in Optical Bistability with Two-Level Atoms*; Phys. Rev. Lett. **53**, 2547 (1984).

[158] H. Gibbs; *Optical Bistability: Controlling Light with Light* (Academic Press, Orlando, 1985).

[159] P. W. Smith and E. H. Turner; *A bistable Fabry-Perot resonator*; Appl. Phys. Lett. **30**, 280 (1977).

[160] M. Sheik-Bahae, D. C. Hutchings, D. J. Hagan, and E. W. Van Stryland; *Dispersion of bound electron nonlinear refraction in solids*; IEEE Journal of Quantum Electronics **27**, 1296 (1991).

[161] W. Lee, F. Amoozegar, and E. Afshari; *Picosecond pulse generation on CMOS: Design beyond transistor limits*; in *2009 IEEE Radar Conference*; 1–6 (2009).

[162] W. Hafez and M. Feng; *Experimental demonstration of pseudomorphic heterojunction bipolar transistors with cutoff frequencies above 600 GHz*; Appl. Phys. Lett. **86**, 152101 (2005).

[163] International Technology Roadmap for Semiconductors (ITRS); *The 2009 International Technology Roadmap for Semiconductors*; website: `http://www.itrs.net/` (2011).

[164] U.S. Environmental Protection Agency; *Report to Congress on Server and Data Center Energy Efficiency*; Public Law 109-431 online: `http://www.energystar.gov` (2011).

[165] J. Hwang, M. Pototschnig, R. Lettow, G. Zumofen, A. Renn, S. Gotzinger, and V. Sandoghdar; *A single-molecule optical transistor*; Nature **460**, 76 (2009).

[166] G. Zumofen, N. M. Mojarad, V. Sandoghdar, and M. Agio; *Perfect Reflection of Light by an Oscillating Dipole*; Phys. Rev. Lett. **101**, 180404 (2008).

[167] G. S. Agarwal and S. Huang; *Electromagnetically induced transparency in mechanical effects of light*; Phys. Rev. A **81**, 041803 (2010).

[168] S. Weis, R. Riviere, S. Deleglise, E. Gavartin, O. Arcizet, A. Schliesser, and T. J. Kippenberg; *Optomechanically Induced Transparency*; Science **330**, 1520 (2010).

[169] L. Tong, R. R. Gattass, J. B. Ashcom, S. He, J. Lou, M. Shen, I. Maxwell, and E. Mazur; *Subwavelength-diameter silica wires for low-loss optical wave guiding*; Nature **426**, 816 (2003).

[170] L. Tong, J. Lou, R. R. Gattass, S. He, X. Chen, Liu, and E. Mazur; *Assembly of Silica Nanowires on Silica Aerogels for Microphotonic Devices*; Nano Lett. **5**, 259 (2005).

[171] M. Foster, K. Moll, and A. Gaeta; *Optimal waveguide dimensions for nonlinear interactions*; Opt. Express **12**, 2880 (2004).

[172] T. G. Philbin, C. Kuklewicz, S. Robertson, S. Hill, F. König, and U. Leonhardt; *Fiber-Optical Analog of the Event Horizon*; Science **319**, 1367 (2008).

[173] A. V. Gorbach and D. V. Skryabin; *Bouncing of a dispersive pulse on an accelerating soliton and stepwise frequency conversion in optical fibers*; Opt. Express **15**, 14560 (2007).

[174] R. W. Robinett; *Quantum wave packet revivals*; Physics Reports **392**, 1 (2004).

[175] S. Amiranashvili and A. Demircan; *Hamiltonian structure of propagation equations for ultrashort optical pulses*; Phys. Rev. A **82**, 013812 (2010).

[176] K. Blow and D. Wood; *Theoretical description of transient stimulated Raman scattering in optical fibers*; IEEE Journal of Quantum Electronics **25**, 2665 (1989).

[177] S. Amiranashvili, U. Bandelow, and A. Mielke; *Padé approximant for refractive index and nonlocal envelope equations*; Opt. Commun. **283**, 480 (2010).

[178] R. R. Alfano, P. L. Baldeck, P. P. Ho, and G. P. Agrawal; *Cross-phase modulation and induced focusing due to optical nonlinearities in optical fibers and bulk materials*; J. Opt. Soc. Am. B **6**, 824 (1989).

[179] G. P. Agrawal, P. L. Baldeck, and R. R. Alfano; *Temporal and spectral effects of cross-phase modulation on copropagating ultrashort pulses in optical fibers*; Phys. Rev. A **40**, 5063 (1989).

[180] NKT-Photonics; *NL pm 750 Nonlinear Photonic Crystal Fiber*; product data sheet, NKT Photonics A/S, Blokken 84, 3460 Birkerød, Denmark, and online: `http://www.nktphotonics.com/files/files/NL-PM-750-090612.pdf` (2011).

[181] D. Mogilevtsev, T. A. Birks, and P. S. J. Russell; *Group-velocity dispersion in photonic crystal fibers*; Opt. Lett. **23**, 1662 (1998).

[182] NKT-Photonics; *NL-1050-ZERO-2 Nonlinear Photonic Crystal Fiber*; product data sheet, NKT Photonics A/S, Blokken 84, 3460 Birkerød, Denmark, and online: `http://www.nktphotonics.com/files/files/NL-1050-ZERO-2-060531.pdf` (2011).

[183] NKT-Photonics; *NL-1.5-670 Highly nonlinear PCF*; product data sheet, NKT Photonics A/S, Blokken 84, 3460 Birkerød, Denmark, and online: `http://www.nktphotonics.com/files/files/NL-15-670.pdf` (2011).

[184] avantes; *AvaSpec-3648 High Resolution Fiber Optic Spectrometer*; product datasheet, Avantes BV, Soerense Zand Noord 26, NL-6961 RB Eerbeek, The Netherlands, and online: `http://www.avantes.com/` (2011).

[185] A. Yang, X. Li, A. Xu, and D. Wu; *Combined impacts of group velocity dispersion, Kerr effect and polarization mode dispersion in optical fibers*; Opt. Commun. **214**, 133 (2002).

[186] H. A. Haus and E. P. Ippen; *Group velocity of solitons*; Opt. Lett. **26**, 1654 (2001).

Selbständigkeitserklärung

Ich erkläre, dass ich die vorliegende Arbeit selbständig und nur unter Verwendung der angegebenen Literatur und Hilfsmittel angefertigt habe.

Ann Arbor, den 28. Juli 2011 Jens Lutz Bethge

Danksagung

Ich danke Prof. Dr. Thomas Elsässer für die Betreuung meiner Promotion und die Möglichkeit, meine Forschung auf internationalen Konferenzen zu präsentieren. Bei PD Dr. Günter Steinmeyer bedanke ich mich für die langjährige Betreuung, Förderung, Unterstützung und für die Weitergabe von umfangreichem Wissen nicht nur im Bereich der Ultrakurzpulslaser.

Ich bedanke mich bei Dr. Roland Müller für die kontinuierliche Zusammenarbeit und die anregenden Diskussionen über die Theorie der Elektrodynamik. Frau Dorit Fischer und Hanjo Benedix danke ich für die Umsetzung meiner Ideen und Betreuung der Experimente. Mein Dank gilt auch Prof. Dr. Fedor Mitschke, Dr. Ayhan Demircan, Dr. Anton Husakou, Dr. Joachim Herrmann, Dr. Julia Skibina und Dr. Tuan Le für die Zusammenarbeit.

Ein großer Dank geht auch an Dr. Christian Grebing, Dr. Thomas Hansel, Sebastian Koke, Bastian Borchers, Dr. Uwe Griebner, Dr. Rüdiger Grunwald, Martin Bock, Andreas Schmidt, Dr. Jie Jang und Dr. Ingmar Hartl für ihre Kollegialität und Hilfsbereitschaft.

Zu guter Letzt möchte ich mich noch meiner Familie und bei Dr. Rebekah Rota für ihre Unterstützung bedanken.